Phase Transformations in Steels during Quenching and Partitioning Heat Treatment

by

Yiming Hu

to obtain the degree of Master of Science in Mechanical Engineering
at the Delft University of Technology,
to be defended publicly on December 13, 2016 at 9:30 AM.

Student number:	4417739	
Project duration:	February 12, 2016 – December 13, 2016	
Thesis committee:	Dr. M. J. Santofimia,	TU Delft, supervisor & chair
	Dr. B. Kim,	TU Delft, supervisor
	Prof. J. Sietsma,	TU Delft
	Dr. M. Hermans,	TU Delft

An electronic version of this thesis is available at `http://repository.tudelft.nl/`.

TU Delft

Acknowledgement

First of all, I would like to express my sincerest gratitude to my supervisors Dr. Bij-Na KimLee and Dr. Maria J. Santofimia for their guidance and support through this project. They have been so inspiring and gave me the freedom to work on my interested areas. Not only have I acquired expertise in materials science from them, but I learned how to be a more organised person. Besides my supervisors, I want to thank Prof. Jilt Sietsma and Dr. Marcel Hermans for being my committee members.

I would also like to thank the technicians who work in the Department of Materials Science and Engineering: Nico Geerlofs who trained me in dilatometry experiments, Richard Huizenga who helped me carry out the XRD measurements, Kees Kwakernaak who trained me in SEM and Sander van Asperen who helped me with sample preparations. Without their participation and input, my lab works would not have gone so smoothly.

Special thanks should be given to Dr. Michael Janssen, Prof. Ian Richardson and Prof. Jilt Sietsma for their agreement on substitution of my previous lab works for internship so that I can be fully devoted to this thesis project.

Many thanks to Qiyu Lei and Hao Feng for cheering me up when I am depressed. I would also like to thank Jiefu Hou, Giridharan Krishnamurthy and Aakarshit Kalra for their accompany through this thesis work. Thanks to Dr. Mingzhi Dong, I firstly understand how scientific research should be done. Acknowledgement should be given to Ramin Barak for all the thoughtful talks.

Finally, I must express my profound gratefulness to my parents for their unconditional love, continuous encouragement and unfailing support.

Yiming Hu
Delft, December 2016

Abstract

Quenching and Partitioning (Q&P) processed steel is a promising candidate for the third-generation advanced high strengths steel (AHSS), where considerable amount of carbon-enriched austenite can be obtained in the steel microstructure. The Q&P process starts with full or partial austenisation of the steel, followed by a quench to form a desired amount of martensite and an isothermal holding (the partitioning step) for carbon to partition from martensite into austenite. The end point of the carbon partitioning is predicted by a model referred to as Constrained Carbon Equilibrium (CCE), which assumes a stationary martensite/austenite interface during the partitioning step and precludes any competing reaction, e.g. bainite formation and carbide precipitation. However, it remains controversial whether martensite/austenite interface remains stationary during partitioning and competing reactions have been reported to occur, which can influence the final steel microstructure.

This thesis therefore aims to study the phase transformations accompanying carbon partitioning during the Q&P process. A steel was heat treated by the Q&P process to investigate the evolution of phase fractions during/approaching the stabilisation of carbon content using dilatometry and Synchrotron X-Ray Diffraction (SXRD). The steel is a model alloy of composition Fe–0.2C–3Mn–2Si (wt.%). From a set of preliminary heat treatments using dilatometry, 400 °C was chosen as the optimal partitioning temperature for a secondary dilatometry tests and the in-situ SXRD.

Results show that as the initial quenching stops, the austenite continues to transform during the short holding and reheating, which might be associated with the formation of martensite and then bainite. The bainitic transformation continues to the end of partitioning step. The consumption of austenite is also accompanied by the increased carbon level of austenite. Therefore, the carbon enrichment in austenite is achieved by the coupling of carbon partitioning from martensite and bainitic transformation. From the end of initial quenching to the end of partitioning step, 40%-50% of previously retained austenite was consumed. The rate of transformation is highest at the beginning of reheating.

Microstructure consisting of tempered martensite with carbides, bainite and retained austenite is obtained through the Q&P process, with tempered martensite mainly as the BCC phase. The RA fraction can be adjusted from 6.9 vol.% to 14.3 vol.% with little or no formation of fresh martensite. The time required to acquire the multi-phase microstructure can be greatly reduced compared to austempering.

Keywords: quenching and partitioning, synchrotron XRD, carbon enrichment, retained austenite

Contents

1 Introduction

1.1. Third Generation AHSS

It was the oil crisis in 1975 that the goal to decrease fuel consumption in the automobile industry immediately projected onto a demand for lighter yet stronger steels [1]. Despite the short period of this crisis, it had a revolutionary impact on the development of sheet steels.

Dual-phase (DP) steels firstly demonstrated its combination of strength and ductility [2] in 1975 and attracted the attention of leading metallurgist and then steelmakers, whereas successful trials and growing applications of DP steels were seen only until mid 1990s. Higher strength and ductility signify that thinner sheets can be used for components while still maintaining structural integrity, and therefore the weight of the car body can be reduced. During the period when DP steels received little interest from the auto industry, only the so-called conventional HSS including highstrength interstitial free (IF) steels and mostly batch-annealed or sometimes continuously annealed High Strength Low Alloy (HSLA) steels with TS $\sim$ 450 – 550 MPa were developed [3].

With competitions from low-density metals such as Al and Mg and growing requirements for passenger safety, vehicle performance and fuel economy, the steel industry responded by developments of steels with special strength and formability parameters, known as "Advanced High Strength Steels" (AHSS) [1, 4]. While the main category of AHSS is the DP steel, automotive customer requirements led to the development of new special microstructures of high-strength sheet steels. The **Tr**ansformation-**I**nduced **P**lasticity (TRIP) steels, for example, possess enhanced stretchability and higher absorbed energy compared to DP steels with the same yield strength (YS) [5].

Figure 1.1 known as the "banana diagram" summarizes the tensile strength and tensile elongation data for various classes of conventional steels and AHSS. DP steels and TRIP steels, together with complex phase (CP) steels and martensitic (MART) steels, are the first generation AHSS. The desire to produce steels with considerably higher strengths has brought about the development of the second generation AHSS, which are austenitic steels with high Mn contents [6]. The third Generation AHSS, as forecast by D. Matlock [7], should exhibit strength-ductility combinations significantly better than the first generation AHSS while at a cost significantly less than required for second generation AHSS, and the microstructure consisting of martensite and retained austenite (RA) mixture is suggested [1, 6, 7].

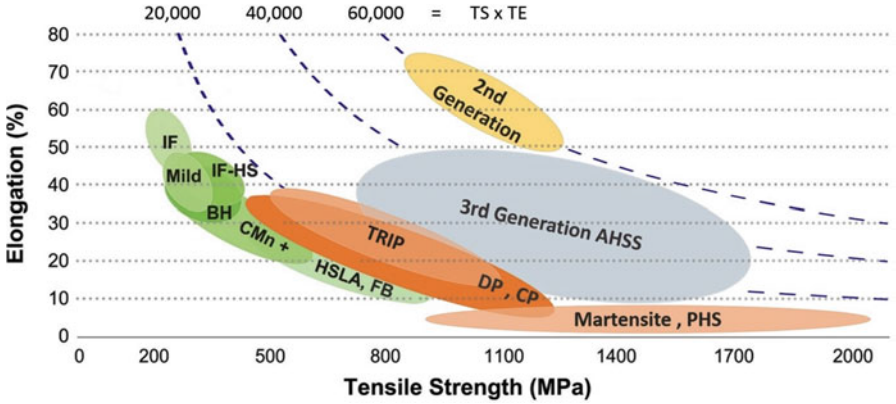

Figure 1.1: Elongation—tensile strength balance diagram for existing variety of formable steels and prospective "third-generation" grades. Modified from reference [7].

1.2. Q&P Process and CCE

The type of microstructure as mentioned above can be achieved using the quenching and partitioning (Q&P) process developed by Speer *et al.*[8], which includes such variants as one-step or two-step Q&P. The partitioning temperature is the same as the quenching temperature in the one-step Q&P, whereas the partitioning is performed at a temperature higher than quenching temperature in two-step Q&P.

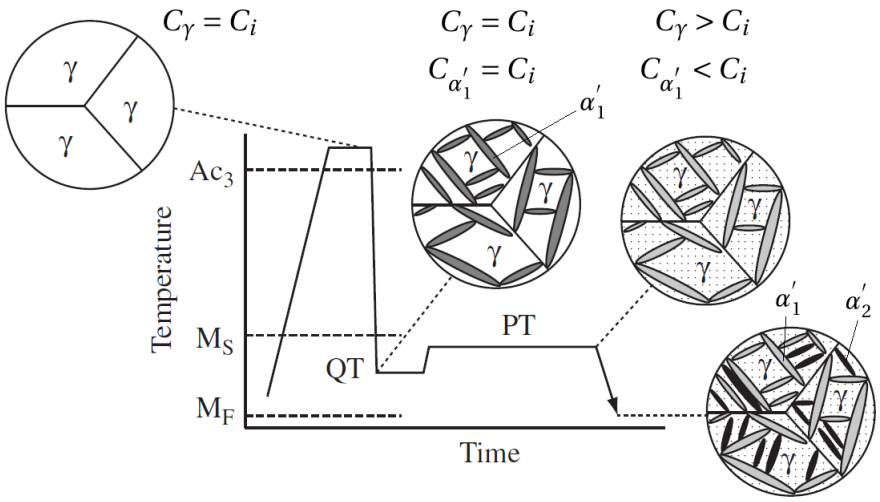

Figure 1.2: Schematic illustration of the Q&P process for producing austenite-containing microstructures. γ, α_1', and α_2' represents the austenite, initial martensite and final martensite, respectively. C_i, C_γ and $C_{\alpha_1'}$ represent the carbon concentrations in the initial alloy, austenite, and martensite, respectively. QT and PT are the quenching and partitioning temperatures. Adapted from [9].

Figure 1.2 depicts a typical two-step Q&P process. After full austenitisation above the A_{c3} temperature, the steel is quenched to a quenching temperature (QT). At this temperature, a fraction of martensite α_1' is formed, where the carbon content in α_1' is the same as that in the austenite γ, and is equal to the carbon content in the bulk material. α_1' is also referred to as primary martensite. Then the steel is held for a short time, followed by a reheating to the partitioning temperature (PT). During this interval between the initial quenching and isothermal holding, carbon partitioning and phase transformation are not

expected to occur. In the partitioning step, where the steel is isothermally held for a time, the carbon will partition from the martensite to the austenite. The driving force for the carbon partitioning process is the greater chemical potential of carbon in the supersaturated martensite than in the austenite, as shown in Figure 1.3. After the partitioning step, a microstructure of carbon-depleted $\alpha_1^{'}$ and carbon-enriched γ will form. If process parameters are chosen properly with the assumption of no carbide precipitation or bainite formation, all the carbon-enriched γ will be retained at room temperature after final quenching. Otherwise, a fraction of γ will transform to martensite during final quenching, as shown by $\alpha_2^{'}$. To distinguish from the tempered martensite, the martensite formed during the final quenching is referred to as fresh martensite.

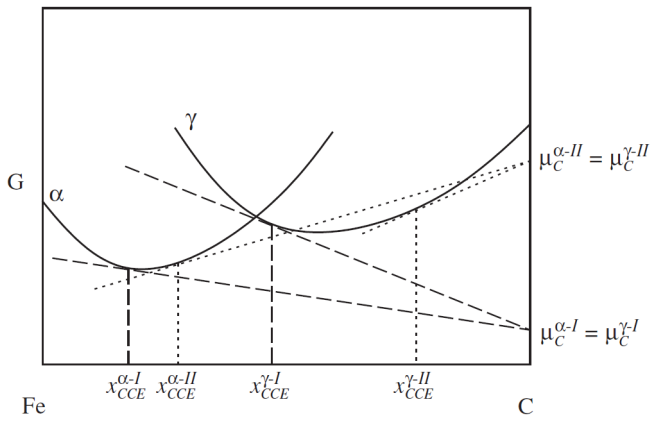

Figure 1.3: Schematic molar Gibbs free energy vs. composition diagrams illustrating metastable equilibrium at a particular temperature between ferrite and austenite in the Fe-C binary system showing two possible conditions (I and II) of CCE [10]. α and γ represents the martensite and austenite, respectively. μ_c is the chemical potential of carbon and x the carbon content. The superscript I or II signifies the CCE condition I or II.

The end point of the partitioning is marked by the equal chemical potential of carbon in both phases, referred to as the constrained paraequilibrium (CPE) [8, 10] firstly by Speer et al. [8]. The term 'constrained carbon equilibrium' (CCE) was later proposed by Hillert and Ågren in place of CPE [11–14]. There are two conditions which are key to CCE:

1. Carbon diffusion is completed when the chemical potential of carbon is equal in the martensite and austenite phases.

2. The number of iron atoms must be conserved in each phase during the approach to CCE.

Condition 1 defines the thermodynamic constraint of CCE. Unlike the full equilibrium, where equilibrium is reached with a unique ferrite and austenite composition at a certain temperature, the CCE is reached with an infinite set of ferrite and austenite compositions. Condition 2 is the matter balance constraint of CCE and is consistent with the presumption of a stationary austenite/martensite interface during the partitioning step. This assumption is based on the fact that as Q&P processing is carried out at a relatively low temperature (350 – 450 °C), the diffusivities of the substitutional alloying elements are too low to partition between martensite and austenite.

1.3. Competing Reactions

Condition 2 of CCE has been questioned and many researchers have suggested the migration of the austenite/martensite interface, either by experiments or by simulations. Zhong *et al.*[15] observed that the interfaces of austenite/martensite changed from almost straight at 480 °C for 3 s to curved structures after increasing the partitioning time to 80 s, indicating possible movements of iron atoms during the partitioning process. Speer et al. [16] then examined qualitatively the implications of the mobility of iron atoms at the interface. That is, there will be changes in the volume fraction of austenite and martensite after the completion of carbon partitioning and repartitioning of carbon atoms might occur as a result.

The theoretical basis for this can be shown in Figure 1.4. Carbon partitioning is considered to be completed before any interface motion. In the case where the carbon concentration in austenite is less than equilibrium (Figure (a)), the iron potential is greater in austenite than in ferrite, thus creating a driving force for iron atoms to move from austenite to ferrite, indicating an interface migration towards austenite, leading to the growth of ferrite and the consumption of austenite. In the case where the carbon concentration in austenite is greater than equilibrium, the iron potential is less in austenite than in ferrite, and the iron atoms will move from ferrite to austenite, indicating an interface migration towards ferrite, resulting in the growth of austenite and the consumption of ferrite. Therefore, the direction of interface movement is controlled by the martensite formation prior to carbon partitioning, with the phase fractions moving towards their equilibrium values consistent with the lever rule. Although carbon partitioning is considered to be completed prior to interface motion due to the greater mobility of carbon atoms at lower temperature, it should also be noted that any interface movement that occurs will create a need for subsequent carbon redistribution, even if carbon partitioning was complete prior to such movement.

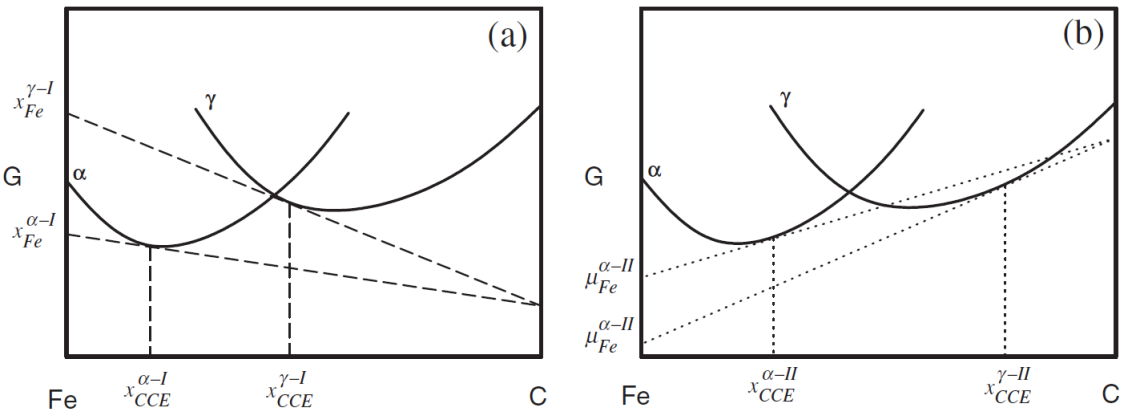

Figure 1.4: Schematic tangent intercepts showing ferrite and austenite compositions having equal chemical potentials for carbon [16].

Santofimia *et al.*[17] later modelled the bidirectional interface migration, and they have incorporated the influence of interface mobility on the interface migration in their following work [18]. DeKnijf *et al.*[19] have observed a clear movement of the austenite/martensite interface in high carbon steel (1wt%) by using in-situ TEM, and compared the experimental results with the calculated martensite grain width evolution with different activation ener-

gies using the model proposed in literatures [17, 18]. The comparisons showed good fit for activation energy between 165 kJ/mol and 170 kJ/mol.

Apart from the possibility of interface migration, bainite transformation [20–22] could decrease the volume fraction of austenite during the partitioning step and hence the fraction of final retained austenite. In literatures, a faster bainitic transformation with presence of martensite have been observed than transformation starting with single-phase austenite [20, 21]. The phase transformation will be accompanied by carbon enrichment in austenite, the mechanism of which is shown in Figure 1.5, where the Gibbs free energy of austenite is equal to that of bainite on T_0 curve. The diffusionless bainitic growth can only occur if the carbon concentration of the austenite lies to the left of the T_0 curve, where the Gibbs free energy of bainite is lower. The enrichment ceases when the austenite composition reaches T_0.

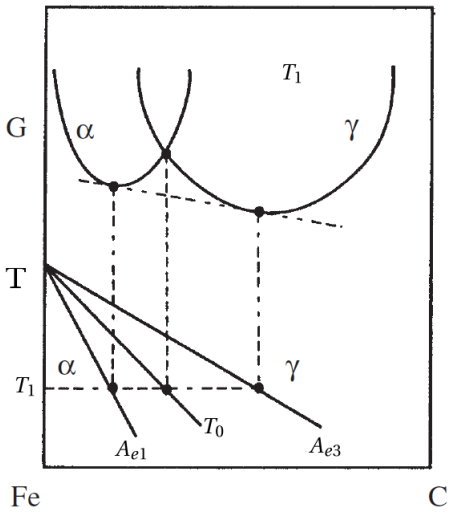

Figure 1.5: Schematic molar Gibbs free energy vs. composition, and temperature vs. composition diagrams illustrating the mechanism of carbon enrichment through formation of carbide-free bainite. Adapted from [23].

Carbides precipitation [24] in martensite could also happen and therefore reduce the amount of carbon partitioning into austenite and affect the stability of austenite during final quenching.

1.4. Objective and Scope of the Thesis

While the in-situ TEM can provide a method to study the local interface mobility, it failed to determine the impact of the moving interface on the evolution of overall austenite fraction, which will influence the final microstructure. Although dilatometry studies can help study the evolution of phase fractions, no direct information on the evolution of carbon content can be obtained. There also exists ambiguity in the interpretations of dilatometry data, e.g. the dilatometric contractions at higher partitioning temperatures may correspond to reduced ferrite growth, austenite growth, and/or martensite tempering effects [25]. Synchrotron XRD (SXRD), however, with its in-situ measurement while applying the thermal cycle, is a technique to study the evolutions of phase fractions and carbon content simultaneously. The evolution of phase fractions of one single phase can be interpreted more directly than dilatometry.

This thesis therefore aims to investigate the microstructural evolutions of a steel during the Q&P process with the help of SXRD. Specifically, the thesis will focus on the change in the volume fraction and carbon content in austenite during the Q&P process. Different Q&P cycles are applied and their corresponding microstructural changes are compared. It is the objective of this thesis to provide experimental proof for the following questions:

- During which stage of the Q&P process will austenite be enriched with carbon?
- Can CCE predict the end point of the carbon partitioning for the studied steel? Will there be any competing process?
- How can we optimise the steel microstructures (i.e. more RA fraction, higher carbon content of RA and less fresh martensite)?

1.5. Structure of the Thesis

The remaining part of the thesis consists of the following chapters:

- Chapter 2 presents the studied material, related experimental techniques and procedures of the experiments.
- Chapter 3 presents the results obtained from the experiments.
- Chapter 4 presents the discussions of the results obtained.
- Chapter 5 presents the conclusions and recommendations for future works.

2

Materials and Experimental Methods

2.1. Material of Study

The studied material is a hot-rolled steel with chemical composition shown in Table 2.1. Manganese is an austenite stabiliser which retards the formation of ferrite, pearlite, and bainite; on the other hand, manganese also promotes carbides formation [23]. Moreover, manganese content higher than 2.5 wt.% leads to banded morphology (Figure 2.1) in the microstructure [26]. The combination of low-carbon and high-silicon contents suppresses the carbide precipitation during the isothermal holding [27, 28].

Table 2.1: Chemical composition of the studied material

Element	C	Mn	Si	Cr	P	S	Al	N
Composition (wt.%)	0.2	2.93	1.97	<0.05	<0.002	<0.001	0.009	<0.001

Figure 2.1 shows the banded microstructure of the steel taken from the 6 mm-thickness slab. The rolling direction (RD) is also shown in the figure, while the transverse direction (TD) is vertical to the surface shown in Figure 2.1. The microstructure consists of martensite, bainite and retained austenite (about 12 vol.% determined by XRD).

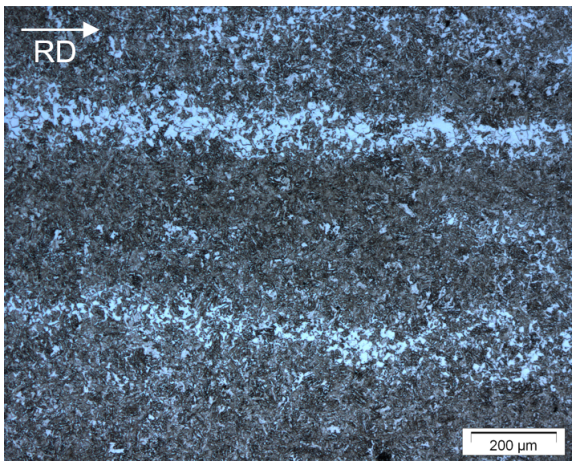

Figure 2.1: Microstructure of the as-received material under optical microscopy showing the banded morphology.

2.2. Dilatometry

Dilatometry is one of the most powerful techniques for the research on solid-state phase transformations in steels, since it allows the in-situ monitoring of the dimensional changes occurring in the sample, which is closely related to the phase transformation and temperature during the application of thermal cycle [29]. The applicability of dilatometry is due to the change of the specific volume (the ratio of volume to mass) of a sample during a phase transformation. When the steel undergoes a phase change, the lattice structure changes, e.g. from α to γ while heated to the A_{c1} temperature.

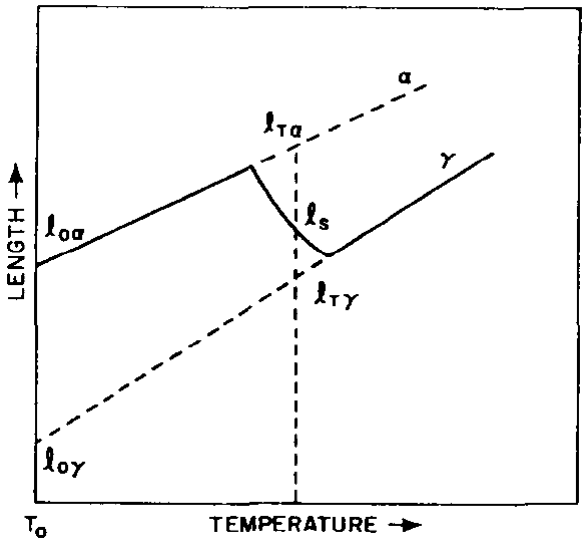

Figure 2.2: Schematic of the expansion process of a steel and the lever rule. The steel is assumed to be fully ferritic before the austenization. [30]

Due to the difference in the atomic volume between α and γ, the phase transformation will be accompanied by the change in the specific volume, and this would be reflected as a sudden change in the length of the steel, as illustrated by Figure 2.2. When the steel is heated, it will expand linearly, until it reaches A_{c1}, where the $\alpha \rightarrow \gamma$ transformation starts, a contraction is expected because of the smaller atomic volume of γ. When the temperature increases to A_{c3}, the steel is fully austenitized and a further increase in temperature will result in the linear expansion of the steel. The transformation temperatures could be identified around the turning point of the dilatometry curve.

The specimens used for the dilatometry tests are in a cylinder geometry, with diameter of the cross-section equal to 3.55 mm and a length of 10 mm. The heat treatments are performed in a DIL 805A/D dilatometer either in a vacuum (less than 2.0×10^{-4} mbar) or helium atmosphere. Figure 2.3 gives a schematic representation of a dilatometer. The sample is clamped between two quartz push rods, and a Linear Variable Differential Transformer is used to record length changes in the sample and the push rods. The specimen is heated by a high-frequency induction coil, and cooling gas (helium) can be applied through the small holes in the induction coil. The thermocouple spot-welded on the specimen is used for temperature record and control. Length resolution of 50 nm can be achieved, and the temperature resolution is 0.05 °C.

In order to obtain the transformation temperature, the offset method proposed by Yang

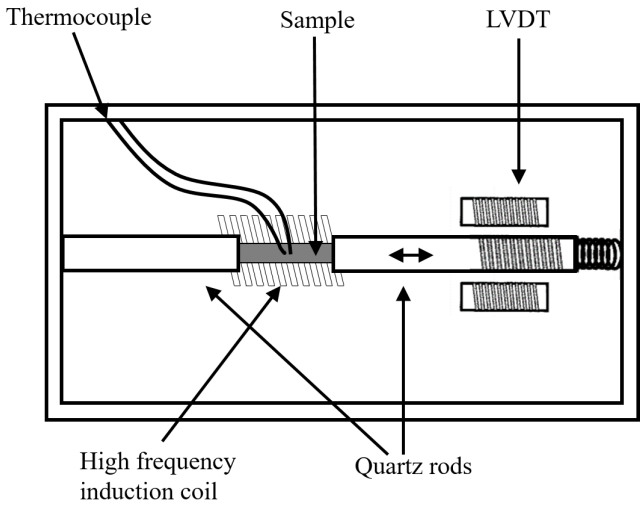

Figure 2.3: Schematic representation of the dilatometer configuration. Adapted from [31].

and Bhadeshia [32] is applied. The offset method determines the transformation temperature with higher accuracy among others and a comparison between these methods can be seen in reference [32]. Figure 2.4 gives an example of the determination of M_s through offset method. Firstly, the data range where austenite contracts linearly is fitted. Then this line is shifted by a value ε_0, which is the strain due to the formation of 1 vol.% martensite, and can be calculated by Eq. (2.1).

$$(1+\varepsilon_0)^3 = a_\gamma^{-3}(2Va_\alpha^3 + (1-V)a_\gamma^3) \tag{2.1}$$

where a_α and a_γ is the lattice parameter of austenite and martensite, respectively, and V is the volume fraction of martensite which is equal to 1% here. The offset line in Figure 2.4 is therefore shifted upwards by ε_0. M_s lies where the experimental data and the offset line intersect, where in this particular case, $M_s = 337.4\,°C$.

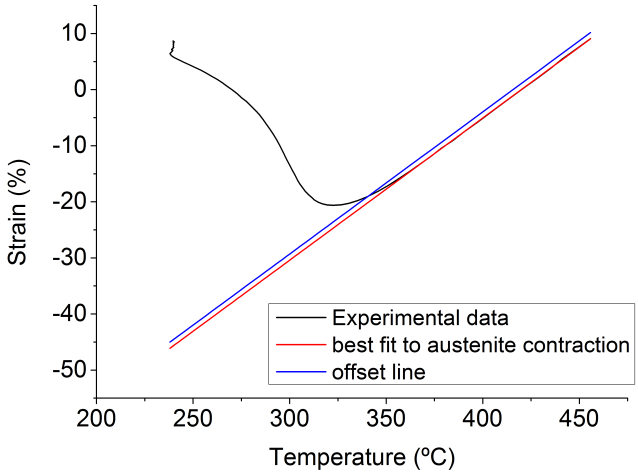

Figure 2.4: Schematic of the offset method.

Apart from the determination of transformation temperatures, dilatometry can also be used to quantitatively determine the amount of transformed phase as a function of temperature using the lever rule as follows [30].

As shown in Figure 2.2, the two dashed line represents the expansion of pure α and pure γ with the increase in temperature, respectively. Any point lying on the curved line in between consists of both α-Fe and γ-Fe. If we draw a line across this point (T, l_s) and intersect with the expansion lines of α-Fe and γ-Fe at (T, $l_{T\alpha}$) and (T, $l_{T\gamma}$), respectively, we could calculate the volume fraction of α-Fe, f_α, as

$$f_\alpha = (l_s - l_{T\gamma})/(l_{T\alpha} - l_{T\gamma}) \tag{2.2}$$

and the details of the derivation for this equation can be seen in reference [30].

2.3. Scanning Electron Microscopy

Scanning electron microscopy (SEM) is used to characterize the microstructures at a higher magnification compared to optical microscopy. Heat-treated specimens will be cut in half and then grinded with sand papers, afterwards, they will be polished to a surface roughness of 1 µm. The polished specimens are etched with 2% nital. Before the observation, the specimens are firstly ultrasonically cleaned with acetone for 2 min, followed by ultrasonic clean with isopropanol for 2 min. SEM observations were performed using a JEOL JSM-6500F field emission gun SEM operating at 15 kV.

2.4. X-Ray Diffraction

X-Ray Diffraction is a technique to investigate the fine structure of matter [33]. This technique can be used to determine crystal structures, the volume fractions of different phases, chemical analysis and stress measurement.

Planes of atoms within a material will diffract beams of X-rays at specific angles, and these diffracted beams are commonly used to characterize various material properties. There are two properties associated with the diffracted beams that are used: the angle between the incident and diffracted beams (2θ) and the intensity of the diffracted beam (I) (Figure 2.5).

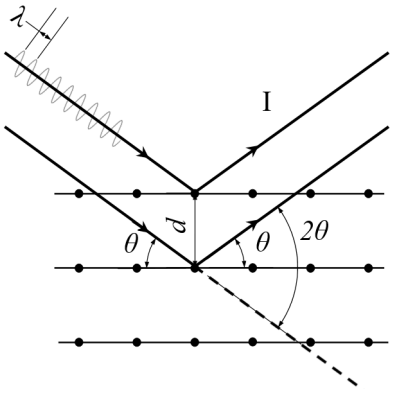

Figure 2.5: Schematic representation of Bragg diffraction of crystallographic planes.

Bragg's law relates the angle θ, the wavelength of the beam (λ) and the spacing between

the planes of atoms in the material (d):

$$n\lambda = 2d\,sin\theta \tag{2.3}$$

Furthermore, the intensity of a given diffracted beam is proportional to the volume of material that has planes spaced and oriented for diffraction in that particular direction. This means that the relative volume of phases within a polycrystalline material can be estimated from the relative intensities of the diffracted beams [33]. For cubic structures, the spacing d between certain planes (hkl) is a function of the lattice parameter a and the Miller indices:

$$d = a/\sqrt{h^2 + k^2 + l^2} \tag{2.4}$$

From Eq. (2.3) and Eq. (2.4) we could relate the lattice parameter to the angle between the incident and diffracted beams. Therefore, from the peak positions of the diffractograms, the lattice parameter of the cubic structure can be calculated. In the case of steels, since the lattice parameter of austenite is related to its carbon content, we can calculate the average carbon content based on the peak positions of the diffractograms.

Hence in this study, XRD is used as a technique to study the volume fraction of austenite and its carbon content. Lab XRD with X-ray tubes and the synchrotron XRD (SXRD) are used. The former source of X-ray is widely available in laboratories while the latter can only be obtained in less than 80 facilities around the world [34].

2.4.1. Lab XRD

Figure 2.6 shows the schematic of the diffractometer using X-ray tube with Bragg-Brentano geometry. After sample preparation, the polished sample is then scanned by the Bruker D8 advanced diffractometer was used. X-rays are produced by the Co target (with 2 portion of Kα_1 and 1 portion of Kα_2 radiation), with photon energy of 6.9 KeV [35], wavelength of 1.79 Å and a penetration depth of 10 µm in steels. During the scanning, the detector position is recorded as the angle 2θ, and 2θ moves from 40° – 135°, with step size of 0.035° and counting time of 4 s for each step. The detector records the number of X-rays observed at each angle 2θ as count, which is proportional to the intensities.

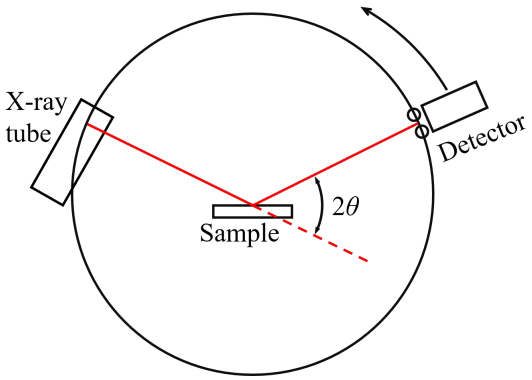

Figure 2.6: Schematic of Bragg-Brentano geometry for X-ray tube sources.

The obtained diffractograms is analysed in the program MAUD as in Section 2.4.3. [36, 37].

2.4.2. In-situ Synchrotron XRD

Compared to the X-ray tube, synchrotron facilities can produce X-rays with much higher energies and intensities [38], which allows the X-ray to be transmitted through the materials (1 mm in thickness in this study) and a larger sample volume can be investigated.

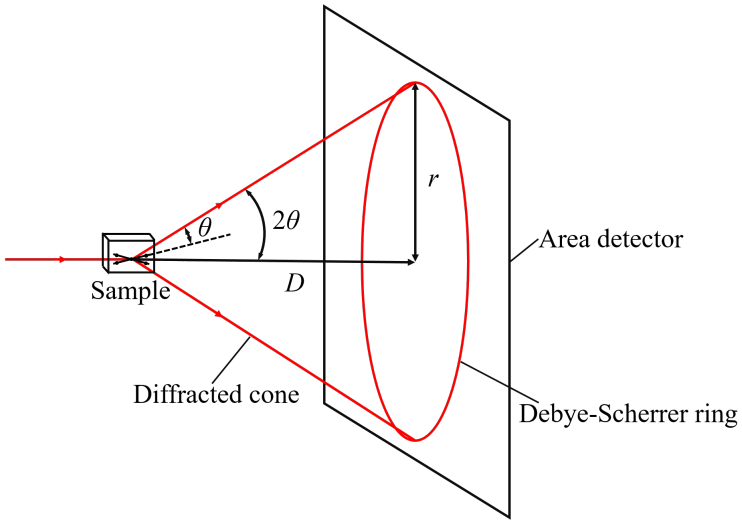

Figure 2.7: Schematic of the transmission Geometry for 2D XRD.

The 2D XRD set-up as shown in Figure 2.7 is used in the synchrotron in this project, which enables much faster data acquisition since all the crystalline planes will diffract the X-rays simultaneously, while in Figure 2.6 the detector needs to rotate in order to record X-rays diffracted by different planes. If the sample is polycrystalline, the diffraction pattern will form a series of diffraction cones and each diffraction cone corresponds to the diffraction from the same family of crystalline planes in all the analysed grains [39]. One cone is shown in Figure 2.7 and the intersection between the cone and the detector will form a ring referred to as the Debye-Scherrer ring. Unlike the $I-2\theta$ data acquisition in 1D XRD, the intensities are recorded in each pixel on the area detector. Azimuthal integration over the rings are needed for further analysis, which will be discussed later. The faster data acquisition in synchrotron XRD can help study the phase transformations in-situ. In fact, some set-up can go as fast as 10 Hz.

The Synchrotron X-ray diffraction (SXRD) experiments were performed at the beamline ID11 of European Synchrotron Radiation Facility (ESRF). The specimens are in a typical tensile specimen geometry (dog-bone shape), as shown in Figure 2.8(a), with an overall length of 40 mm, shoulder length of 10 mm on both sides and a gage cross-section of 1×1 mm^2. The Electrothermal Mechanical Testing (ETMT) System was applied for the thermal cycle during the in-situ XRD experiments. Compared to the dilatometry tests where the steels are heated by the induction coil, heating is achieved by passing direct current through the gauge length of the specimen controlled by a Pt/Pt-13% Rh thermocouple spot-welded to the centre of the gauge length. Argon was used to minimise sample oxidation.

Figure 2.8 presents the schematic of the experimental setup for the measurement. The incident beam has a wavelength $\lambda = 0.15582$ Å (79.57 keV), and the sample to detector distance is about D = 300 mm. The diffracted beams were recorded by the Frelon CCD camera, which has an image resolution of 2048×2048 pixels and a pixel size of $50\times50\,\mu$m^2. Before the in-situ measurement of each specimen, a standard material (CeO_2) was measured for

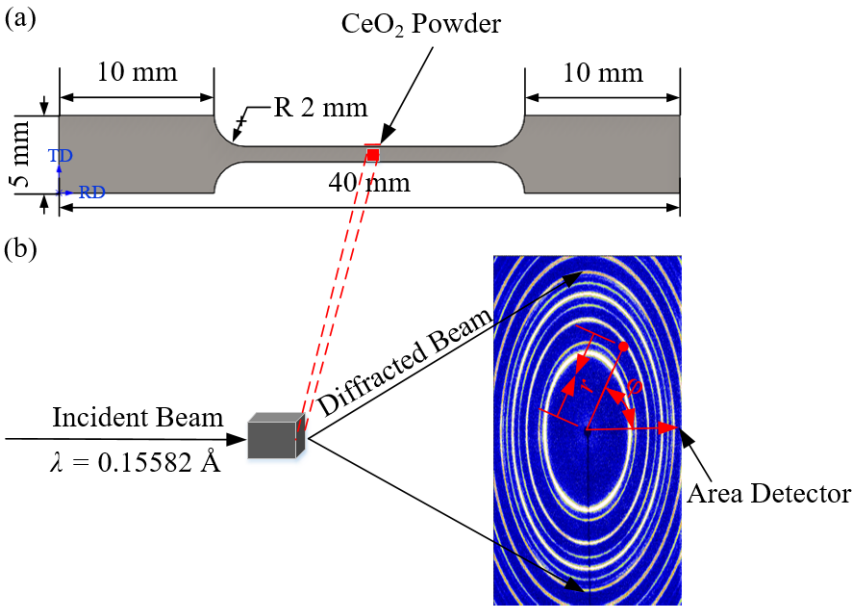

Figure 2.8: (a) A schematic of the specimen showing the area of exposure for SXRD measurements, the beam size is 200 × 200 mm^2. Also shown is the CeO2 powder attached on top of the specimen for calibration. (b) A schematic of the diffraction measurement set-up. the Debye-Scherrer rings are shown on the area detector.

later calibration of the system configuration, e.g. beam center, sample-detector distance and tilted angle of the detector. The time of exposure was 60 s for the CeO_2. During the thermal cycle, the ETMT was run under load control with a set point of zero load to permit free thermal expansion of the sample. The exposure time was 0.1 s for the steel specimens. Including data recording time, powder diffraction rings were therefore recorded at $\sim$0.7 s intervals.

The 2D XRD patterns as in Figure 2.8 need to be reduced to the standard 1D $I-2\theta$ profile for further analysis. However, before the data reduction, calibration for the system configuration (e.g. sample-detector distance, tilt angle of the area detector, etc.) is required. The calibration process can be referred in literature [40] and the calibrated results for each specimen are shown in Table B.1 (see Appendix B.2). The data reduction was performed with the program Fit2D [41, 42] developed at ESRF with system calibration, dark current subtraction, flat field correction and spatial distortion correction. As introduced before, every pixel in the area detector is 50×50 µm^2 in size, and therefore, a pixel $(Column, Row)$ could have a position (x, y) in the Cartesian coordinate system, and

$$\begin{aligned} x &= 50Column \\ y &= 50Row \end{aligned} \tag{2.5}$$

For the azimuthal integration, the polar coordinate system should be used. A point (x, y) in the Cartesian coordinate system can be transformed into a point (r, φ) into the polar coordinates according to:

$$\begin{aligned} r &= \sqrt{x^2 + y^2} \\ \varphi &= \tan^{-1}(y/x) \end{aligned} \tag{2.6}$$

For every point (r, φ) in the area detector, an intensity value $I(r, \varphi)$ is recorded, and for the same radius r, we could integrate over the whole azimuthal range from 0 to 2π to

obtain the relationship between the integrated intensity $I(r)$ and the radius r:

$$I(r) = \int_0^{2\pi} I(r,\varphi)d\varphi \tag{2.7}$$

According to the relationship between the r and 2θ, we could transform the $I-r$ relationship to $I-2\theta$ relationship:

$$I(r) \xrightarrow{r=D\tan 2\theta} I(2\theta) \tag{2.8}$$

2.4.3. Rietveld Refinement

Both the integrated diffraction patterns from SXRD and the 1D diffractograms obtained by lab XRD are analysed with the Rietveld refinement software MAUD [36, 37]. The refinement works by minimizing the weighted sum of squares WSS:

$$WSS = \sum_{i=1}^{i=N} w_i(I_{obs,i} - I_{calc,i})^2 \tag{2.9}$$

where $I_{obs,i}$ and $I_{calc,i}$ is the ith observed and calculated intensity respectively. w_i is the weight assigned to the ith sum of square, and for a standard x-ray powder diffraction pattern, $w_i = 1/I_{calc,i}$ [43]. For minimizing the WSS, the Levenberg-Marquardt Algorithm [44, 45] is implemented in MAUD. The weighted profile R-factor R_{wp} [46], following directly from the square root of the WSS minimized and scaled by the weighted intensities, is a parameter to assess the quality of the refinement, and

$$R_{wp} = \sqrt{\frac{\sum_{i=1}^{i=N}(I_{obs,i} - I_{calc,i})^2}{\sum_{i=1}^{i=N} w_i I_{obs,i}^2}} \tag{2.10}$$

Lutterotti [47] suggested that a good refinement for the cubic crystal structures would have a R_{wp} value less than 8%, while Toby [46] shows that R_{wp} value as a criterion for a good fitting is only suitable for low background levels.

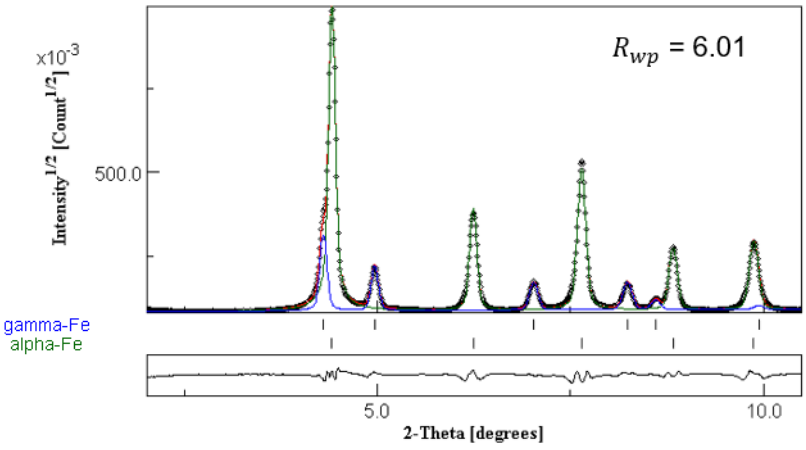

Figure 2.9: An example of the reduced data obtained at 25 °C and fitted with the program MAUD. The residuals are given below the profile fitting.

An example of the fitted $I-2\theta$ profile is presented in Figure 2.9. Very low background level exists in the diffractogram and the R_{wp} is 6.01%, showing a good quality of fitting. The

austenite (gamma-Fe in the figure) profile and ferrite (alpha-Fe in the figure) profile are shown separately and their peak positions are represented by the tick below the fitted profile. The volume fraction and lattice parameter of each phase can be extracted from each fitted profile, which helps to study the evolution of phase fractions and carbon content.

2.4.4. Spotty Rings and Spiky Peaks

During austenitisation, when a grain in the steel is too large, it will appear as a large spot on the area detector instead of being a part of a ring. An example of one spotty 2D XRD profile is shown in Figure 2.10 and its corresponding 1D XRD diffractograms is shown in Figure 2.11. It is clear that the peak is not smooth: it appears that the peak splits into several peaks. The spiky peaks would result in larger R_{wp} during refinement, as will shown later in Chapter 3.

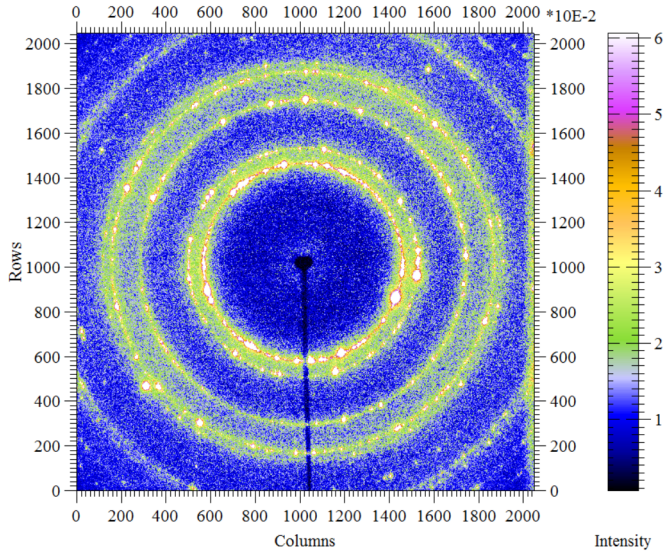

Figure 2.10: An example of spotty 2D XRD profile at 1000 °C

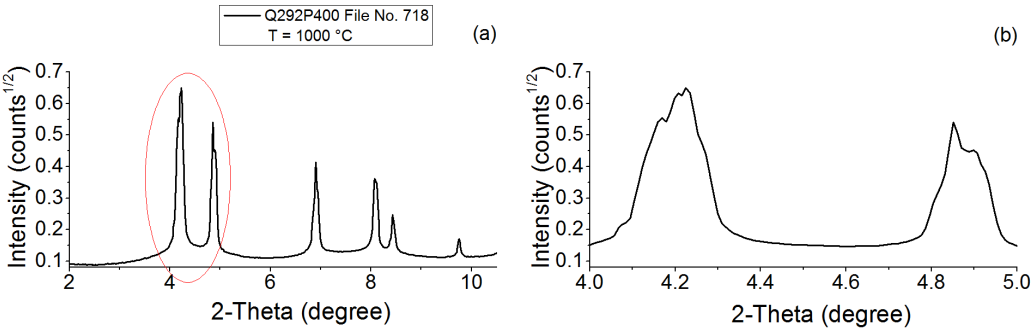

Figure 2.11: (a) The 1D diffractograms obtained by data reduction of the File No. 718 of Q292P400 at 1000 °C. (b) The enlarged image of the red-circled area in (a).

3

Results

3.1. Transformation Temperatures and Quenching Temperature Selection Methodology

In order to select the austenitising temperature, quenching temperature and partitioning temperature, it is necessary to estimate the A_{c1}, A_{c3}, M_s and B_s temperature using empirical equations. The A_{c1}, A_{c3}, M_s and B_s [48–51] temperature are calculated as follows:

$$\begin{aligned} A_{c1}(°C) &= 723 - 16.9(\text{wt.\%Ni}) + 29.1(\text{wt.\%Si}) + 6.38(\text{wt.\%W}) \\ &\quad - 10.7(\text{wt.\%Mn}) + 16.9(\text{wt.\%Cr}) + 290(\text{wt.\%As}) \\ &= 749.1 \end{aligned} \tag{3.1}$$

$$\begin{aligned} A_{c3}(°C) &= 955 - 350(\text{wt.\%C}) - 25(\text{wt.\%Mn}) + 51(\text{wt.\%Si}) \\ &\quad + 106(\text{wt.\%Nb}) + 100(\text{wt.\%Ti}) + 68(\text{wt.\%Al}) - 11(\text{wt.\%Cr}) \\ &\quad - 33(\text{wt.\%Ni}) - 16(\text{wt.\%Cu}) + 67(\text{wt.\%Mo}) \\ &= 912.0 \end{aligned} \tag{3.2}$$

$$\begin{aligned} M_s(°C) &= 462 - 273(\text{wt.\%C}) - 26(\text{wt.\%Mn}) \\ &\quad - 16(\text{wt.\%Ni}) - 13(\text{wt.\%Cr}) - 30(\text{wt.\%Mo}) \\ &= 329.4 \end{aligned} \tag{3.3}$$

$$\begin{aligned} B_s(°C) &= 656 - 57.7(\text{wt.\%C}) - 75(\text{wt.\%Si}) - 35(\text{wt.\%Mn}) \\ &\quad - 15.3(\text{wt.\%Ni}) - 34(\text{wt.\%Cr}) - 41.2(\text{wt.\%Mo}) \\ &= 389.5 \end{aligned} \tag{3.4}$$

The calculated M_s and B_s using Eq. (3.3) and Eq. (3.4) are close to the findings of Bhadeshia [52] for the Fe–3Mn–2Si–C (wt.%) series steels considering the error bars in Figure 3.1, from which it is shown that when carbon content is 0.2 wt.%, $M_s = 357 \pm 20$ °C and $B_s = 427 \pm 20$ °C. However, for more precise determinations of transformation start temperatures, in-situ experiments such as dilatometry should be performed.

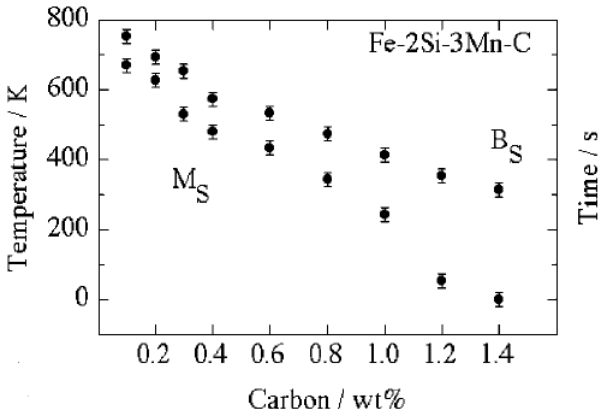

Figure 3.1: Calculated transformation start temperatures in Fe–2Si–3Mn steel as function of carbon concentration [52].

Before the heat treatment, a model [11] based on the Koistinen-Marburger (K-M) equation [53] was used for both quenching temperature selection and the estimation of RA fraction at a given quenching temperature. In this model, the volume fraction of primary martensite ($V_{\alpha_1'}$) is firstly calculated using the K-M equation:

$$V_{\alpha_1'} = 1 - \exp(-\beta(M_s - T_q)) \tag{3.5}$$

where $V_{\alpha_1'}$ is the volume fraction of primary martensite and T_q the temperature to which the steel is quenched. The parameters β depends on the chemical composition [50] of the steel according to:

$$\begin{aligned}\beta = {} & 0.0224 - 0.0107(\text{wt.\%C}) - 0.0007(\text{wt.\%Mn}) \\ & - 0.00005(\text{wt.\%Ni}) - 0.00012(\text{wt.\%Cr}) - 0.0001(\text{wt.\%Mo})\end{aligned} \tag{3.6}$$

According to Eq. (3.6), the parameter β is calculated to be 0.01816. By substituting the value of M_s and β into Eq. (3.5), the evolution of martensite volume fractions during quenching is obtained as in Figure 3.2 (a).

The model assumes full partitioning and precludes any competing reactions. Therefore, no phase transformation is expected and during the partitioning step, all the carbon atoms in the primary martensite are assumed to partition completely into the austenite. With this assumption, we can obtain the value of C_γ at the end of carbon partitioning from the matter balance of carbon atoms before and after partitioning:

$$C_i = (1 - V_{\alpha_1'})C_\gamma \tag{3.7}$$

where C_i is the carbon content in the bulk material. Since the carbon content in austenite has changed after the partitioning step, a secondary martensite-start temperature M_{s2} can thus be calculated using Eq. (3.3) again. Similarly, the parameter β should be recalculated according to the enriched carbon content in austenite.

There exists a optimal QT according to this model. Below this temperature, too much austenite is consumed during initial quenching. Above this temperature, the carbon partitioning into austenite is not enough to stabilise the austenite, resulting in the formation of

fresh martensite during the final quenching, thus decreasing the fraction of austenite. This optimal temperature T_0 is obtained when no fresh martensite will form during the final quenching, which requires

$$M_{s2} = 25 \tag{3.8}$$

T_0 can be solved using Eq. (3.3), Eq. (3.7) and Eq. (3.8), and $T_0 = 225.7\,°C$. If $T_q < T_0$, the austenite obtained after initial quenching can be fully retained during the final quenching, therefore the volume fraction of RA V_γ would only depend on $V_{\alpha_1'}$:

$$V_\gamma = 1 - V_{\alpha_1'} - V_{\alpha_2'} \tag{3.9}$$

If $T_q > T_0$, the formation of fresh martensite α_2' during final quenching needs to be considered, which can be obtained by applying Eq. (3.5) again:

$$V_{\alpha_2'} = (1 - \exp(-\beta_2(M_{s2} - 25)))(1 - V_{\alpha_1'}) \tag{3.10}$$

It should be noted that the K-M equation in Eq. (3.10) is applied to the volume fraction of austenite at the end of the initial quenching, i.e. $1 - V_{\alpha_1'}$. Also, the quenching temperature is set to be 25 °C. Therefore, the volume fraction of RA can be obtained as:

$$V_\gamma = 1 - V_{\alpha_1'} - V_{\alpha_2'} \tag{3.11}$$

Following the steps from Eq. (3.5) to Eq. (3.11), we can obtain the relationship between the volume fraction of RA and the quenching temperature as in Figure 3.2. The maximum volume fraction of RA is estimated to be around 15.2 vol.% when initially quenched to 225.7 °C. However, it should be noted that this methodology is simplified with assumptions of full partitioning and exclusion of competing processes that may happen during the Q&P process, e.g. bainite formation and carbide precipitation. The influence of carbon partitioning kinetics [54] is also not taken into consideration.

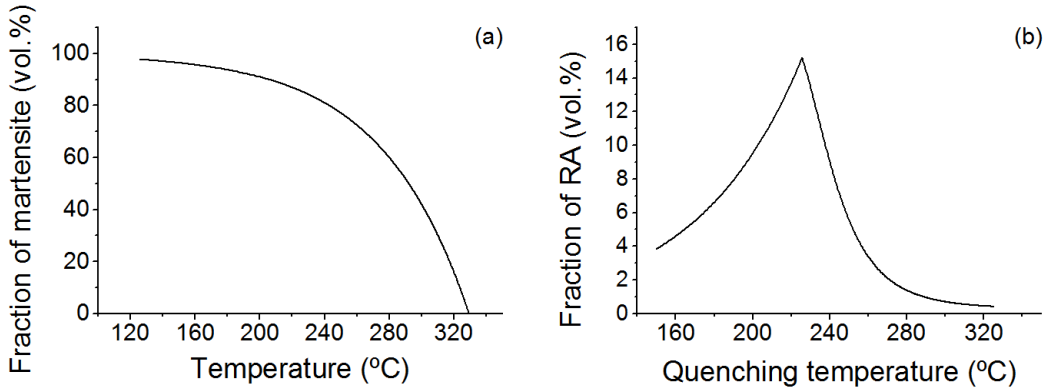

Figure 3.2: Prediction of final austenite fraction with different quenching temperatures applied using the methodology in reference [11].

3.2. Preliminary Heat Treatments

Based on the calculated transformations temperatures and the K-M equation, a set of preliminary heat treatments were performed in the dilatometer, and the details of the thermal cycles are shown in Figure 3.3. A direct quench experiment was conducted before the Q&P processes. The steels were firstly heated from room temperature to 1000 °C at a rate of 5 °C/s, and then fully austenitized at this temperature for 300 s. The maximum cooling rate of the dilatometer 150°C/s was used during the initial quenching. Three QTs, 240 °C, 275 °C and 300 °C are selected in the expectation that 80 vol.%, 60 vol.% and 40 vol.% primary martensite (α_1') can be obtained (Eq. 3.5) after the initial quenching, respectively. Afterwards, the steels were isothermally held for 3 s, and then reheated to the PT at rate of 5 °C/s. For each QT, three PTs were selected, namely, 400 °C, 450 °C and 500 °C. An exception existed in the specimens partitioned at 500 °C that 310 °C was selected instead of 240 °C for the QT. For each Q&P thermal cycle, the partitioning time was set to be 500 s. After the isothermal holding, specimens were quenched to room temperature at the maximum cooling rate. Each thermal cycle and the associated specimen are named according to the applied PT and QT, e.g. Q240P400 refers to a specimen which has been heated treated using a Q&P process with QT = 240 °C and PT = 400 °C. The direct quench process and the associated specimen are referred to as Full quench.

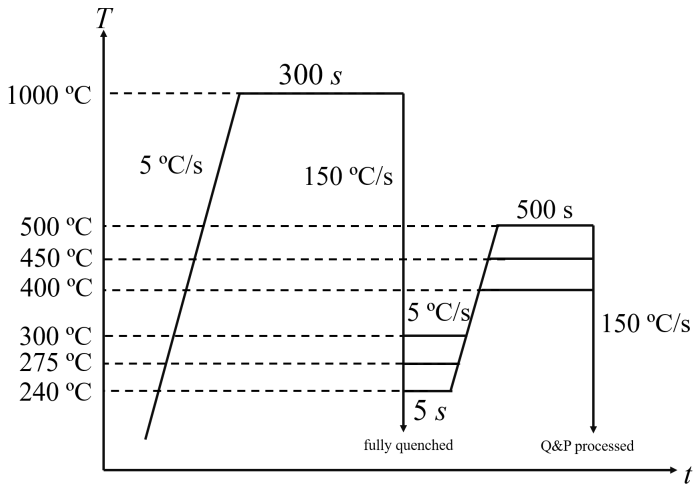

Figure 3.3: Thermal cycles of the preliminary dilatometry tests.

3.2.1. Microstructure Characterization

In Figure 3.4, the specimen quenched to 240 °C, 275 °C and 300 °C have similar microstructures, where martensite laths can be clearly distinguished and some martensite laths are more etched than others.

No RA lath can be distinguished from the martensite in these micrographs, while small amount of carbides can be clearly resolved with 5000× magnification, implying that carbides precipitated from the martensite during the reheating or partitioning step. A higher density of carbides is observed in Q240P400 than that in Q275P400 and Q300P400, while Q300P400 contains the least carbides in the microstructure. Therefore, higher undercool-

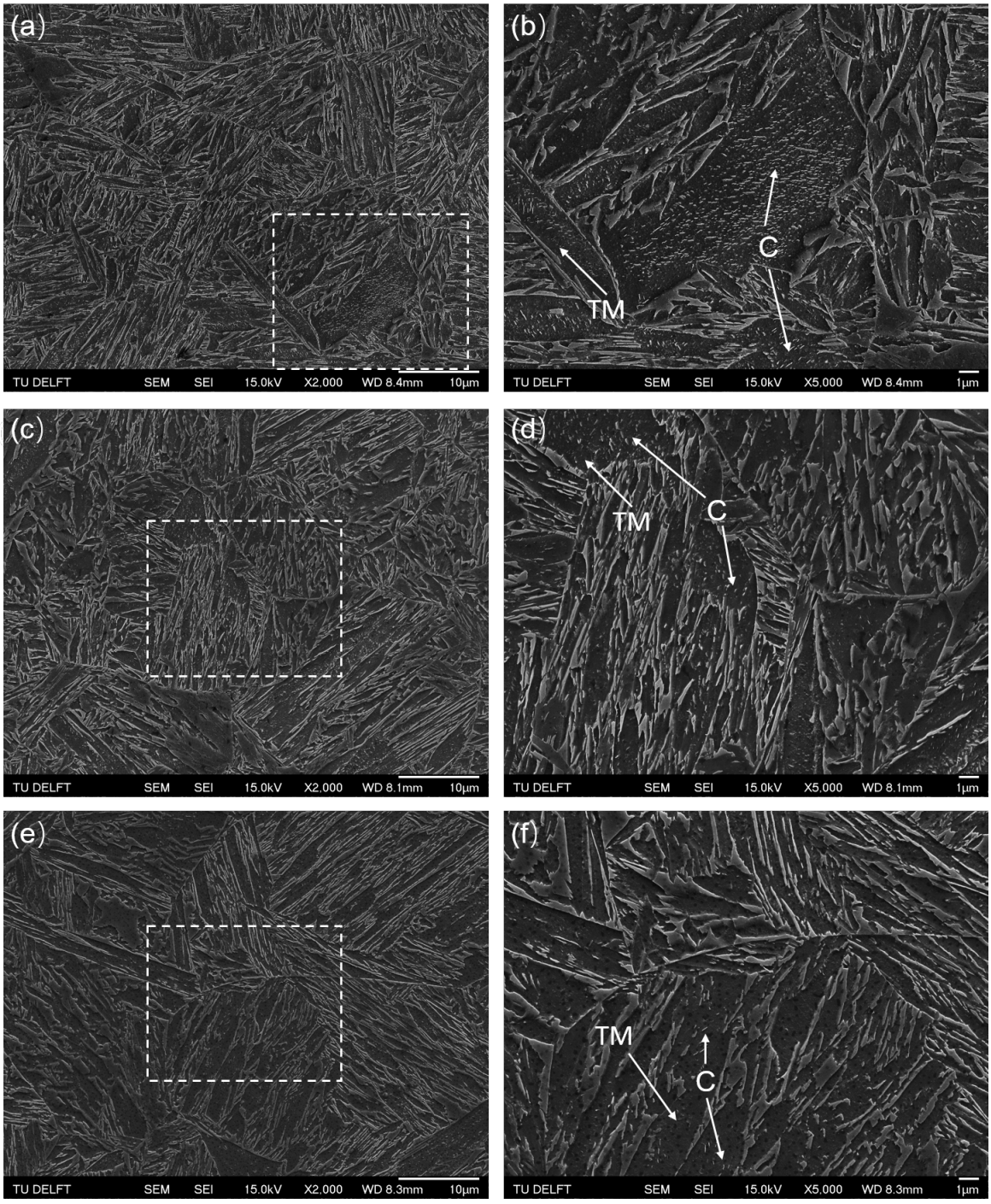

Figure 3.4: (a),(c),(e): Microstructures of Q&P processed specimen quenched to 240 °C, 275 °C and 300 °C respectively. All specimens are partitioned at 400 °C. (b), (d), (f): The enlarged images of the squared area in (a), (c) and (e) respectively. Carbides are represented by C and tempered martensite by TM.

ing leads to more carbides precipitation. The microstructures of the P450 series[1] are quite similar to that of the P400 series except that some fresh martensite can be clearly distinguished in the micrographs; carbides in the specimen quenched to 300 °C are hardly visible in the 5000 × magnification, while the carbides in the other specimens can be resolved

[1] See Figure A.2 for details of P450 series and Figure A.3 for details of P500 series.

in this magnification. The microstructures of the P500 series[1] look different with the presence of more fresh martensite in the micrographs; carbides cannot be resolved in the 5000 × magnification for all three specimens tempered at 500 °C.

3.2.2. Dilatometry Curves and Phase Fractions

From a set of Full quench experiments and using the lever rule described in Section 2.2, the martensite fraction as a function of temperature can be calculated using the dilatometry data of the full quenched samples as in Figure 3.5. It is seen that compared to the K-M equation, the results calculated with lever rule deviate about 3 – 10 vol.%. The results calculated with lever rule also exibit large error bars, especially at temperatures around 300 °C (up to 20%). The actual QTs achieved in the dilatometer are ~ 1.5 – 3°C lower than the preset QTs, the influence of which on the volume fraction of austenite or martensite is limited. Therefore, the specimens can still be considered as quenched to the preset QTs. The Q240, Q275, Q300 and Q310 would then have a martensite fraction of 89 ± 6 vol.%, 73 ± 12 vol.%, 46 ± 19 vol.% and 31 ± 20 vol.%, respectively.

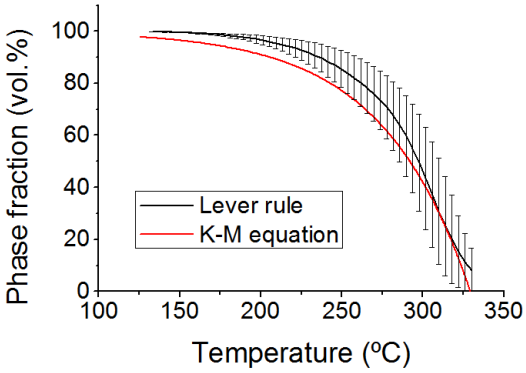

Figure 3.5: Evolution of martensite fraction as a function of temperature during quenching. Results obtained by lever rule using the experimental data is compared with the results obtained using K-M equation. For each of the three dilatometry data, the lever rule is performed. Therefore, three sets of fraction vs. temperature data can be obtained. The data obtained in this figure is averaged from the three sets of data, with standard deviation being the error bar. Only error bars of some data points are shown in the figure for better visualisation.

Figure 3.6 gives an overview of the strain of each Q&P processed specimen. Using the offset method to the dilatometry curves obtained in the preliminary heat treatments, the M_s is calculated to be 342 ± 8 °C.[2] Figure 3.6 (a)-(c) present the three specimens quenched to different temperatures and partitioned at 400 °C. All three samples show a noticeable dilatation during the short holding after direct quenching. The specimen Q300P400 shows a non-linear dilatation during reheating to partitioning temperature, which implies a phase transformation, e.g. austenite decomposition to bainite, while the other two specimens show a linear dilation during this stage. During the final quenching, all three samples contracted linearly, and no secondary M_s could be observed.

The specimens partitioned at 450 °C share similar patterns with the P400 series (Figure 3.6 (d)-(f)), with a dilatation during the interval before the reheating and initial quenching. The specimens quenched to 240 °C and 275 °C also show a linear dilation during the

[2]The M_s determined for each specimen are shown in Table A.1 in Appendix A.

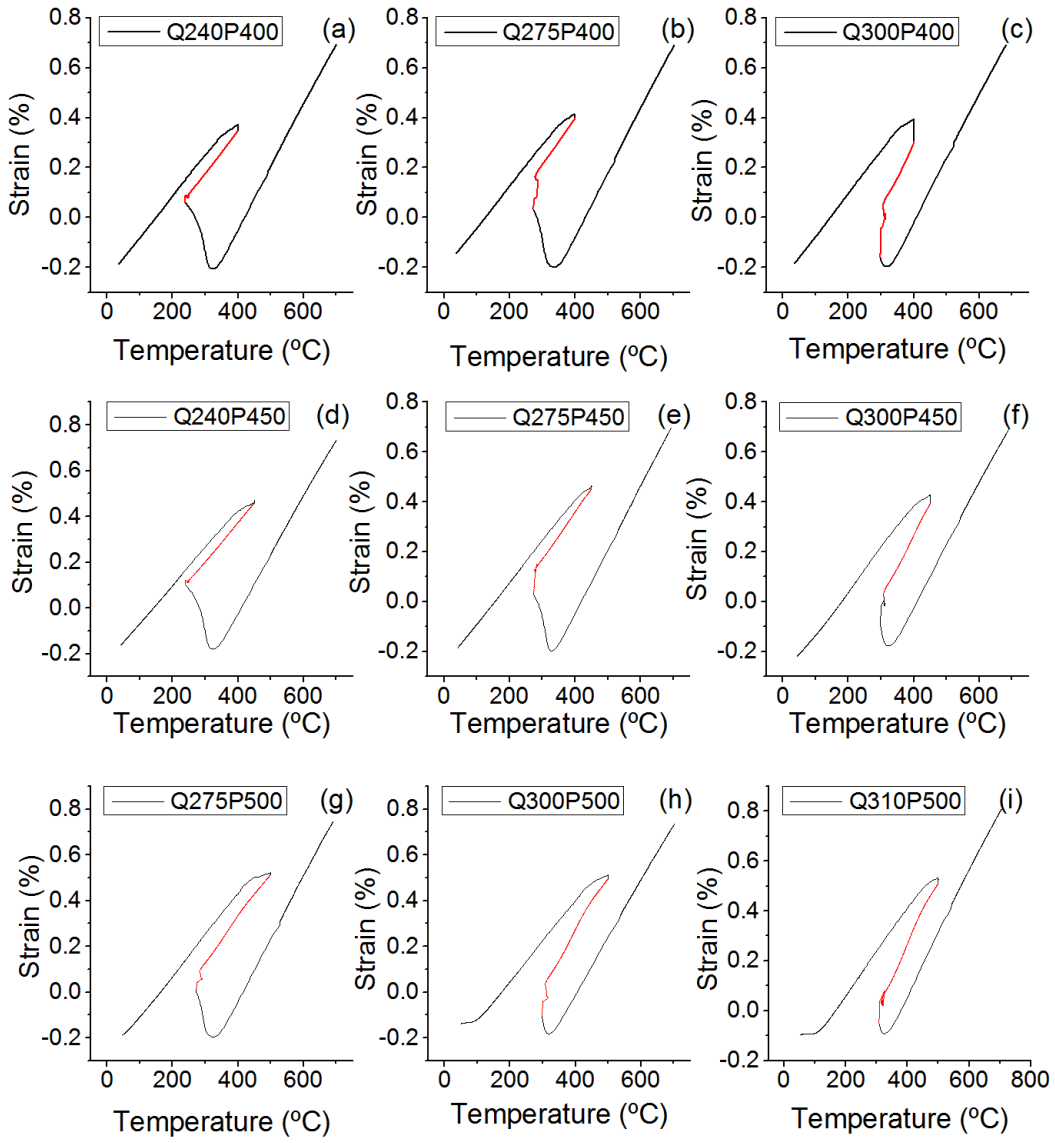

Figure 3.6: (a)-(c) Changes in length for specimens partitioned at 400 °C after initially quenched to 240 °C, 275 °C and 300 °C, respectively. (d)-(f) Changes in length for specimens partitioned at 450 °C after initially quenched to 240 °C, 275 °C and 300 °C, respectively. (g)-(i) Changes in length for specimens partitioned at 500 °C after initially quenched to 275 °C, 300 °C and 310 °C, respectively.

reheating while Q300P450 shows a non-linear dilatation during this stage. During the final quenching, Q240P450 and Q275P400 contracted linearly while Q300P400 contracts non-linearly, with a secondary M_s observed at around 100 °C. Figure 3.6 (g)-(i) show the three samples quenched to different temperatures and partitioned at 500 °C. All three samples showed a dilatation during the interval before the reheating and initial quenching and contracted non-linearly during the final quenching, with a secondary M_s temperature observed at around 100 °C for samples Q300P500 and Q310P500, and at around 50 °C for Q275P500.

The strain vs. time diagram gives more details on the lengths changes during the short holding and reheating. An example is shown in Figure 3.7 for Q300P400, also shown is the

achieved thermal cycle in the dilatometer. Instead of a short isothermal holding for 5 s, the temperature in the dilatometer firstly held from time point 1 for around 2.5 s and then fluctuated, with a sudden temperature increase from time point 2 to 3, during which the steel expanded suddenly. The temperature fluctuation should be related to the sudden changes in the atmosphere of the dilatometer.[3] The other eight specimens show similar temperature fluctuations during the short holding. Apart from the dilation due to the sudden increase in temperature, the dilation of the specimen before the fluctuation is observable, implying the austenite transforms to bainite or martensite directly after the initial quenching. Also noticeable is that despite the temperature decrease after the sudden increase, the specimen still expanded. At the end of this "short holding", the temperature increased to that of time point 3 approximately. Therefore, the strain due to phase transformation during the temperature fluctuation can be calculated as the difference between the strain at time point 3 and strain at time point 4. During this "short holding", the relative strain (the length change with reference to the length at time point 1) due to phase transformation is about 0.32%, which can be associated with the formation of about 35% BCC phase (bainite or martensite).

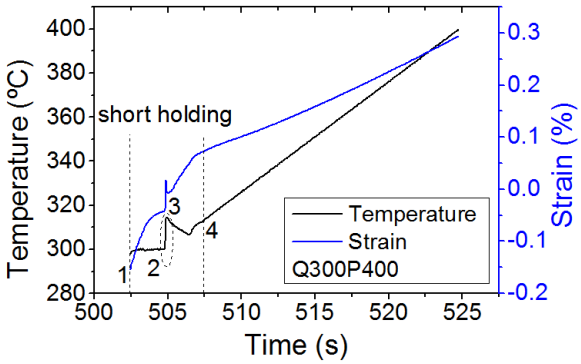

Figure 3.7: The strains vs. time and temperature vs. time of Q300P400 during the short holding and reheating. The dashed-circle area shows a sudden increase of temperature.

Figure 3.8 shows the changes of lengths with time during the partitioning step. $t = 0$ s is set at the beginning of the partitioning. The dilatations during the isothermal holding in all samples indicate the formation of BCC phase during the partitioning step, which could be associated with the growth of martensite or formation of bainite. The dilation during this stage might be a continuous phase transformation from the short holding and reheating stage. The Q300P400 had the largest dilation (0.095%) during the isothermal holding, which relates to formation of about 9% martensite or bainite. The other specimens had overall dilations ranging from less than 0.01% to 0.04%, which corresponds to $\sim 1-4\%$ formation of martensite or bainite. Contraction also happened for specimens Q240P450 and Q275P450 after partitioning for approximately 100 s and 200 s respectively, which could imply formation of carbides in martensite or the tempering of martensite; there is also a contraction for Q275P500 observed several seconds after the isothermal holding began; for the other specimens, no carbides formation or tempering of martensite can be interpreted from the dilatometry curves.

[3] In the preliminary heat treatments, the atmosphere changes from helium to vacuum after the initial quenching. Similar heat treatments were repeated but the atmosphere changes at the beginning of partitioning, and there was a temperature fluctuation observed at the beginning of partitioning.

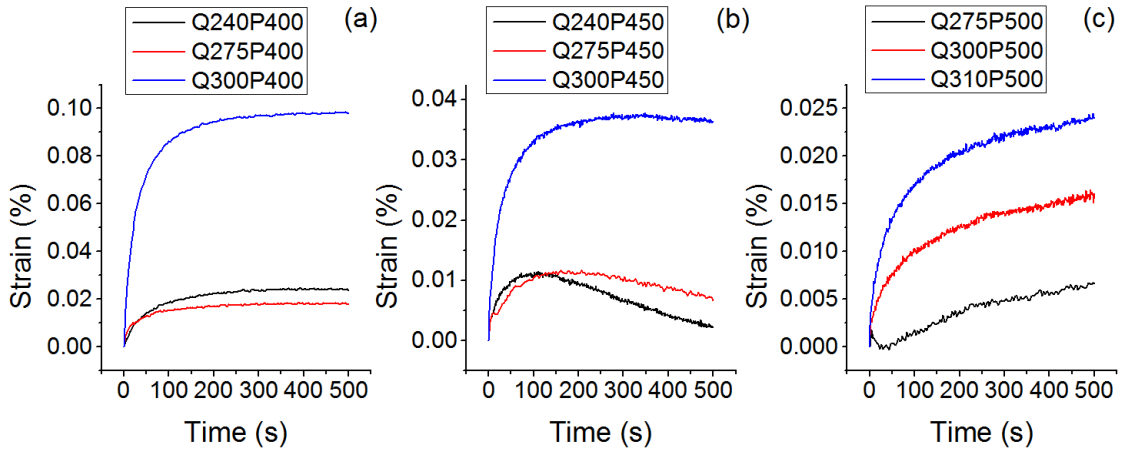

Figure 3.8: Overview of the changes in lengths of specimens partitioned for 500 s at (a) 400 °C, (b) 450 °C and (c) 500 °C, respectively. The strain is calculated over the length just before the partitioning step and time 0 is set at the beginning of the partitioning.

It is apparent now that during the short holding, reheating and the isothermal holding, an amount of BCC phase or phases will form, with carbides precipitation for some specimens. Denoting this phase product by α_2, primary martensite by α'_1, the fresh martensite formed during the final quenching by α'_2, and retained austenite by γ_r, the volume fraction of phase product X by f_X, then from the microstructural balance:

$$f_{\alpha'_1} + f_{\alpha_2} + f_{\alpha'_2} + f_{\gamma_r} = 1 \tag{3.12}$$

Due to the low density of carbides observed in the SEM micrographs of all specimens, the fraction of carbides is included in $f_{\alpha'_1}$ and not calculated separately. To calculate the volume fraction of the BCC phase(s) formed during this stage, we can use the microstructural balance as in Eq. (3.12). Since $f_{\alpha'_1}$ has already been calculated using the lever rule, now $f_{\alpha'_2}$ and f_{γ_r} are needed.

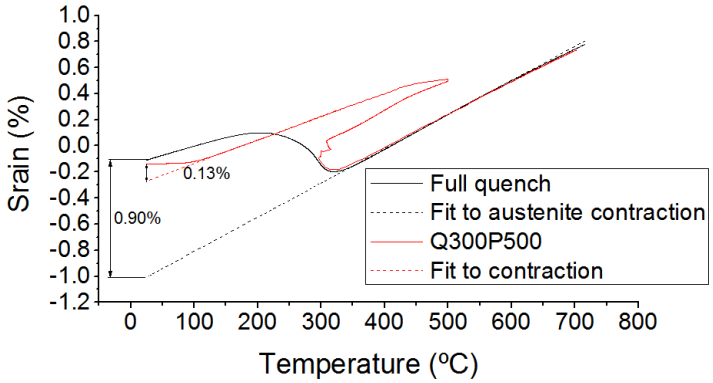

Figure 3.9: An example for the quantification of fresh martensite for the process Q300P500. The linear contraction of Q300P500 is fitted by the red dashed line, and the linear contraction of the austenite during the full quench is fitted by the black dashed line. The net dilation due to the martensitic transformation is therefore the difference between the experimental value and the fitted value.

In order to quantify $f_{\alpha'_2}$, the dilation due to the formation of fresh martensite of each Q&P processed specimen in Figure 3.6 are compared to that of the fully quenched specimen

in Figure 3.5 (a). An example was given in Figure 3.9. The linear contraction of austenite during the full quench is fitted, and the difference between the experimental value and the fitted value is calculated as the net dilation due to formation of martensite, which equals 0.90%. According to XRD, the volume fraction of retained austenite in the fully-quenched specimen is approximately 1%. Hence, the net dilation of 0.90% would correspond to formation of 99% martensite. Similarly, the net dilation due to martensitic transformation of Q300P500 can be calculated to be 0.13%, which is associated with the formation of 14.3% martensite. Since linear contraction are observed during the final quench for the P400 series as well as Q240P450 and Q275P450, they will have no fresh martensite in the microstructure. $f_{\alpha'_2}$ is calculated to be 4.4%, 5.8% and 16.7% for Q300P450, Q275P500 and Q310P500, respectively.

For the determination of f_{γ_r}, lab XRD experiments were performed. The obtained diffractograms are summarized in Appendix B.1 and they are fitted using MAUD as described in Section 3.2.3. From the program MAUD, the volume fraction of RA and lattice parameter of austenite a_γ can be extracted. a_γ can be related to the chemical compositions according to [55]:

$$a_\gamma = 3.556 + 0.0453x_C + 0.00095x_{Mn} + 0.0056x_{Al} \tag{3.13}$$

where x_C, x_{Mn} and x_{Al} represent the weight percentage of C, Mn and Al in austenite, respectively. x_C can therefore be calculated through Eq. (3.13).

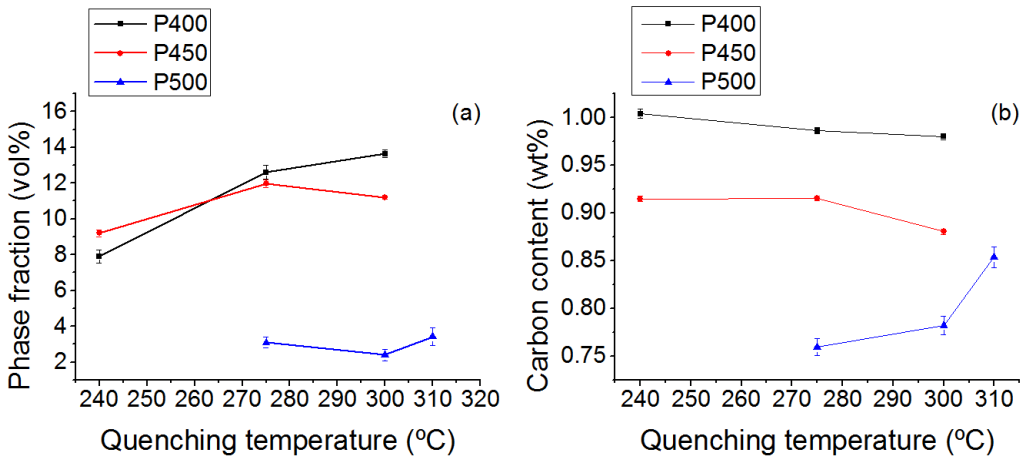

Figure 3.10: (a) The volume fraction of RA for different Q&P processed specimens. (b) The carbon content of RA for different Q&P processed specimens.

The volume fraction and the carbon content of RA are shown in Figure 3.10. The highest amount of RA was obtained for Q300P400. The P500 series retained the least austenite in the microstructure, ranging from 2 vol.% to 4 vol.%. As for the carbon content in the specimens, around 1.00 wt% is determined for the P400 series, around 0.90 wt% for the P450 series, and ranging from 0.75 wt% to 0.87 wt% for the P500 series.

Now that $f_{\alpha'_1}$, $f_{\alpha'_2}$ and f_{γ_r} for each specimen are known, f_{α_2} can be computed for each specimen. The results are shown in Figure 3.11, with phase fraction of each specimen.

The P400 series and P450 series share similar phase compositions at the same QT, except that there is formation of fresh martensite during the final quenching for Q450P300, which can be explained by the less carbon content in the P450 series than in P400 (Figure

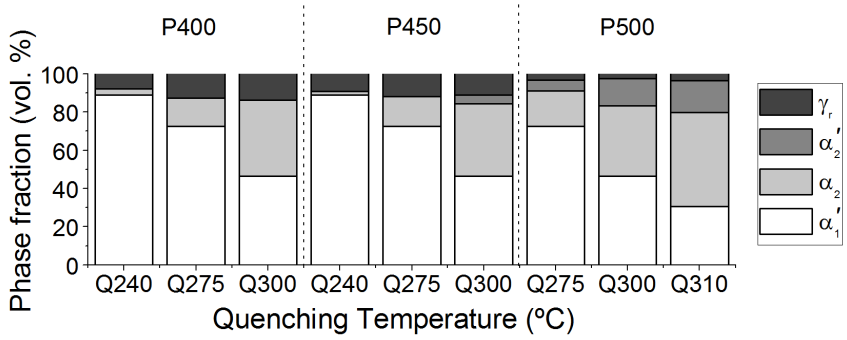

Figure 3.11: Phase fractions of different Q&P processed specimens. Primary martensite is denoted by α_1', the phase product formed during the short holding, reheating and isothermal holding by α_2, the fresh martensite formed during the final quenching by α_2', and retained austenite by γ_r. α_1' and α_2' are determined by dilatometry curves, and γ_r by XRD. α_2 is determined by microstructural balance $f_{\alpha_1'} + f_{\alpha_2} + f_{\alpha_2'} + f_{\gamma_r} = 1$.

3.10 (b)). The less carbon content in P450 series should resulted from carbides precipitation as observed by the dilatometry curves (Figure 3.8 (b)), which consumes carbon and thus leading to less carbon partitioning into austenite. The P500 series retained the least amount of RA and had the least carbon partitioning into austenite.

Therefore, with the same PT, the presence of less α_1' leads to more formation of α_2, relatively lower carbon content of RA and more volume fraction of RA when carbides precipitation is limited. However, the nature of the phase product(s) α_2 is not known. It is also unclear when the carbon enrichment in austenite occurred. In the following two sections, the steels are further studied for the unresolved questions.

3.3. Dilatometry Tests with Different Partitioning Time

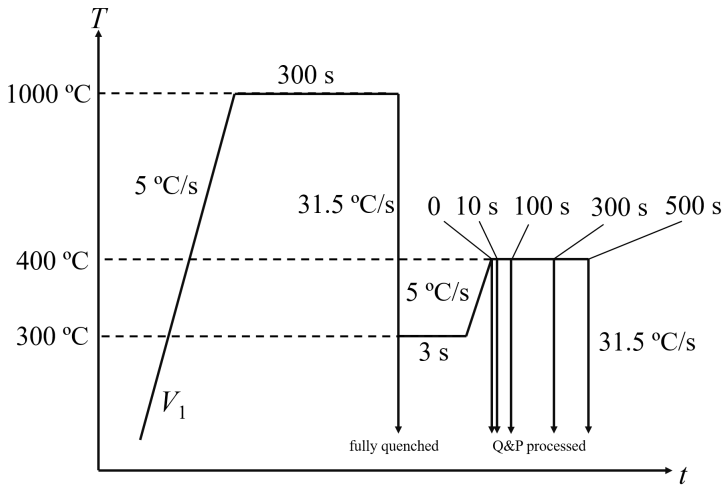

Figure 3.12: Thermal cycle of the dilatometry tests with different partitioning time.

In order to study the effect of different partitioning time on the final microstructure, a set of dilatometry tests with different partitioning time is designed. 300 °C and 400 °C are selected for QT and PT, respectively, since with the two parameters, the steel had a higher amount of RA and also higher carbon content of RA. At 400 °C, different partitioning time is selected, namely, 0 s, 10 s, 100 s, 300 s and 500 s. Separate from the Q&P process, a specimen is fully quenched, and the specimen and the process are named as Full quench. The Q&P processes and associated specimens are named according to the partitioning time, e.g. t_p10 signifies a Q&P process with a partitioning time of 10 s, or specimen partitioned with 10 s. The aim of t_p0 is to investigate to what carbon level will the RA be enriched when the steel is just heated to 400 °C, without any time of holding.

The details of the thermal cycles are shown in Figure 3.12. A cooling rate of 31.5 °C/s is chosen instead of the maximum value in order to reduce temperature fluctuation after the initial quenching. The short holding time is reduced to 3 s. Other process parameters are the same as in the preliminary heat treatments.

3.3.1. Microstructural Characterization

The aim of the SEM is to study when the carbides precipitated during the Q&P process. Figure 3.13 presents the SEM micrographs of all the specimens. The carbides observed in the fully quenched specimen should arise from auto-tempering, which refers to a process where the martensite formed near the M_s gets tempered during the remainder of the quench [23]. Small quantity of carbides have been resolved in all the specimens, implying that the carbides already precipitate during reheating from QT to PT. As the time of partitioning increases, no obvious increase in the quantity of carbides can be distinguished among the five Q&P processed specimens. The isothermal holding can therefore be regarded as a process without further carbides precipitation at 400 °C.

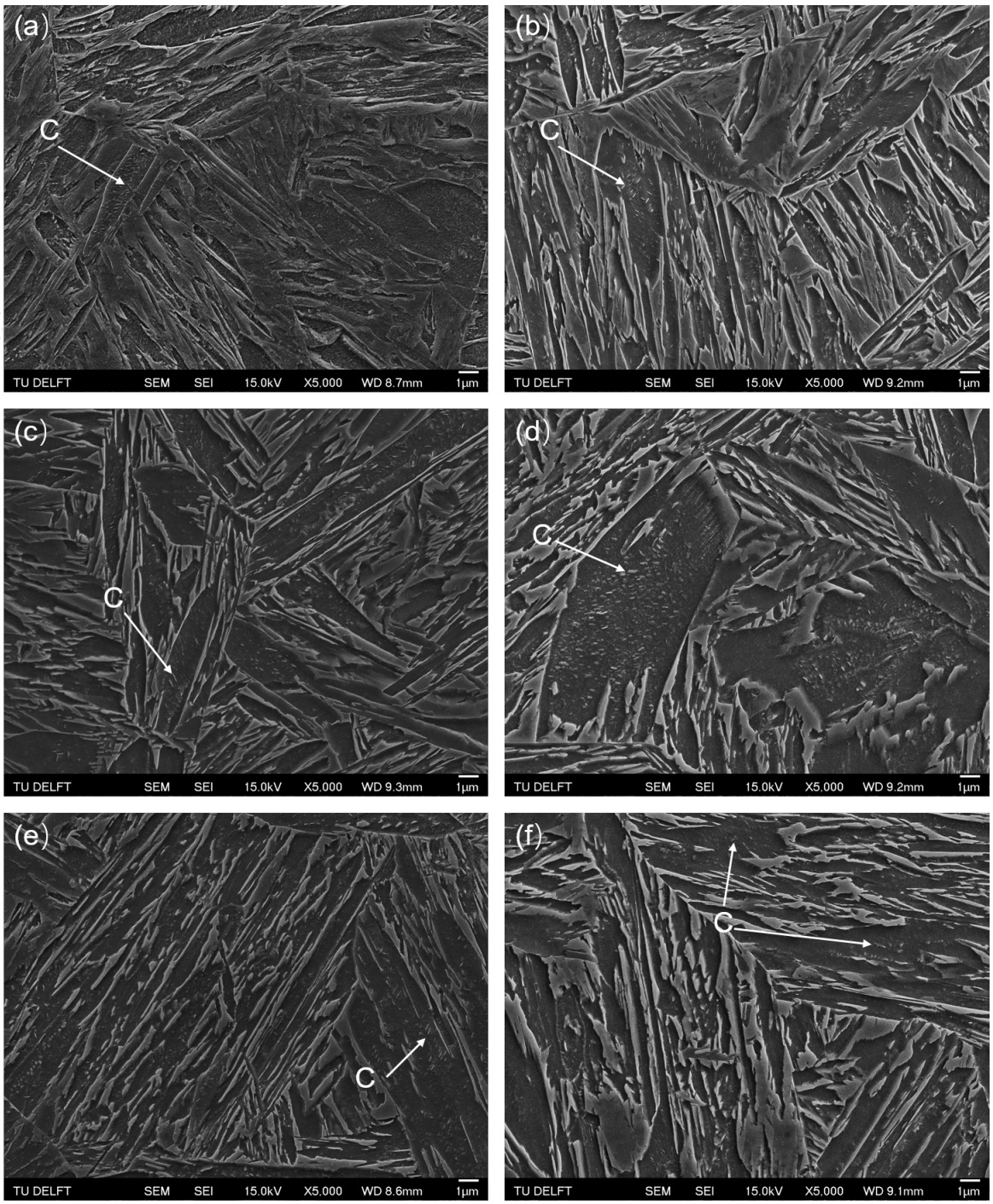

Figure 3.13: (a)-(f): Microstructure of the fully quenched specimen, t_p0, t_p10, t_p100, t_p300 and t_p500 respectively. Carbides are labelled by C.

3.3.2. Dilatometry Curves and Phases Fractions

Figure 3.14 gives an overview of the dilatometry curves of the five Q&P processed specimens with different partitioning time, with the strain vs. time diagrams given for the short holding, reheating and partitioning stage of t_p500. The strain vs. time diagrams for the short holding and reheating of other specimens are very similar, and therefore are not given in the figure. The strain vs. time diagrams for the partitioning stage of other specimens re-

semble part of the t_p500 curve and are also not shown in the figure. With a slower cooling rate than in the preliminary heat treatment, the temperature fluctuation is greatly reduced during the short holding (Figure 3.14 (b)). Similar to the preliminary heat treatment, a dilation was observed directly after the initial quenching. Also noticeable is the non-linear dilation during the reheating stage. All these confirmed a phase product of BCC structure formed during the short holding and reheating. The relative strain after 500 s of partitioning is around 0.085%, which is slightly smaller than the value obtained for Q300P400 during the preliminary heat treatment. At the end of the partitioning, there is still a growing trend for the strain with time, implying that phase transformation is not completed.

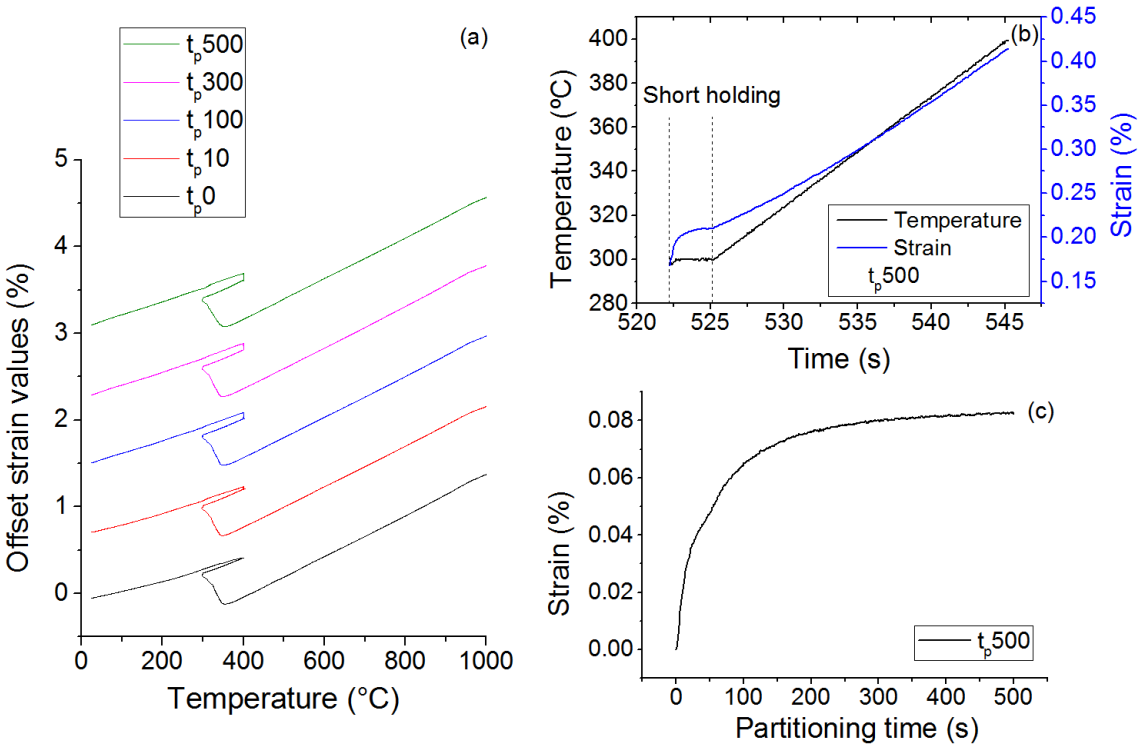

Figure 3.14: (a) Overview of the strains of the Q&P processed specimen. t_p10, t_p100, t_p300 and t_p500 are offset by a strain value 0.8%, 1.6%, 2.4% and 3.2%, respectively. (b) The strains vs. time and temperature vs. time diagram of Q300P400 during the short holding and reheating. (c) The normalised strain during the partitioning step. The strain is calculated over the length just before the partitioning step and time 0 is set at the beginning of the partitioning.

As in the preliminary heat treatment, we denote the phase product(s) formed during the short holding, reheating and isothermal holding by α_2, which is calculated by the microstructural balance. The quantification of the fresh martensite α_2' is achieved through the same procedure as in Figure 3.9, and $f_{\alpha_2'}$ calculated for each specimen is 3.5 – 11.0 vol.%.

Lab XRD is used to investigate the volume fraction of RA and the carbon content in RA for specimens processed with different partitioning time, t_P, with diffractograms shown in Figure B.4. The results are summarised in Figure 3.15. Even specimen with $t_P = 0$ can retain 8.5 ± 0.3 vol.% austenite in the final microstructure, and the corresponding carbon content is 0.87 ± 0.01 wt.%. The RA fraction of specimens processed with $t_P \geq 100$ s varies slightly from 13.4 ± 0.3 to 14.3 ± 0.2 vol.% and the peak value 14.3 ± 0.2 vol.% is obtained at $t_P =$ 300 s. The carbon content in the RA increases with the partitioning time. By comparing the

carbon content of RA in t_P0 and t_P500, it can be inferred that the carbon enrichment before the partitioning (from 0.2 wt% to 0.87 wt%) is even more than that during partitioning (from 0.87 wt% to 0.98 wt%).

Figure 3.16 summarises the phase fractions of each specimen. α_2' is present in all specimens, and $f_{\alpha_2'}$ decreases when t_p increases due to higher austenite stability. Both the carbon level and the volume fraction of RA obtained by t_p0 shows that carbon enrichment during the short holding and reheating is considerable, and carbon partitioning occurred well before the partitioning stage. f_{α_2} seems to vary slightly with different t_p. However, since it is calculated using the microstructural balance, the errors resulted from the other three fraction values will all contribute to the error of f_{α_2}, with α_1' being the largest source of error.

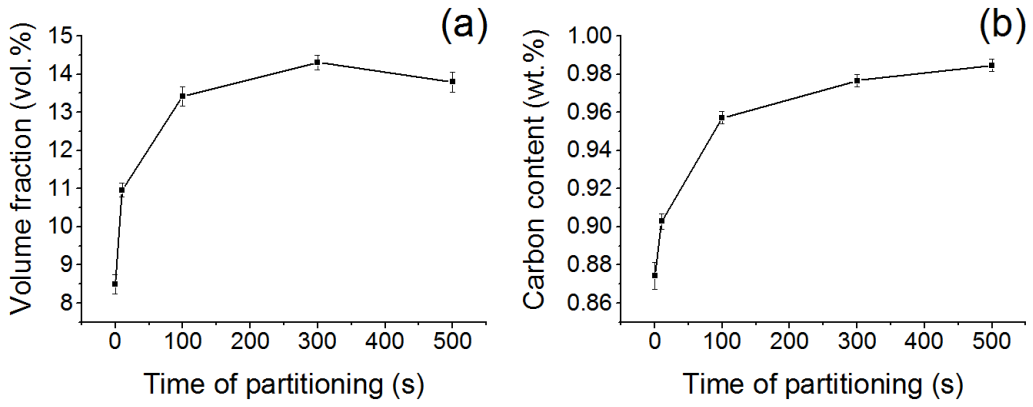

Figure 3.15: (a) Volume fraction of RA with different partitioning time. (b) Carbon content in the RA with different paritioning time.

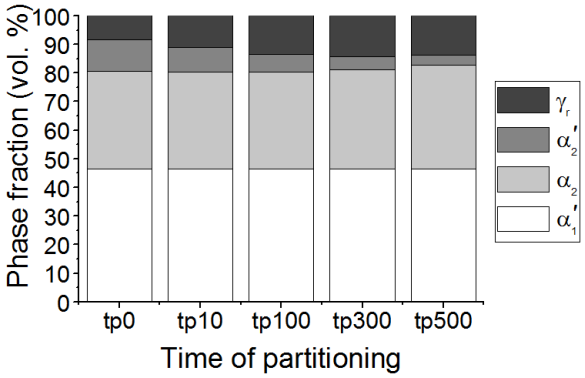

Figure 3.16: Phase fractions of specimens heat treated with different partitioning time. Primary martensite is denoted by α_1', the phase product formed during the short holding, reheating and isothermal holding by α_2, the fresh martensite formed during the final quenching by α_2', and retained austenite by γ_r. α_1' and α_2' are determined by dilatometry curves, and γ_r by XRD. α_2 is determined by microstructural balance $f_{\alpha_1'} + f_{\alpha_2} + f_{\alpha_2'} + f_{\gamma_r} = 1$.

3.4. In-situ SXRD experiments

The above two sections give information about how $f_{\alpha'_1}$ and t_p influence the final microstructure of the steels. However, it is not known how the microstructure evolved during Q&P process. In this section, a set of heat treatments were performed with the in-situ XRD scanning to study the microstructural evolution during the Q&P process. The process parameters are selected based on the results of the preliminary heat treatments. Similarly, PT is selected to be 400 °C as most carbon partitioning is expected, stabilising RA. QTs 240, 275 and 300 °C were initially selected, although 8−10°C lower than the preset QTs were achieved experimentally. Figure 3.17 depicts the details of the thermal cycles applied, with the actual QTs in place of the preset ones.

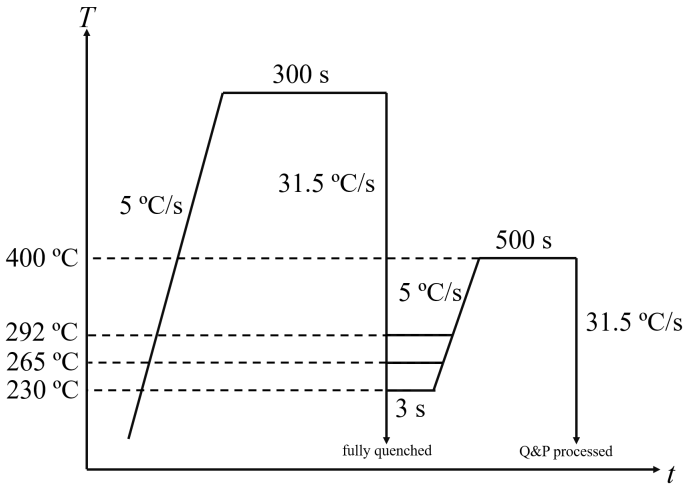

Figure 3.17: Thermal cycle of the in-situ SXRD experiments.

The obtained 2D XRD profiles were firstly reduced into 1D diffractograms using Fit2D, followed by Rietveld refinement using MAUD. Both data reduction and refinement started from the beginning of the initial quenching to the end of the final quenching for each specimen, and the R_{wp} values for the refinement are given in Figure B.3 (see Appendix B.2). Higher R_{wp} values were obtained for the initial quenching files since their peak profiles are less smooth (Figure 2.11). The reason for the spiky profile is that during austenitization, some of the austenite grains grow preferably and their large grain size cannot be considered as “powder” thereafter. Instead of contributing to the Debye-Scherrer rings, the large grain will appear as a large spot (Figure 2.10) on the area detector [56]. Error bars in this part are estimated from the program MAUD, or calculated based on the estimation of MAUD.

3.4.1. Microstructure Characterization

The microstructures of the Q&P processed specimens after the in-situ SXRD experiments are shown in 3.18. The microstructures of specimens quenched to 230 °C, 265 °C and 292 °C look quite similar, consisting of martensite that responded to the 2% nital etching in two different ways since some martensite laths are clearly more etched than others. No RA lath can be distinguished from the martensite in these micrographs, while small amount of carbides can be resolved with 5000× magnification. It is clear that the carbides in Q292P400 are less than that in Q265P400 or Q230P400, meaning a lower undercooling

would lead to less carbides precipitation.

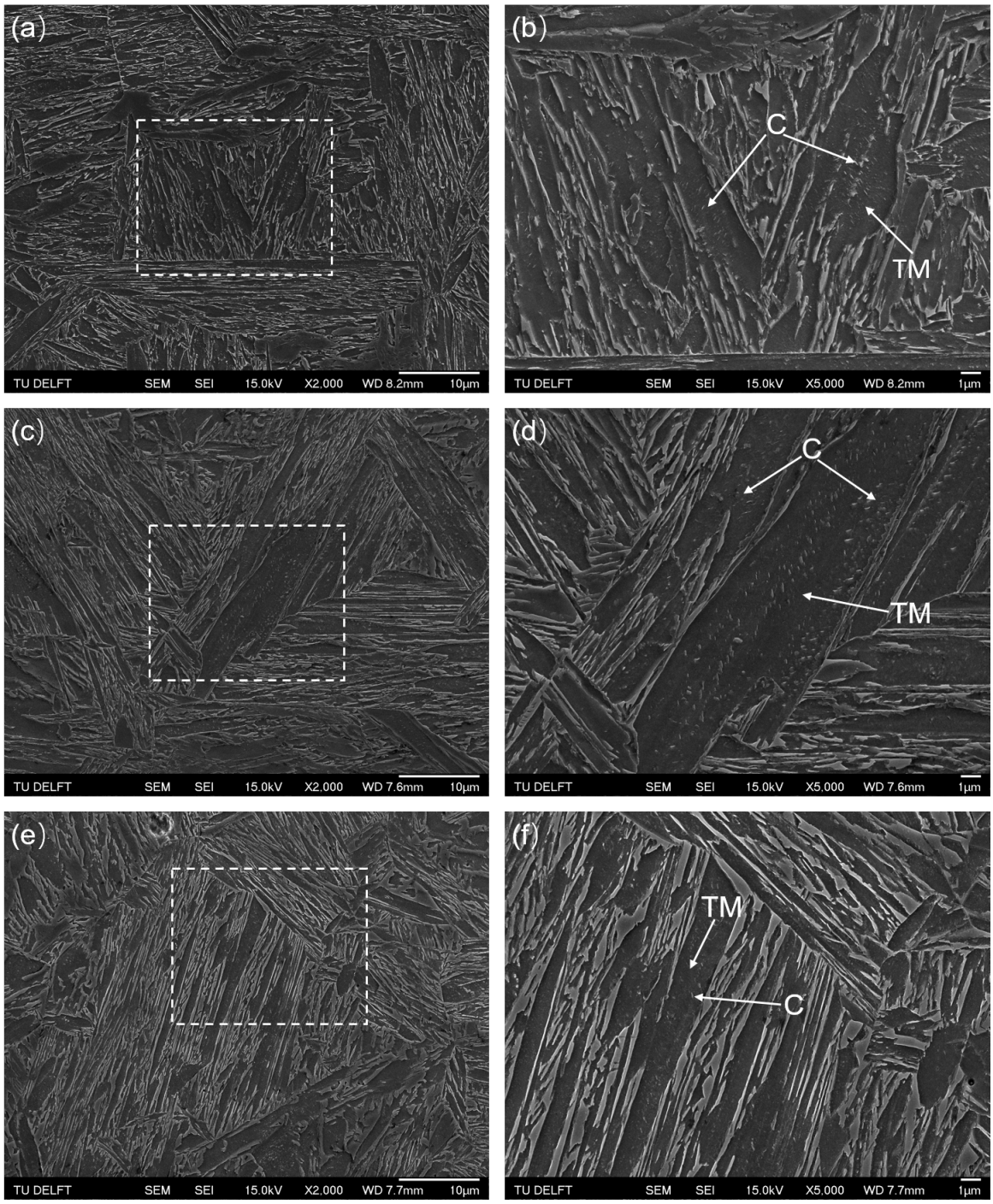

Figure 3.18: (a),(c),(e): Microstructures of Q&P processed specimen quenched to 230 °C, 265 °C and 292 °C respectively. All specimens are partitioned at 400 °C. (b), (d), (f): The enlarged images of the squared area in (a), (c) and (e) respectively. Carbides are represented by C and tempered martensite by TM.

3.4.2. Microstructural Evolutions during Initial Quenching

From the diffractograms (Figure 3.19) of the four specimens, it is found that some small fraction of BCC phase (α in the figure) formed at 803 °C, 807 °C, 709 °C and 816 °C for

full quench, Q230P400, Q265P400, Q292P400, respectively. This temperature range (709 – 816 °C) is far above the M_s or B_s temperature of the material, and therefore, the BCC phase formed at these temperatures could not be martensite or bainite. This temperature range (709 – 816 °C) is close to the Ae_3 temperature of the material (818 °C calculated by the Andrews Equation [48]). Since the Widmanstätten ferrite grows at a temperature in proximity to the Ae_3 [57, 58], the ferrite formed high above the M_s or B_s is considered to be Widmanstätten ferrite.

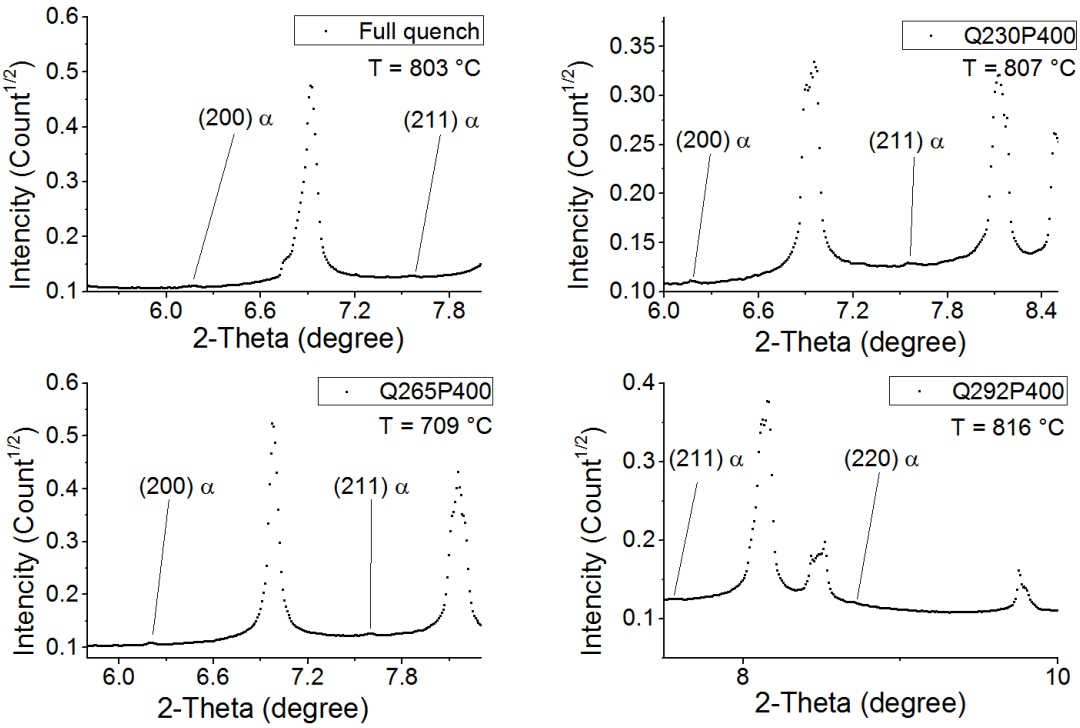

Figure 3.19: XRD diffractograms showing the first observation of ferrite peaks for specimen Full quench, Q230P400, Q265P400 and Q292P400 in the in-situ XRD experiments, respectively.

Figure 3.20 presents the evolution of austenite volume fraction (f_γ) for the four specimens during the full quench or initial quenching. The shape of the four curves resemble the "S"-shaped curve in Figure 3.5 determined by the lever rule, even though the austenite transformed well before the M_s in all four specimens. By examining both the evolution of austenite volume fraction and the change in the length of the specimen as measured by the ETMT, we can determine when the fast decomposition of austenite begins. Figure 3.21 compares the rate in length change with the phase evolution of the specimen Q292P400. The rate of length change firstly stabilized at around 0.0003 when quenching from 1000 °C to 420 °C, during which the austenite transformed slowly by a volume fraction of about 7%. Then a sudden decrease in the rate of contraction can be observed in Figure 3.21 (a), which corresponds to a fast γ to α transformation. This has also been observed in Figure 3.21 (b) by a much faster decrease in the volume fraction of austenite (7% when quenching from 420 °C to 390 °C compared to 7% when quenching from 1000 °C to 420 °C).

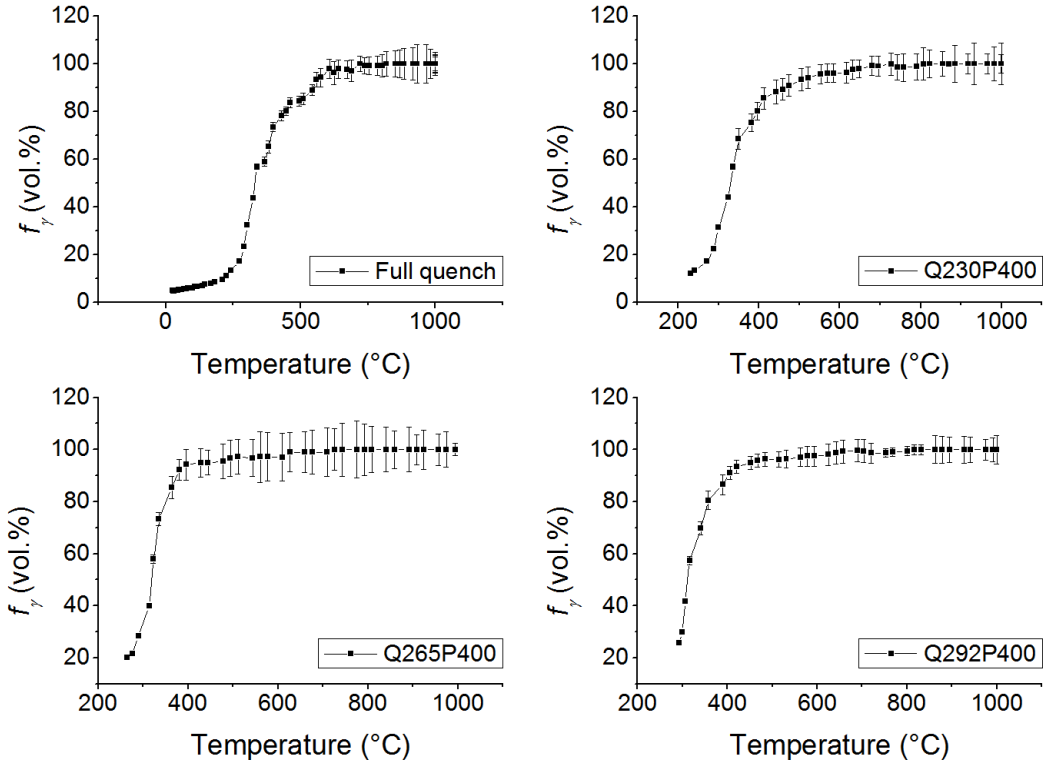

Figure 3.20: Evolution of austenite fraction for different specimens during the initial quenching. The legend in each figure corresponds to specimen Full quench, Q230P400, Q265P400, Q292P400 respectively.

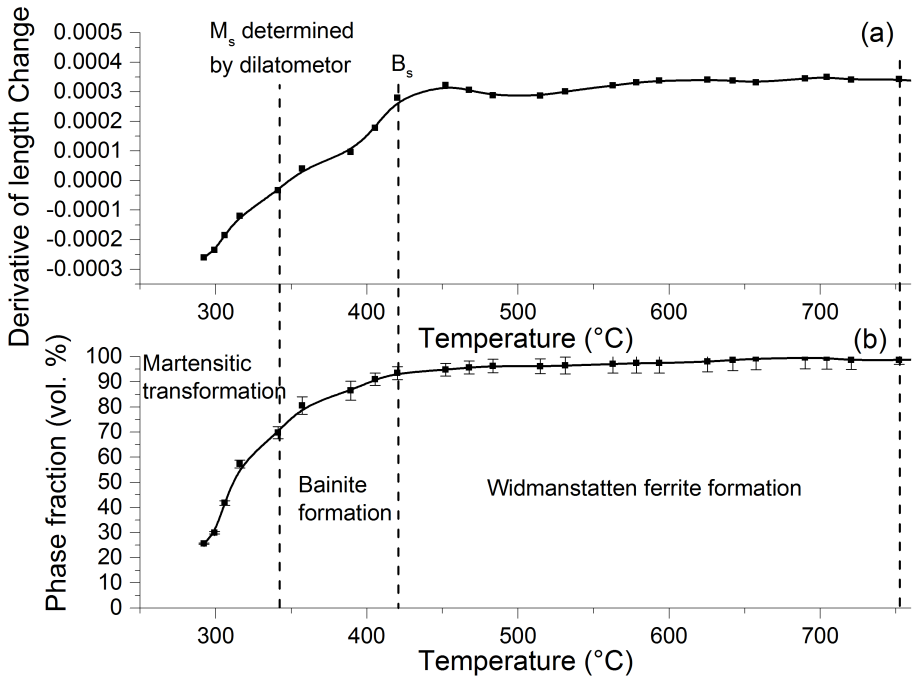

Figure 3.21: (a) The first derivative of length change of the specimen to temperature. The length change are measured by the position reader of ETMT. (b) The evolution of austenite volume fraction for the specimen Q292P400.

However, this temperature is higher than the M_s ($342 \pm 8\,°C$) determined in Section 3.2.2 and close to the B_s. Therefore, the 420 °C should be identified as the B_s for specimen Q292P400. Similarly, B_s has been identified for the other three specimens as in Appendix C.1. The phase compositions can therefore be obtained as in Figure 3.22.

Similar amount (5.0−6.6 vol.%) of Widmanstätten ferrite (α_W) formed for Q292P400 and Q265P400 during the initial quenching, while α_W is higher for Q230P400. The amount of bainite formed ranges from 15.7 to 23.4 vol.%. Due to more formation of Widmanstätten ferrite and bainite before cooling to M_s, Q275P400 has almost the same amount of primary martensite as Q230P400. But still, the amount of austenite decreases with the QT.

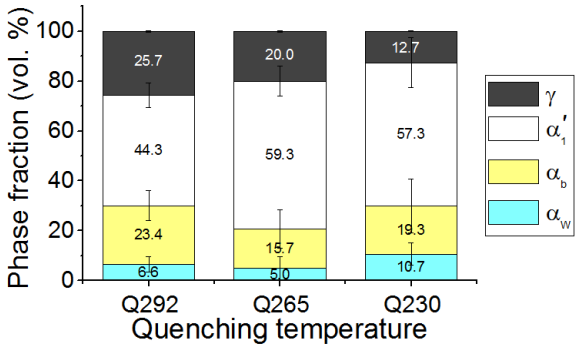

Figure 3.22: Phase fractions of specimens quenched to different temperature and partitioned at 400 °C. Widmanstätten ferrite is denoted by α_W, bainite by α_b, prior athermal by α'_1 and austenite by γ.

Figure 3.23 gives an overview of the changes in lattice parameters during initial quenching for the four specimens. a_γ represents the lattice parameter of austenite and a_α the lattice parameter of ferrite. The lattice parameters of austenite are shown in the left column of Figure 3.23, where a decrease in the rate of contraction during quenching can be observed for all four specimens at around 400 °C, represented by the red data points. The decrease in the rate of contraction stopped at around 300 °C for Full quench, Q230P400 and Q265P400 while it stopped at 389 °C for Q292P400. An increase in the rate of contraction is observed in the corresponding temperature range for ferrite, as represented by the red data points in the right column of Figure 3.23. The observed phenomena should be related to the martensitic transformation since it has been reported that during standard quenching process, the martensite phase should be subject to tensile stress and the austenite should be in stress of the opposite sign (compressive stress) to satisfy the force balance [59].

The error bar of a_γ is within the size of the data point ($< 5 \times 10^{-4}$Å), while the large error bar of a_α at higher temperatures is due to the small volume fraction of α at these temperatures. Despite the small error of a_γ, there is an observable scatter from linear contraction at temperature range 700 - 1000 °C. The scatter may result from the spotty rings observed during the 2D diffractograms in this temperature range (Figure 2.10 and 2.11). The spotty rings will result in less smooth peak profiles and thus errors in the determination of a_γ. However, this is not reflected in the error bar of a_γ determined by the program MAUD, since the error bar is only estimated from the fitting in the program; the spikes that appear in the peak profiles are not taken into considerations.

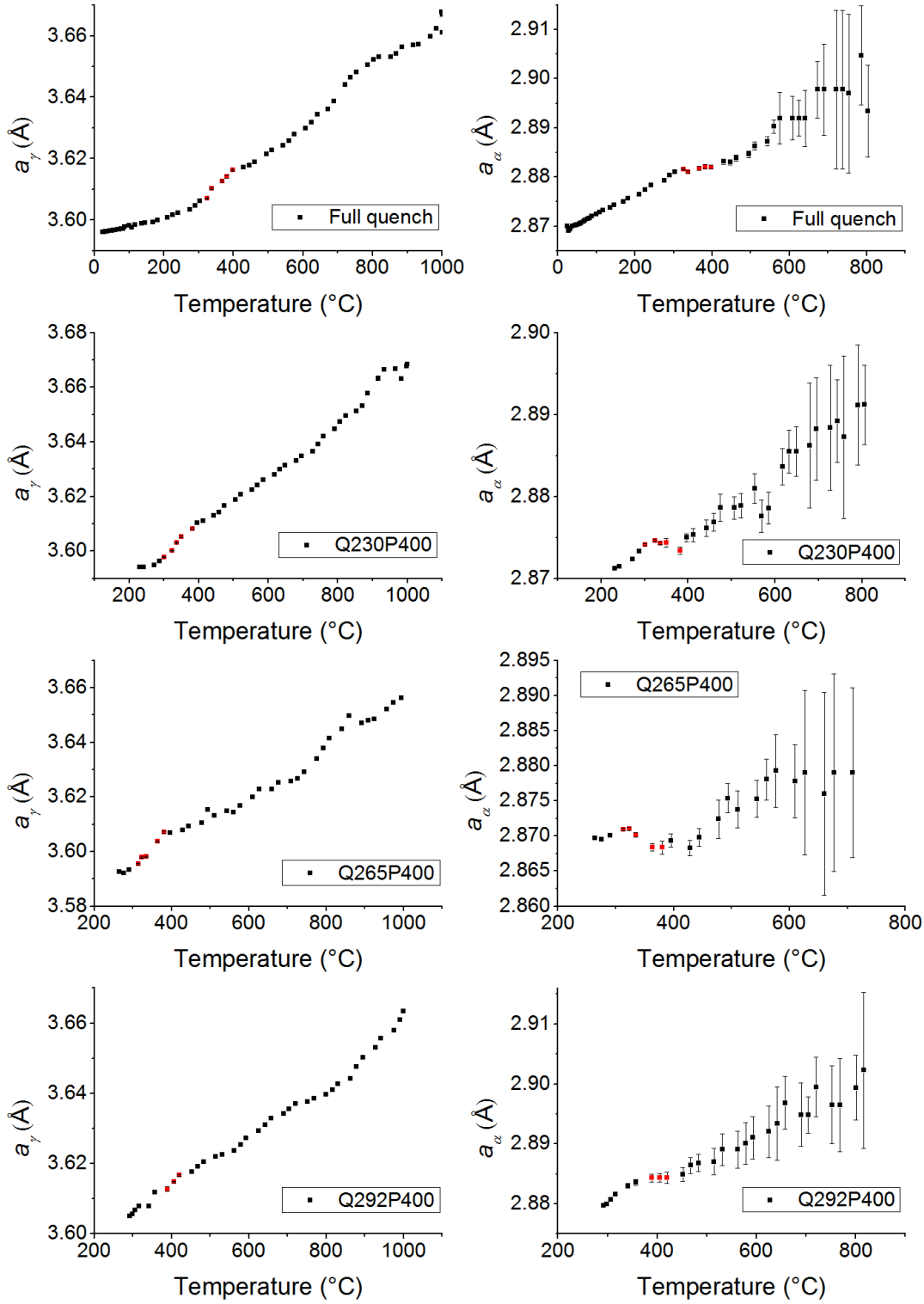

Figure 3.23: Evolutions of lattice parameters during the initial quenching. The four figures on the left column corresponds to the lattice parameters of austenite for Full quench, Q230P400, Q265P400 and Q292P400, respectively. The four figures on the right column corresponds to the lattice parameters of ferrite for the four specimens. The data marked by red color represent a change in the rate of contraction during the quenching.

3.4.3. Microstructural Evolutions during the Short Holding and Reheating

Figure 3.24 shows that the volume fraction of austenite decreased with the increase of temperature (a) or time (b), signifying that austenite transforms to a BCC phase (or phases)

through this stage. The results obtained by the SXRD experiments confirmed the finding of the dilatometry tests that austenite still transforms after the initial quenching stops. As in the dilatometry tests, the BCC phase formed during this stage, as well as the BCC phase formed during the partitioning step, is referred to as α_2. During this stage, more consumption of austenite is observed for specimen with a higher f_γ at t = 0 because of higher QT.

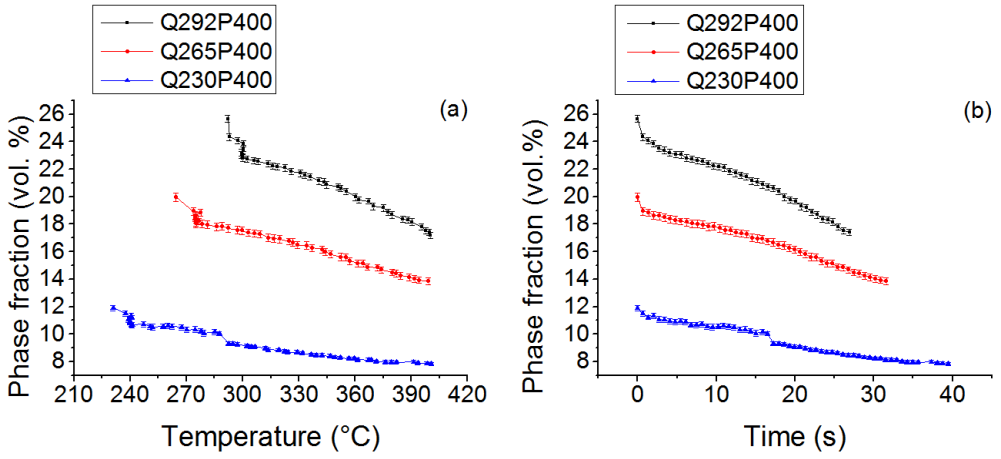

Figure 3.24: (a) Evolution of austenite volume fraction during the reheating stage with the increase of temperature. (b) Evolution of austenite volume fraction during the reheating stage with time.

Figure 3.25 presents the evolution of lattice parameters during the reheating to the partitioning temperature 400 °C for the three specimens. The lattice parameters of austenite (a_γ) for all three specimens experienced non-linear expansion during the reheating and the rate of expansion increased with temperature for Q265P400 and Q292P400. For Q230P400, the rate of expansion in a_γ increased until 360 °C, then decreased slowly upon further heating to 400 °C. By contrast, the lattice parameter of BCC phase (a_α) for all three specimens expanded linearly with increasing temperature. By fitting them linearly (See Figure C.7-C.9 in Appendix C), we could obtain the relationship between the lattice parameter a_γ and temperature T, and the results are summarized in Table C.1 (Appendix C).

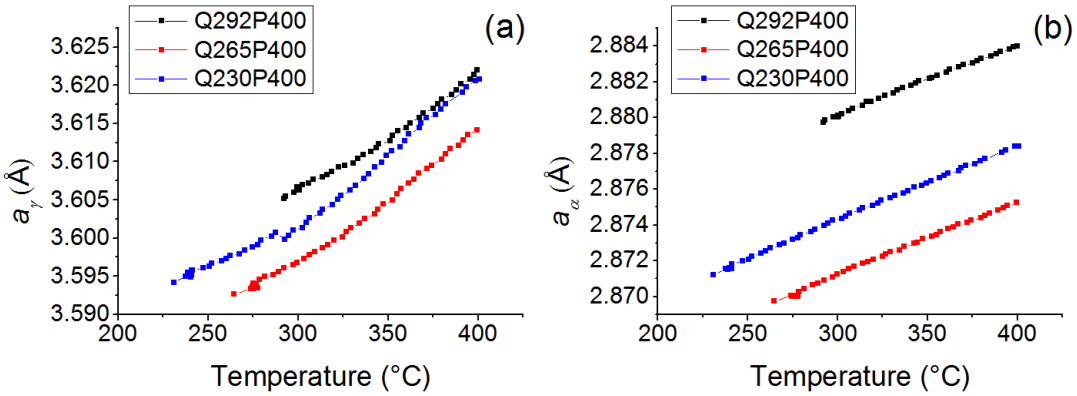

Figure 3.25: (a) Evolution of the lattice parameter of austenite during the reheating to 400 °C. (b) Evolution of the lattice parameter of ferrite during the reheating to 400 °C.

The R^2 values for the three fittings are very close to 1, and therefore a linear expansion

rate of $\sim 4 \times 10^{-5}$ can be extracted for a_α. However, from this linear expansion, it is not possible to calculate the amount of carbon partitioned away from the BCC phase. This might result from the fact that for the sake of simplicity, in the current work, all BCC phases are treated as α. The determination of the peak positions and thus a_α will be less accurate since the α peak is composed of peaks of martensite, bainite and ferrite. Therefore, only a_γ will be used for the quantification of carbon content.

The non-linear dilation of a_γ could be contributed from three processes: the thermal expansion during reheating, the release of stress from the previous martensitic transformation [59] or carbon atoms partitioning from the BCC phase into austenite.

Figure 3.26 (a) shows the evolution of a_γ for specimen Q230P400 quenched to 230 °C and then reheated to 400 °C, which presents more clearly the influence of the three contributions on a_γ during the reheating. The error bars of both the initial quenching data and reheating data are within the size of the data points ($< 5 \times 10^{-4}$Å). The data in the initial quenching curve (a_γ^{quench}) before the martensitic transformation is fitted linearly, represented by the blue line in the figure and referred to as a_γ^{fit}. This line represents the dilation or contraction of austenite without strain or carbon partitioning process. The details of the fitting are given in Figure C.4-C.6 and the results are summarised in Table C.2. Once the martensitic transformation occurs, the difference between the blue line and the black data point can be considered as the contraction of a_γ due to the transformation strain. The expansion of a_γ during reheating is represented by the red dot (a_γ^{reheat}) in the figure, and as temperature increase, a_γ soon intercepts with the fitted line at point E. When the temperature is further increased, a_γ^{reheat} is greater than the a_γ^{fit}, implying that the carbon partitioning and/or stress release have compensated for the contraction induced by martensitic transformation. Therefore, in the area right to point E, the austenite is enriched by carbon atoms regardless of stress release or not.

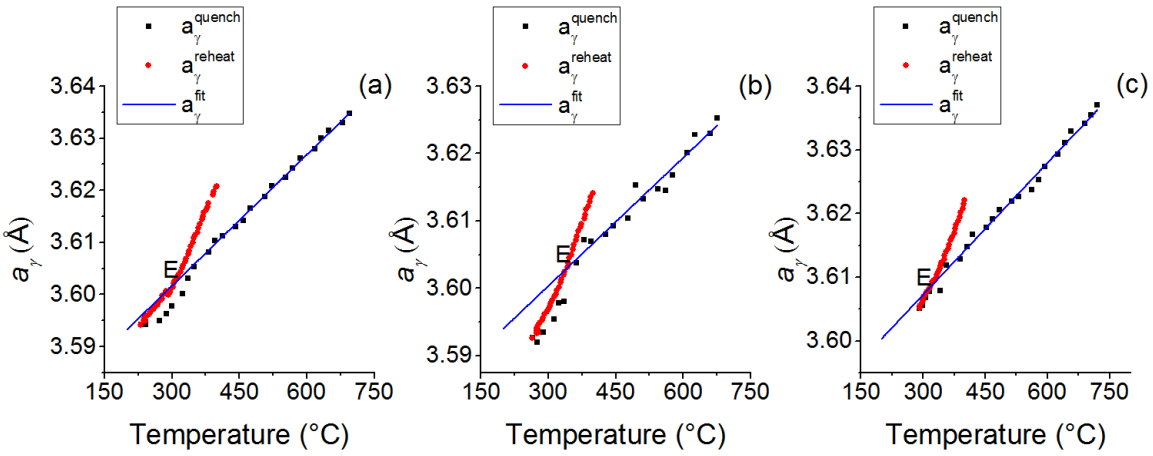

Figure 3.26: (a) a_γ of Q230P400 during initial quenching and reheating. (b) a_γ of Q265P400 during initial quenching and reheating. (c) a_γ of Q292P400 during initial quenching and reheating. The linear part of the data in initial quenching is fitted for each specimen.

However, since it is unknown how the transformation stress was released during the reheating, the data presented is not sufficient to calculate the evolution of carbon content in austenite during reheating. But still, we can estimate the the amount of carbon enriched

through the isothermal holding by looking at the beginning and the end of the reheating process:

- beginning of the reheating: stress has not been released and no carbon enrichment occurred. The carbon can be calculated using Eq. (3.13) after extrapolating the fitted line to $T = 25$°C.
- end of the reheating: The stress is assumed to be completely released at this point, the difference between a_γ^{reheat} and a_γ^{fit} can be regarded as the dilation due to the carbon enrichment. The carbon content can be calculated by Eq. (3.13) through the a_γ^{reheat} at room temperature ($a_{\gamma-RT}^{reheat}$), which can be expressed by:

$$a_{\gamma-RT}^{reheat} = a_{\gamma-T}^{reheat} - k^{fit}(T-25) \tag{3.14}$$

  where $a_{\gamma-T}^{reheat}$ is the lattice parameter of austenite at temperature T during reheating and k the slope of the fitted line. The k value is shown in Table C.2.

Therefore, for Q230P400:

- at $T = 230$°C, $a_\gamma^{reheat} = 3.5942 \pm 0.0005$Å, the corresponding a_γ^{reheat} at room temperature can be calculated by extrapolating the fitted line to room temperature and $a_{\gamma-RT}^{reheat} = 3.5784 \pm 0.0007$Å[4]. The carbon content thus can be calculated with Eq. (3.13) and $C_{\gamma-T=230}^{reheat} = 0.43 \pm 0.02$ wt%.
- at $T = 400$°C, $a_\gamma^{reheat} = 3.6208$ Å, and substituting this into Eq. (3.14), the corresponding a_γ^{reheat} at room temperature can be calculated to be $a_{\gamma-RT}^{reheat} = 3.5892 \pm 0.0007$Å, similarly, with Eq. (3.13), the corresponding carbon content is $C_{\gamma-T=400}^{reheat} = 0.67 \pm 0.02$ wt%. Hence, the carbon content in austenite increased by 0.24 ± 0.03 wt%[5] during the reheating process.

Similarly, to calculate the changes in the carbon content during reheating for the other two specimens, Figure 3.26 (b) and Figure 3.26 (c) are presented. There also exists the intersection point between the fitted line and reheating curve, implying that carbon enrichment happens right to point E, as analysed before. The results are summarised in Table C.3. The carbon content in austenite of Q265P400 and Q292P400 increased by 0.17 ± 0.06 wt% and 0.17 ± 0.04 wt%, respectively, during the reheating process.

3.4.4. Microstructural Evolutions during Partitioning

Figure 3.27 depicts the evolution of the austenite volume fraction and the changes in the lattice parameter of austenite during partitioning. A decrease in the austenite fraction has also been observed in the partitioning step, and the amount of transformed austenite decreases with lower starting austenite fraction : 1.0%, 2.2% and 4.5% austenite has transformed in the specimen Q230P400, Q265P400 and Q292P400, respectively. Moreover,

[4]The error (δ) of $kx+b$ equals $\sqrt{(k\delta x)^2+(\delta b)^2}$ if variable x and b are independent [60]. Since k here is the fitted slope in Table C.2, which is very small (in the order of 10^{-5}), the error of $kx+b$ would be δb, which is the error of the fitted intercept in Table C.2

[5]The error (δ) of $a-b$ equals $\sqrt{(\delta a)^2+(\delta b)^2}$ if variable a and b are independent [60].

all three specimens showed a similar pattern in the austenite transformation, that is, the volume fraction firstly decayed exponentially, and then linearly. During the exponential decrease in the austenite fraction, the lattice parameter of all three specimen increased rapidly despite the decreasing rate of expansion. Afterwards, a_γ of Q265P400 and Q292P400 tend to level off while a_γ of Q230P400 firstly reached a plateau and then experienced a slight decline. It is also apparent from Figure 3.27 that a_γ of Q230P400 was the first to reach the plateau, followed by Q265P400 and then Q292P400.

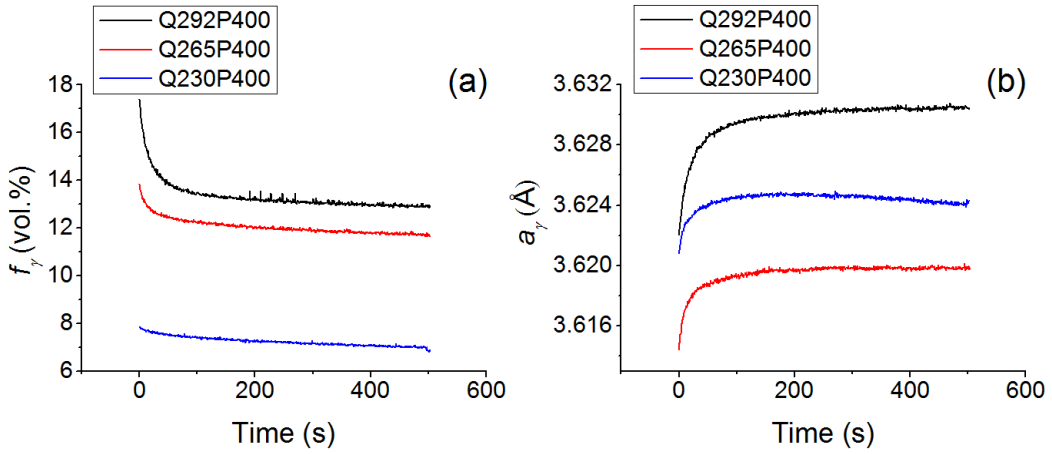

Figure 3.27: (a) Evolution of austenite fraction during the isothermal holding. (b) Changes in the lattice parameter of austenite during the isothermal holding.

To calculate the evolution of carbon content during isothermal holding, the lattice parameters of austenite at 400 °C are firstly extrapolated to 25 °C according to:

$$a_{\gamma-RT}^{partition} = a_{\gamma-t}^{partition} - k^{fit}(400-25) \tag{3.15}$$

where $a_{\gamma-RT}^{partition}$ and $a_{\gamma-t}^{partition}$ are the lattice parameter of austenite extrapolated to room temperature and the lattice parameter of austenite at a given partitioning time t. Data in Table C.2 (will be shown later) is used for k^{fit} with the assumption that stress due to martensitic transformation has been fully released during the reheating process. Therefore, the same k^{fit} can be used for $a_{\gamma-t}^{partition}$ at any time t. The corresponding carbon contents are calculated with Eq. (3.13) and the evolutions of carbon content in the austenite are then summarized in Figure 3.28 for each specimen.

It can be observed that with lower QT and therefore more primary martensite and less austenite at the beginning of isothermal holding, carbon stabilisation is faster to achieve. The observed lower carbon content for Q265P400 arises from the calibration error during the experiments and a deviation of -0.20 wt% is expected.[6] Therefore it is not recommended to compare the absolute carbon content between different specimens. The carbon enrichment in austenite during the partitioning step ranges from 0.13 to 0.20 wt.%, which is comparable to the difference between the carbon content of t_p0 and t_p500 (0.12 wt.%), confirming that during partitioning step, there is less carbon enrichment in austenite than before partitioning step.

[6]See Table B.2 in Appendix B for details.

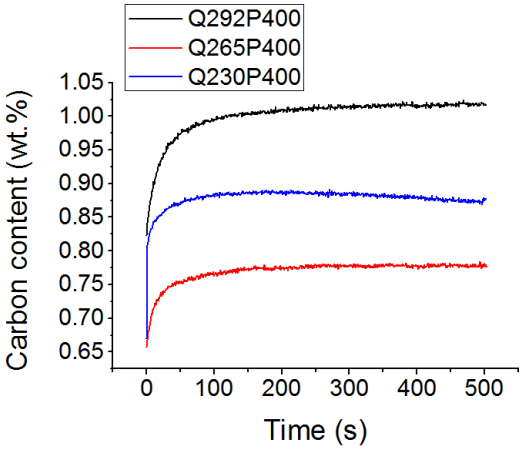

Figure 3.28: Evolution of average carbon content in the austenite in the three specimens during the partitioning step.

The lattice parameter of ferrite, on the other hand, decreased slightly during the isothermal holding, as shown in Figure 3.29. As stated in Section 3.4.3, a_α is not used for quantification, however, from Figure 3.29, it can still be inferred that carbon partitioned away from the BCC phase during the isothermal holding.

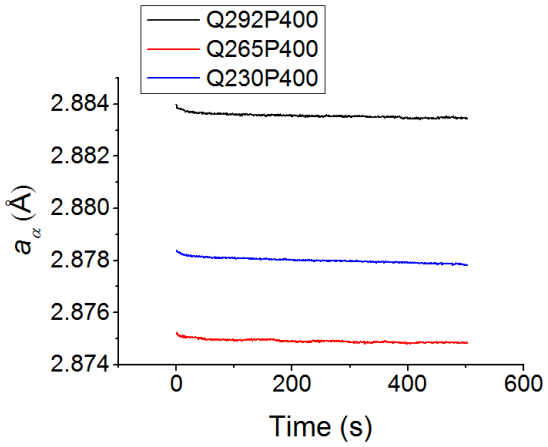

Figure 3.29: Changes in the lattice parameter of ferrite during the isothermal holding.

3.4.5. Microstructural Evolutions during Final Quenching

Figure 3.30 shows the evolution of austenite volume fraction quenched from 400 °C to room temperature and it can be shown that the austenite fraction for all three specimens barely changes during the final quenching and therefore no fresh martensite forms. The thermal stability of austenite is therefore very high after the partitioning step in all three specimens. The fully-quenched specimen, on the other hand, retained about 4.5 vol% of austenite, which is higher than that retained for the fully-quenched specimen in the dilatometry tests (1 vol%). One possible reason for this is that during quenching, Widmanstätten ferrite and bainite formed, therefore enriching the austenite before the martensitic transformation.

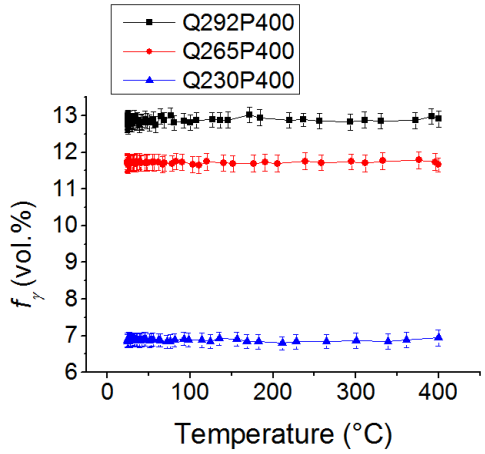

Figure 3.30: Evolution of austenite fraction during the final quenching.

The contraction of austenite and ferrite are presented by the changes in their lattice parameters as in Figure 3.31. Linear contraction with temperature are observed for both a_γ and a_α.

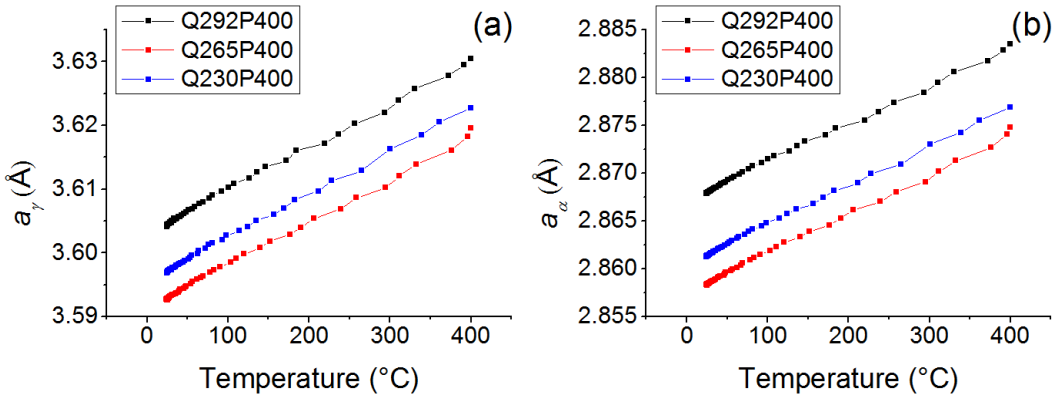

Figure 3.31: (a) Evolution of the lattice parameter of austenite during the final quenching from 400 °C. (b) Evolution of the lattice parameter of ferrite during the final quenching from 400 °C.

The $a_\gamma - T$ relationship is fitted linearly[7] and the results are summarized in Table C.4. Data in Table C.4 is used for calculation of carbon content in Section 3.4.4. All the R^2 values in Table C.4 are equal to 0.998, proving an effective linear relationship between the lattice parameter and temperature in all specimens.

3.5. Kinetics of α_2 formation during the Short Holding, Reheating and Partitioning

As shown by both dilatometry and SXRD, the formation of α_2 must be considered during the Q&P process. In order to study the kinetics of α_2 formation and compare between

[7]The details of the fitting are shown by Figure C.10-C.12 in Appendix A.

specimens quenched to different temperatures, the volume fraction of α_2 is calculated and normalised by the volume fraction of austenite at the end of initial quenching, $f_{\gamma-\mathrm{I}}$:

$$f^n_{\alpha_2} = \frac{f_{\gamma-\mathrm{I}} - f_{\gamma-t}}{f_{\gamma-\mathrm{I}}} \tag{3.16}$$

where $f_{\gamma-t}$ is the volume fraction of austenite at time t. Therefore, $f_{\gamma-\mathrm{I}} - f_{\gamma-t}$ is the fraction of consumed austenite at time t with respect to the end of initial quenching. Since the consumption of austenite only lead to the fomation of α_2 during this stage, this value is the absolute volume fraction of α_2.

Figure 3.32 presents the evolution of $f^n_{\alpha_2}$ with time for the three specimens. It can be seen that the value of $f^n_{\alpha_2}$ for Q230P400 and Q265P400 are very close to each other at any time t, and around 40% α_2 formed for these two specimens. The three specimens share a similar $f^n_{\alpha_2} - t$ pattern before 30% α_2 formed, after which further increase in $f^n_{\alpha_2}$ can be observed in Q292P400. This might be related to the fact that more austenite is present in Q292P400 at the beginning of this stage. In fact, $f^n_{\alpha_2} \approx 30\%$ (30% for Q292, 32% for Q265P400 and 34% for Q240p400) for all three specimen at the end of reheating. This implies that three specimens share almost the same formation kinetics during the reheating process. The slight difference may result from the longer reheating time of Q265P400 and Q230P400 than Q292P400. The difference in the transformation kinetics therefore takes place during the isothermal holding when the austenite in Q292P400 transforms much faster.

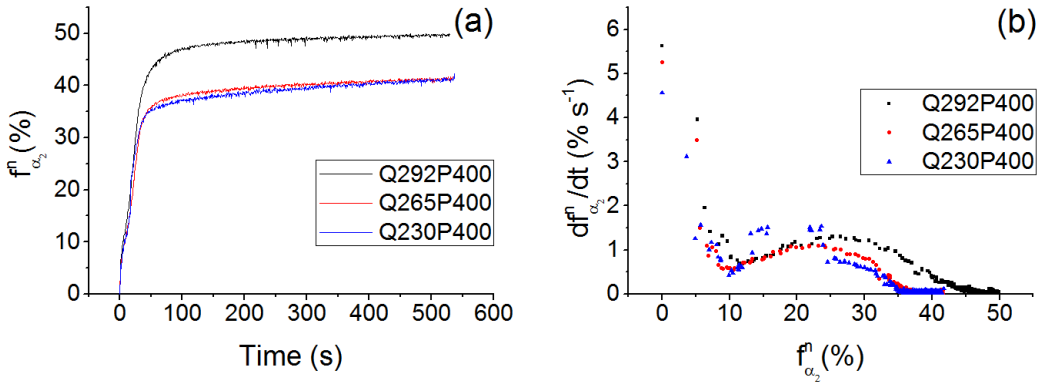

Figure 3.32: (a) The transformed fraction of austenite with time. (b) The rate of transformation as a function of the transformed fraction of austenite. $t = 0$ is selected at the end of the initial quenching for each specimen.

In order to know how the rate of α_2 formation changes with the phase transformation proceeding, the data in Figure 3.32 (a) is firstly smoothed using the adjacent-averaging method [61] to reduce the scattering of the data. Afterwards, the first derivative of $f^n_{\alpha_2}$ is taken with respect to t, as shown in Figure 3.32 (b). For all three specimens, the fastest rate of α_2 formation occurs at the beginning of reheating, and with the transformation proceeding, the rate of transformation will decrease and then increase, and this turning point corresponds to $f^n_{\alpha_2} = 10\%$ for each specimen. The corresponding temperature is higher for specimens with a higher volume fraction of austenite at the beginning of this stage: 247 °C, 289 °C and 302 °C for Q230P400, Q265P400 and Q292P400 respectively. For Q230P400 and Q265P400, the rate of α_2 formation increases until 20% of transformation is reached, followed by a decrease in rate. For Q300P400, the rate continues to increase until 25% of transformation is reached, and then decreases until the partitioning is finished. While the

rate of Q292P400 decreases, it is still higher than that of Q265P400 and Q230P400. This difference is enlarged after $f^n_{\alpha_2} = 30\%$, where higher $f^n_{\alpha_2}$ is expected with Q292P400.

4

Discussions

4.1. Carbon Enrichment in Austenite and Associated Phase Transformations

Both the dilatometry and SXRD experiments show that austenite can be enriched with carbon through the reheating and partitioning steps, with more carbon enrichment in austenite during reheating than partitioning step. The carbon enrichment is accompanied by the consumption of austenite and the formation of a BCC phase or phases (α_2). α_2 formed immediately after the initial quenching stops. Since this process starts from below M_s to above M_s, it is difficult to determine whether α_2 consists of bainite, martensite, or both. Above M_s, researchers [62–68] agree that the isothermal products formed from the decomposition of austenite consists of bainitic ferrite with or without carbides and retained austenite. The bainitic transformation will also be accelerated by the primary martensite formed before the isothermal treatment, because the martensite-austenite interfaces act as additional potential nucleation sites [20]. Since partitioning is performed at 400 °C, which is within the bainitic temperature range, α_2 formed during the partitioning step should be bainite (α_b). However, controversy exists over the isothermal products formed below M_s, which can be purely bainitic [27, 65, 69], martensitic [70], or a phase product neither purely martensitic nor bainitic [68, 71, 72]. The kinetics analysis in Section 3.5 suggests that two phase products might form during reheating, since the rate of transformation firstly decreased and then increase during reheating. One explanation for this is that as the initial quenching stops, the martensite continues to grow at a fast rate, however, with the carbon partitioning into austenite, M_s is lowered while the steel is reheating. The lowering M_s and the rising temperature decreases the undercooling until a temperature T_b is reached where the growth of martensite stops (corresponding to the first turning point in Figure 3.5) and the bainite nucleation begins. According to Santofimia *et al.* [73, 74], with the presence of some fraction of primary martensite $f_{\alpha'_1}$, the rate of isothermal bainitic transformation df_{α_b}/dt is related to the volume fraction of bainite f_{α_b} as:

$$\frac{df_{\alpha_b}}{dt} = (1 - f_{\alpha_b} - f_{\alpha'_1})(1 + \lambda_{\alpha_b} f_{\alpha_b} + \lambda_{\alpha'_1} f_{\alpha'_1})\kappa \tag{4.1}$$

where λ_{α_b} and $\lambda_{\alpha'_1}$ is the autocatalytic constant due to the presence of bainite and primary martensite, respectively. κ is a rate constant which is related to temperature. At a

given temperature and certain f_{α_b} range, df_{α_b}/dt will have a parabolic relationship with f_{α_b}, i.e. df_{α_b}/dt increases with f_{α_b} to a maximal point and then decreases. This trend is also observed in Figure 3.5) despite the fact that part of the curve does not reside in the isothermal region. Besides, it is very difficult to tell whether martensite growths ceases at T_b and bainite nucleation starts at T_b. Therefore, the analysis above is only qualitative and simplified. For more precise phases determination and quantification, characterization techniques such as TEM, EBSD and IF spectrum can be used [68, 71, 72].

4.2. CCE and the End of Carbon Partitioning

The CCE model cannot be used for the prediction of the end of partitioning for the studied steel due to the following reasons. Firstly, after the initial quenching stops, the primary martensite continues to grow, which contradicts the condition 2 of CCE assuming a stationary martensite/austenite interface. Secondly, during the reheating and partitioning, the carbon enrichment in austenite is accompanied by bainite formation, which is assumed to be precluded in CCE model. The model in literature [73, 74] might provide a method to simulate the coupling of carbon partitioning process and bainite formation, however, this model does not take into account the carbon partitioning and bainite formation during reheating; both of the processes are assumed to occur only during the partitioning step. However, as the results show that the rate of transformation is fastest at the start of reheating, and as many researchers [27, 65, 68, 69, 69–72] have observed the immediate phase transformation after the initial quenching, the reheating as well as the short holding before the partitioning should not be ignored.

As Figure 3.28 shows, C_γ of Q230P400 firstly reached a plateau at around $t = 150$ s, and stablised for about 50 s, followed by a slight decrease in C_γ. C_γ in Q265P400 increased until $t = 300$ s and kept constant afterwards for 200 s. C_γ of Q292P400 continued to increase until the end of partitioning step, showing a growing trend. To summarize, the specimen with the least austenite at the end of initial quenching reaches the stabilisation of carbon content first, and more time is needed for specimen with higher volume fraction of austenite at QT. When the carbon content is stabilised in austenite, still a slight decrease in f_γ can be observed, showing that carbon enrichment in austenite can be completed before the whole system reaches equilibrium. Therefore, the partitioning time should not be too long so that more austenite can be retained at room temperature.

4.3. The Influence of Process Parameters on Final Microstructure

QT determines the amount of α_1', which can be predicted using K-M equation or by applying the lever rule to the dilatometry curves. Afterwards, if no phase transformation occurs and the carbon in the martensite can partition completely into the austenite, RA fraction will change with the QT as shown by the calculated line in Figure 4.1. However, because austenite will be consumed during the short holding, reheating and partitioning, the optimal QT determined by experiments is higher than the calculated one. The changes of experimental RA fraction with QT is also less sharp compared to the calculated results, implying that QT can be selected from a wider range to obtain desired RA fraction. When PT is chosen properly (400 °C in this study), the carbides precipitation is limited, and within the chosen QT range (230 – 300 °C), RA fraction increases with increasing QT.

The partitioning time t_p influences the carbon enrichment in austenite. Carbon enrichment in austenite can be increased with increasing t_p. If partitioning time is chosen properly, austenite can be enriched to a level where no fresh martensite will form during the final quenching. A further increase in t_p results in more carbon in austenite until the carbon level is stabilised, accompanied by a slight decrease in austenite fraction. This will be reflected as an increasing RA fraction with t_p followed by slight decrease, which has been observed in the second dilatometry tests: RA fraction increases until $t_p = 300$ s, followed by a slight decrease at $t_p = 500$ s. After the stabilisation of carbon level in austenite, any further increase in t_p would lead to more decrease in the austenite fraction and even loss of carbon in austenite, resulting in less RA with lower carbon level.

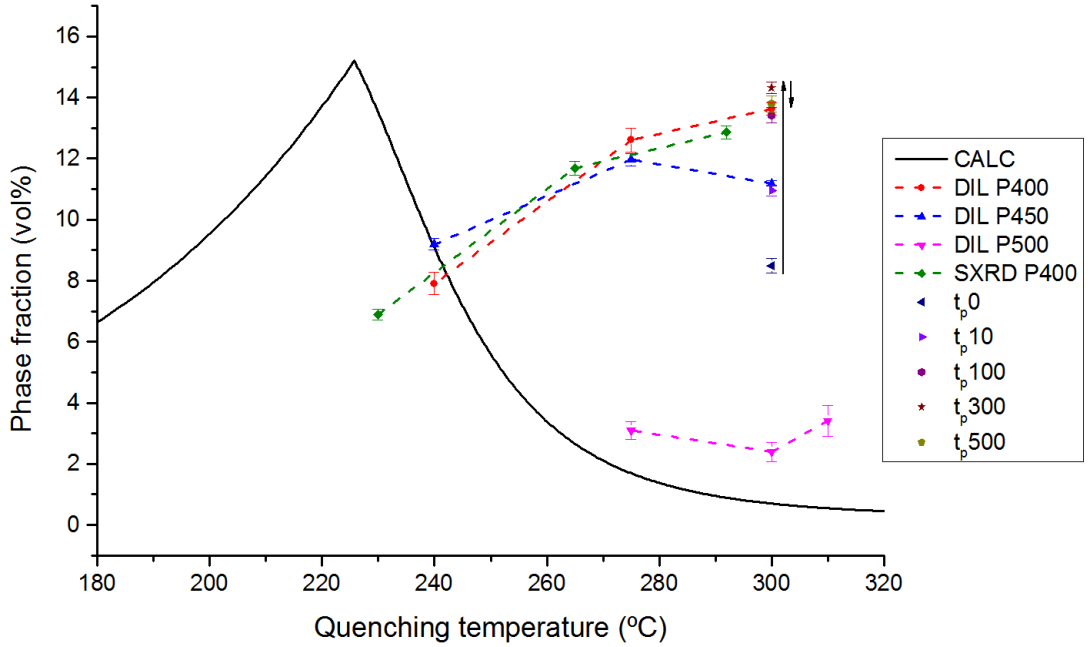

Figure 4.1: A summary of the volume fraction of RA obtained with different QTs. The results of obtained by the dilatometry tests are labelled by DIL. For the preliminary heat treatments where the partitioning time all equals to 500 s, the partitioning temperature is added after DIL. For the secondary dilatometry tests where the partitioning is performed at 400 °C, the partitioning time t_p is added after DIL. The synchrotron XRD experiments are labelled by SXRD P400. The two arrows highlight RA fraction behaviour with increasing partitioning time for QT = 300 °C and PT = 400 °C. The experimental results are compared with the calculated results (CALC) using the methodology in literature [11].

Another important parameter is the heating rate during reheating. Lower heating rate would mean longer interval between the initial quenching and partitioning step, and as shown by our results, fast phase transformation and carbon enrichment can occur during this stage. However, since all the heating rate is selected to be 5 °C/s in this work, it is not known how the heating rate would influence the rate of transformation during this stage.

4.4. Comparison to Other Processes

In this work, the microstructure consisting of bainite, martensite and retained austenite is obtained through the Q&P process. This microstructure mixture is conventionally obtained through the austempering process, an example of which is shown by the black

line in Figure 4.2, where the fully austenitised steel is firstly quenched to a temperature within the bainitic temperature range, followed by an isothermal holding at this temperature and then a final quenching. Compared to the austempering process, the kinetics of bainite formation during the Q&P process is much faster due to the accelerating effect of primary martensite on the bainitic transformation [73, 74]. For a direct comparison, the strain vs. time diagram of a steel of the same composition as in Table 2.1 austempered at 400 °C is shown in Figure 4.2. There is a incubation time of about 30 s for the bainite formation, and then it takes more than 1000 s to complete the phase transformation, which is marked by the plateau in the figure. The bainitic reaction in Q&P process with a PT=400 ° takes 200 – 500 s to approach the completion, which is much less than the time required for the austempering process. Apart from the time that can be saved during heat treatment, the RA fraction can be adjusted in a wider range without formation of fresh martensite, resulting in a microstructure consisting of tempered martensite, bainite and retained austenite. In this study, RA fraction can be adjusted from 6.9 vol.% to 13.6 vol.% without forming fresh martensite. By contrast, in the case of austempering, fresh martensite would even form during the final quench with the completion of bainite transformation, depending on the chemical composition of the steel.

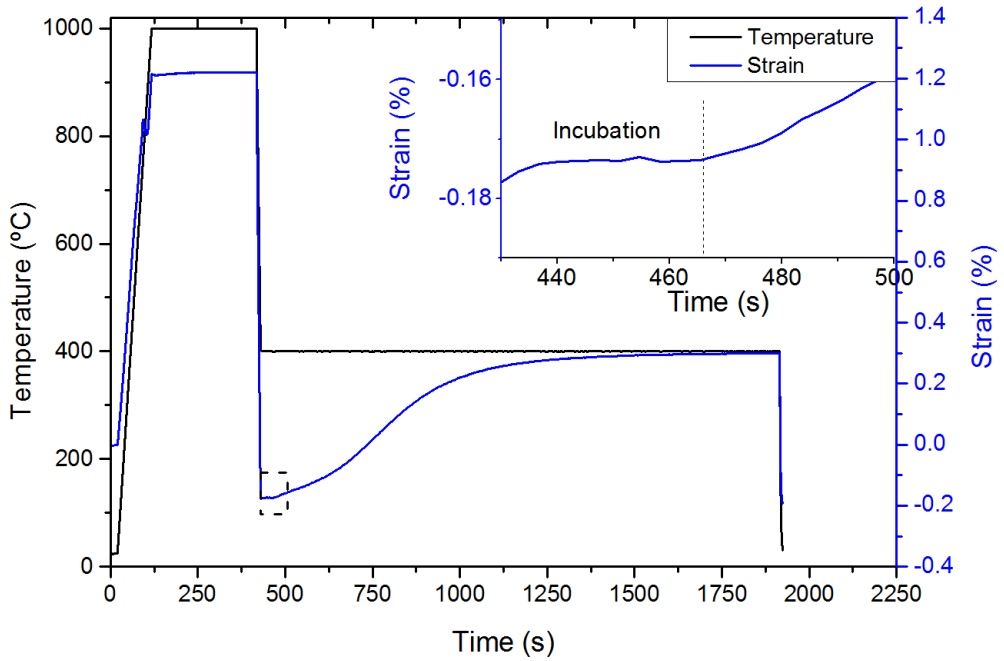

Figure 4.2: An example of the austempering process and the strain vs. time diagram of the studied specimen processed with austempering. The inset shows an enlarged image of the dashed-square area.

The bainite/martensite multi-phase steels obtained through Q&P also show improved mechanical properties. Gao *et al.* [75] obtained a low-carbon steel that exhibits a fatigue limit of 770 MPa in the very high cycle fatigue regime and a tensile strength of 1410 MPa by a Q&P-tempering process that obtained bainite during the initial quenching. Luo *et al.* [76] obtained the multi-phase steel that has a tensile strength of 1923 MPa and total elongation of 18.3%. Huang *et al.* [77] showed a significantly improved impact toughness from 84 J/cm^2 for austempering to 104 J/cm^2 for the Q&P heat treatment. The reported improvement upon fatigue behaviour, strengths, ductility and toughness would be beneficial for

industrial applications. The obtained multi-phase steel in this study can be further characterized mechanically in order to study the effect of different microstructures (e.g. different RA volume fraction) on the mechanical behaviour.

5

Conclusions and Recommendations

In this project, the phase transformations in a steel of a composition Fe–0.2C–3Mn–2Si (wt.%) during the Q&P were studied. Three sets of experiments were performed: the preliminary dilatometry tests to select appropriate processing parameters for Q&P thermal cycles, secondary dilatometry tests to study the effect of partitioning time on the final microstructure, in-situ synchrotron XRD experiments to study the microstructural evolution during the Q&P process. The following conclusions are drawn from the results and discussions:

5.1. Conclusions

- Carbon enrichment in austenite can be achieved through reheating and partitioning during Q&P, with more carbon partitioning occured during reheating. Carbon enrichment is also accompanied by 40%-50% transformation of previously retained austenite and the rate of transformation is highest at the beginning of the reheating process. During reheating, the consumption of austenite might be related to the formation of martensite and then bainite. Bainite formation is expected during partitioning.

- The CCE model cannot be used for the prediction of end of partitioning for the studied steel. A better model needs to couple the process of carbon partitioning with bainite formation. The microstructural changes during reheating must be considered too.

- When the carbon level in austenite is stabilised, there is still a slight decrease in austenite fraction, showing that carbon enrichment in austenite can be completed before the whole system reaches equilibrium.

- Microstructure consisting of tempered martensite with carbides, bainite and RA is obtained through the Q&P process, with tempered martensite mainly as the BCC phase. The required time to obtain the multi-phase structure is much less than that of austempering. The RA fraction can be adjusted from 6.9 vol.% to 13.6 vol.% without forming fresh martensite. Up to 14.3 vol.% of retained austenite can be obtained, which is very close to the predicted maximum, 15.2 vol.%., with 4.5 vol.% of fresh

martensite in the microstructure. Small amount of Widmanstätten ferrite was also detected in the case of SXRD experiments, but not for dilatometry tests.

5.2. Recommendations

There are still some questions that remain unresolved in this study and the following works are recommended:

- Since the quantification of carbon content in the martensite or bainite is not achieved in this study, APT can be performed in order to study the local carbon content of martensite or bainite.
- For more precise determination and quantification of the phase product formed below M_s, characterization techniques such as TEM, EBSD and IF spectrum can be used.
- Since heating rate can influence the time of reheating and thus the kinetics of phase transformation during this stage, a set of Q&P processes with different reheating rate can be performed either with dilatometry or SXRD.
- Mechanical characterization such as tensile test can be performed with the obtained multi-phase steel in this study to investigate the relationship between mechanical properties and microstructures.
- The as-received steel shows banded morphology in the microstructure. In order to investigate the influence of the banded morphology, similar Q&P process can be applied to steels with the same composition but homogenised.

Bibliography

[1] N. Fonstein, *Advanced High Strength Sheet Steels: Physical Metallurgy, Design, Processing, and Properties* (Springer, 2015).

[2] S. Hayami and T. Furukawa, *A family of high-strength cold-rolled steels,* in *Union Carbide Corporation* (1975) p. 311.

[3] J. Hall, *Evolution of advanced high strength steels in automotive applications,* Presentation at Joint Policy Council, Auto/Steel Partnership **18** (2011).

[4] R. Kuziak, R. Kawalla, and S. Waengler, *Advanced high strength steels for automotive industry,* Archives of Civil and Mechanical Engineering **8**, 103 (2008).

[5] M. Takahashi, *Development of high strength steels for automobiles,* Shinnittetsu Giho , 2 (2003).

[6] D. K. Matlock and J. G. Speer, *Third generation of* AHSS*: microstructure design concepts,* in *Microstructure and texture in steels* (Springer, 2009) pp. 185–205.

[7] D. K. Matlock and J. G. Speer, *Design considerations for the next generation of advanced high strength sheet steels,* in *Proceedings of 3rd International Conference on Structural Steels* (2006) pp. 774–781.

[8] J. G. Speer, D. K. Matlock, B. C. de Cooman, and J. G. Schroth, *Carbon partitioning into austenite after martensite transformation,* Acta Materialia **51**, 2611 (2003).

[9] D. K. Matlock, V. E. Bräutigam, and J. G. Speer, *Application of the quenching and partitioning (Q&P) process to a medium-carbon, high-Si microalloyed bar steel,* in *Materials Science Forum*, Vol. 426 (Trans Tech Publ, 2003) pp. 1089–1094.

[10] J. G. Speer, F. C. R. Assunção, D. K. Matlock, and D. V. Edmonds, *The "quenching and partitioning" process: background and recent progress,* Materials Research **8**, 417 (2005).

[11] J. G. Speer, D. V. Edmonds, F. C. Rizzo, and D. K. Matlock, *Partitioning of carbon from supersaturated plates of ferrite, with application to steel processing and fundamentals of the bainite transformation,* Current Opinion in Solid State and Materials Science **8**, 219 (2004).

[12] J. G. Speer, D. K. Matlock, B. C. de Cooman, and J. G. Schroth, *Comments on "On the definitions of paraequilibrium and orthoequilibrium",* Scripta Materialia **52**, 83 (2005).

[13] M. Hillert and J. Ågren, *On the definitions of paraequilibrium and orthoequilibrium,* Scripta Materialia **50**, 697 (2004).

[14] M. Hillert and J. Ågren, *Reply to comments on "on the definition of paraequilibrium and orthoequilibrium",* Scripta Materialia **52**, 87 (2005).

[15] N. Zhong, X. Wang, Y. Rong, and L. Wang, *Interface migration between martensite and austenite during quenching and partitioning (*Q&P*) process,* Journal of Materials Science and Technology **22**, 751 (2006).

[16] J. G. Speer, R. E. Hackenberg, B. C. de Cooman, and D. K. Matlock, *Influence of interface migration during annealing of martensite/austenite mixtures,* Philosophical Magazine Letters **87**, 379 (2007).

[17] M. J. Santofimia, L. Zhao, and J. Sietsma, *Model for the interaction between interface migration and carbon diffusion during annealing of martensite–austenite microstructures in steels,* Scripta Materialia **59**, 159 (2008).

[18] M. J. Santofimia, J. G. Speer, A. J. Clarke, L. Zhao, and J. Sietsma, *Influence of interface mobility on the evolution of austenite–martensite grain assemblies during annealing,* Acta Materialia **57**, 4548 (2009).

[19] D. de Knijf, M. J. Santofimia, H. Shi, V. Bliznuk, C. Föjer, R. Petrov, and W. Xu, *In situ austenite–martensite interface mobility study during annealing,* Acta Materialia **90**, 161 (2015).

[20] H. Kawata, K. Hayashi, N. Sugiura, N. Yoshinaga, and M. Takahashi, *Effect of martensite in initial structure on bainite transformation,* in *Materials Science Forum*, Vol. 638 (Trans Tech Publ, 2010) pp. 3307–3312.

[21] K. Seto and H. Matsuda, *Application of nanoengineering to research and development and production of high strength steel sheets,* Materials Science and Technology **29**, 1158 (2013).

[22] J. Sun and H. Yu, *Microstructure development and mechanical properties of quenching and partitioning (Q&P) steel and an incorporation of hot-dipping galvanization during q&p process,* Materials Science and Engineering: A **586**, 100 (2013).

[23] H. K. D. H. Bhadeshia and R. W. K. Honeycombe, *Steels: microstructure and properties* (Butterworth-Heinemann, 2011).

[24] Y. Toji, G. Miyamoto, and D. Raabe, *Carbon partitioning during quenching and partitioning heat treatment accompanied by carbide precipitation,* Acta Materialia **86**, 137 (2015).

[25] J. G. Speer, E. de Moor, and A. J. Clarke, *Critical assessment 7: quenching and partitioning,* Materials Science and Technology **31**, 3 (2015).

[26] S.-J. Kim, C. G. Lee, I. Choi, and S. Lee, *Effects of heat treatment and alloying elements on the microstructures and mechanical properties of 0.15 wt pct C transformation-induced plasticity-aided cold-rolled steel sheets,* Metallurgical and Materials Transactions A **32**, 505 (2001).

[27] A. Navarro-López, J. Sietsma, and M. J. Santofimia, *Effect of prior athermal martensite on the isothermal transformation kinetics below M_s in a low-C high-Si steel,* Metallurgical and Materials Transactions A **47**, 1028 (2016).

[28] B. C. de Cooman, *Structure–properties relationship in TRIP steels containing carbide-free bainite,* Current Opinion in Solid State and Materials Science **8**, 285 (2004).

[29] C. García de Andrés, F. G. Caballero, C. Capdevila, and L. F. Álvarez, *Application of dilatometric analysis to the study of solid–solid phase transformations in steels,* Materials Characterization **48**, 101 (2002).

[30] G. L. Fisher and R. H. Geils, *A method for obtaining quantitative dilatometric data from alloys undergoing a phase transformation,* Metallography **3**, 229 (1970).

[31] T. A. Kop, *A dilatometric study of the austenite/ferrite interface mobility* (Delft University of Technology, 2000).

[32] H. S. Yang and H. K. D. H. Bhadeshia, *Uncertainties in dilatometric determination of martensite start temperature,* Materials Science and Technology **23**, 556 (2007).

[33] B. D. Cullity, *Elements of x-ray diffraction,* (1956).

[34] P. Suwanpinij, *The synchrotron radiation for steel research,* Advances in Materials Science and Engineering **2016** (2016).

[35] J. A. Bearden, *X-ray wavelengths,* Reviews of Modern Physics **39**, 78 (1967).

[36] H. Rietveld, *A profile refinement method for nuclear and magnetic structures,* Journal of applied Crystallography **2**, 65 (1969).

[37] L. Lutterotti, S. Matthies, H.-R. Wenk, A. S. Schultz, and J. W. Richardson Jr, *Combined texture and structure analysis of deformed limestone from time-of-flight neutron diffraction spectra,* Journal of Applied Physics **81**, 594 (1997).

[38] D. Carmele, T. Rieger, K. Herrmann, S. Meyer, T. Lippmann, A. Stark, W. Bleck, and U. Klemradt, *Very hard synchrotron X-ray radiation as an advanced characterization method applied to advanced high-strength steels,* in *Advanced Materials Research*, Vol. 409 (Trans Tech Publications, 2012) pp. 660–665.

[39] B. B. He, U. Preckwinkel, and K. L. Smith, *Fundamentals of two-dimensional X-ray diffraction (XRD^2),* Advances in X-ray Analysis **43**, 273 (2000).

[40] A. Hammersley, *Fit2d v9. 129 reference manual v3. 1,* Inter Rep ESRF98HA01, ESRF, Grenoble (1998).

[41] A. P. Hammersley, S. O. Svensson, M. Hanfland, A. N. Fitch, and D. Hausermann, *Two-dimensional detector software: from real detector to idealised image or two-theta scan,* International Journal of High Pressure Research **14**, 235 (1996).

[42] A. P. Hammersley, *Fit2d: an introduction and overview,* European Synchrotron Radiation Facility Internal Report ESRF97HA02T **68** (1997).

[43] W. David, *Powder diffraction: least-squares and beyond,* Journal of Research of the National Institute of Standards and Technology **109**, 107 (2004).

[44] M. I. A. Lourakis, *A brief description of the Levenberg-Marquardt algorithm implemented by levmar,* Foundation of Research and Technology **4**, 1 (2005).

[45] H. Gavin, *The Levenberg-Marquardt method for nonlinear least squares curve-fitting problems,* (2011).

[46] B. H. Toby, *R factors in* R*ietveld analysis: How good is good enough?* Powder diffraction **21**, 67 (2006).

[47] L. Lutterotti, *Introduction to diffraction and the Rietveld method,* http://www.ccp14.ac.uk/ccp/web-mirrors/lutterotti/ luttero/laboratoriomateriali/Rietveld.pdf, accessed: 2016-07-30.

[48] K. W. Andrews, *Empirical formulae for the calculation of some transformation temperatures,* Journal of the Iron and Steel Institute **207**, 721 (1965).

[49] A. A. Gorni, *Steel forming and heat treating handbook,* Sao Vicente (2011).

[50] S. M. C. van Bohemen and J. Sietsma, *Martensite formation in partially and fully austenitic plain carbon steels,* Metallurgical and Materials Transactions A **40**, 1059 (2009).

[51] Y. K. Lee, *Empirical formula of isothermal bainite start temperature of steels,* Journal of Materials Science Letters **21**, 1253 (2002).

[52] H. K. D. H. Bhadeshia, *Bulk nanocrystalline steel,* Ironmaking & Steelmaking (2013).

[53] D. P. Koistinen and R. E. Marburger, *A general equation prescribing the extent of the austenite-martensite transformation in pure iron-carbon alloys and plain carbon steels,* Acta Metallurgica **7**, 59 (1959).

[54] A. J. Clarke, J. G. Speer, D. K. Matlock, F. C. Rizzo, D. V. Edmonds, and M. J. Santofimia, *Influence of carbon partitioning kinetics on final austenite fraction during quenching and partitioning,* Scripta Materialia **61**, 149 (2009).

[55] N. H. van Dijk, A. M. Butt, L. Zhao, J. Sietsma, S. E. Offerman, J. P. Wright, and S. van der Zwaag, *Thermal stability of retained austenite in trip steels studied by synchrotron x-ray diffraction during cooling,* Acta Materialia **53**, 5439 (2005).

[56] B. He, U. Preckwinkel, and K. L. Smith, *Comparison between conventional and two-dimensional XRD,* Adv. X-Ray Anal **46**, 37 (2003).

[57] N. Oku, K. Asakura, J. Inoue, and T. Koseki, *In-situ observation of ferrite plate formation in low carbon steel during continuous cooling process,* Journal of the Iron and Steel Institute of Japan **94**, B33 (2008).

[58] H. K. D. H. Bhadeshia, *Widmanstätten ferrite,* http://www.msm.cam.ac.uk/phase-trans/2000/C9/lecture7.pdf, accessed: 2016-07-30.

[59] L. Cheng, A. Böttger, T. H. de Keijser, and E. J. Mittemeijer, *Lattice parameters of iron-carbon and iron-nitrogen martensites and austenites,* Scripta metallurgica et materialia **24**, 509 (1990).

[60] R. E. Walpole, R. H. Myers, and S. L. Myers, *Probability and statistics for engineers and scientists*, 9th ed., Vol. 5 (Prentice Hall, 2012).

[61] Origin, *The adjacent-averaging method,* http://www.originlab.com/doc/Origin-Help/Smooth-Algorithm, accessed: 2016-07-30.

[62] K.-i. Sugimoto, T. Iida, J. Sakaguchi, and T. Kashima, *Retained austenite characteristics and tensile properties in a TRIP type bainitic sheet steel.* ISIJ international **40**, 902 (2000).

[63] K.-i. Sugimoto, M. Murata, and S.-M. Song, *Formability of Al-Nb bearing ultra high-strength TRIP-aided sheet steels with bainitic ferrite and/or martensite matrix,* ISIJ international **50**, 162 (2010).

[64] Y. H. Jiang, R. F. Zhou, D. Lu, and Z. H. Li, *Microstructures and properties of a bainite and martensite dual-phase cast steel fabricated by combination of alloying and controlled cooling heat treatment,* in *Materials Science Forum*, Vol. 475 (Trans Tech Publ, 2005) pp. 93–96.

[65] S. Van Bohemen, M. Santofimia, and J. Sietsma, *Experimental evidence for bainite formation below m s in fe–0.66 c,* Scripta Materialia **58**, 488 (2008).

[66] J.-C. Hell, M. Dehmas, S. Allain, J. M. Prado, A. Hazotte, and J.-P. Chateau, *Microstructure-properties relationships in carbide-free bainitic steels,* ISIJ international **51**, 1724 (2011).

[67] I. Yakubtsov and G. Purdy, *Analyses of transformation kinetics of carbide-free bainite above and below the athermal martensite-start temperature,* Metallurgical and Materials Transactions A **43**, 437 (2012).

[68] D. H. Kim, J. G. Speer, and B. C. De Cooman, *The isothermal transformation of low-alloy low-C CMnSi steels below M_s,* in *Materials Science Forum*, Vol. 654 (Trans Tech Publ, 2010) pp. 98–101.

[69] E. P. da Silva, D. de Knijf, W. Xu, C. Föjer, Y. Houbaert, J. Sietsma, and R. Petrov, *Isothermal transformations in advanced high strength steels below martensite start temperature,* Materials Science and Technology **31**, 808 (2015).

[70] M. Oka and H. Okamoto, *Swing back in kinetics near M_s in hypereutectoid steels,* Metallurgical Transactions A **19**, 447 (1988).

[71] D. Kim, J. G. Speer, and B. De Cooman, *Isothermal transformation of a CMnSi steel below the M_s temperature,* Metallurgical and Materials Transactions A **42**, 1575 (2011).

[72] D. Kim, S.-J. Lee, and B. C. De Cooman, *Microstructure of low C steel isothermally transformed in the M_s to M_f temperature range,* Metallurgical and Materials Transactions A **43**, 4967 (2012).

[73] M. J. Santofimia Navarro, D. Hanlon, J. Sietsma, and S. van Bohemen, *Perspectives in high strength steels: interactions between non-equilibrium phases,* in *Proceedings of the 2013 International Symposium on New Developments in Advanced High-Strength Sheet Steels.*, edited by K. D. Hickey and R. E. Ashburn (Association for Iron & Steel Technology, 2013) pp. 331–339.

[74] M. Santofimia, S. van Bohemen, and J. Sietsma, *Combining bainite and martensite in steel microstructures for light weight applications,* Journal of the Southern African Institute of Mining and Metallurgy **113**, 143 (2013).

[75] G. Gao, B. Zhang, C. Cheng, P. Zhao, H. Zhang, and B. Bai, *Very high cycle fatigue behaviors of bainite/martensite multiphase steel treated by quenching-partitioning-tempering process,* International Journal of Fatigue **92, Part 1**, 203 (2016).

[76] P. Luo, G. Gao, H. Zhang, Z. Tan, R. Misra, and B. Bai, *On structure-property relationship in nanostructured bainitic steel subjected to the quenching and partitioning process,* Materials Science and Engineering: A **661**, 1 (2016).

[77] X. Huang, W. Liu, Y. Huang, H. Chen, and W. Huang, *Effect of a quenching–long partitioning treatment on the microstructure and mechanical properties of a 0.2C bainitic steel,* Journal of Materials Processing Technology **222**, 181 (2015).

[78] R. W. G. Wyckoff, *Fluorite structure,* Crystal Structures **1**, 239 (1963).

A

Preliminary Heat Treatment

A.1. M_s Determination

Table A.1: M_s determined by offset method.

Specimen	M_s (°C)
Q240P400	337.4
Q275P400	355.9
Q300P400	331.3
Q240P450	340.7
Q275P450	346.8
Q300P450	340.4
Q275P500	353.6
Q300P500	329.3
Q310P500	343.3
Full quench	339.0

A.2. Microstructure

Figure A.1 presents SEM micrographs of the fully quenched specimen in the preliminary dilatometry tests. Figure A.2 presents the SEM micrographs of the specimens quenched to 240 °C, 275 °C and 300 °C but all partitioned at 450 °C. Fresh martensites can be clearly distinguished in the specimen Q240P450, and small islands of martensite-austenite can be observed in the specimen Q300P450. The microstructures of the P500 series are shown in Figure A.3. Ferrite can be observed in the specimen Q300P500; no carbides can be resolved in the 5000 × magnification.

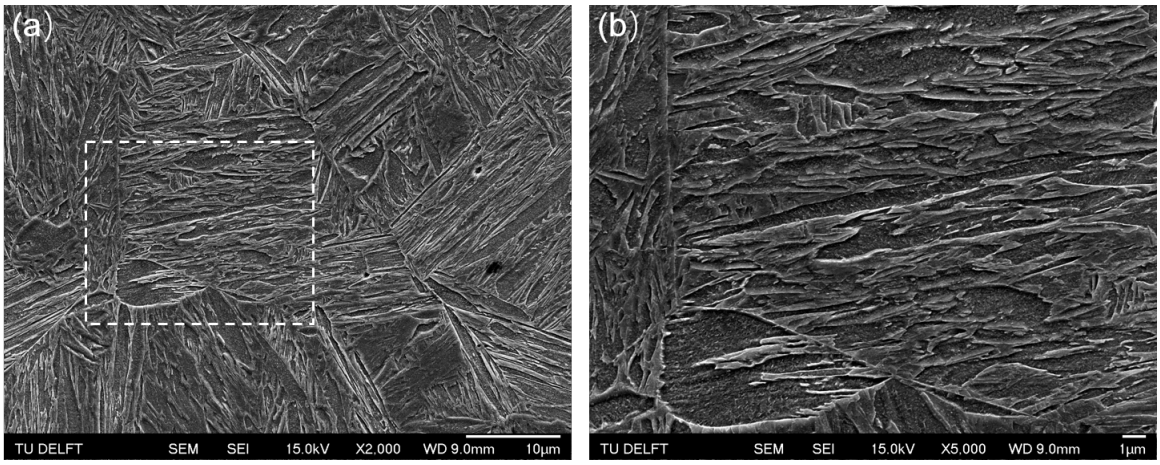

Figure A.1: (a) Microstructure of the full quenched sample. (b) The enlarged image of the squared area in Figure (a).

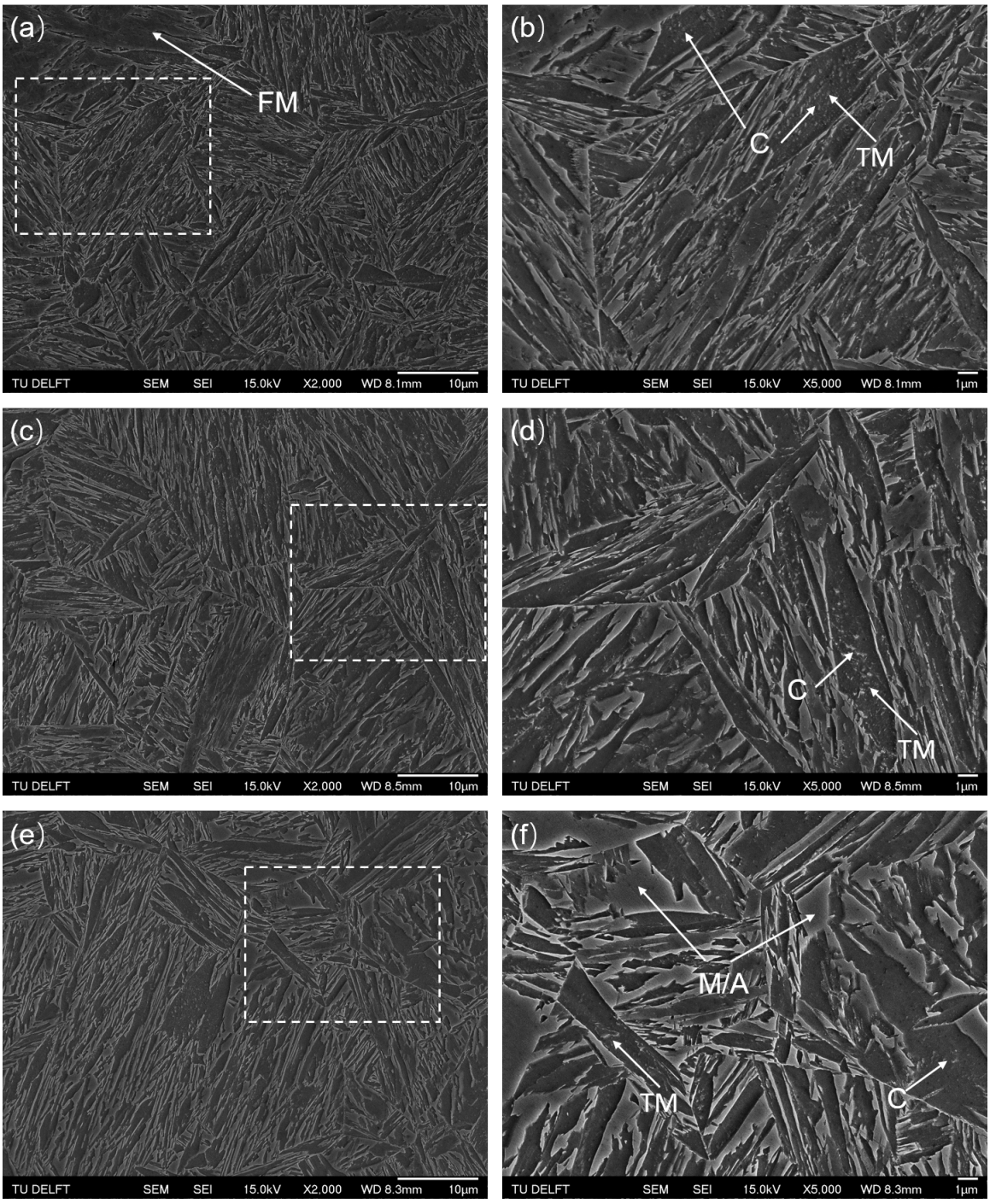

Figure A.2: (a),(c),(e): Microstructures of Q&P processed specimen quenched to 240 °C, 275 °C and 300 °C respectively. All specimens are partitioned at 450 °C. (b), (d), (f): The enlarged images of the squared area in (a), (c) and (e) respectively. Carbides are labelled by C, tempered martensite by TM, fresh martensite by FM, martensite-austenite islands by M/A.

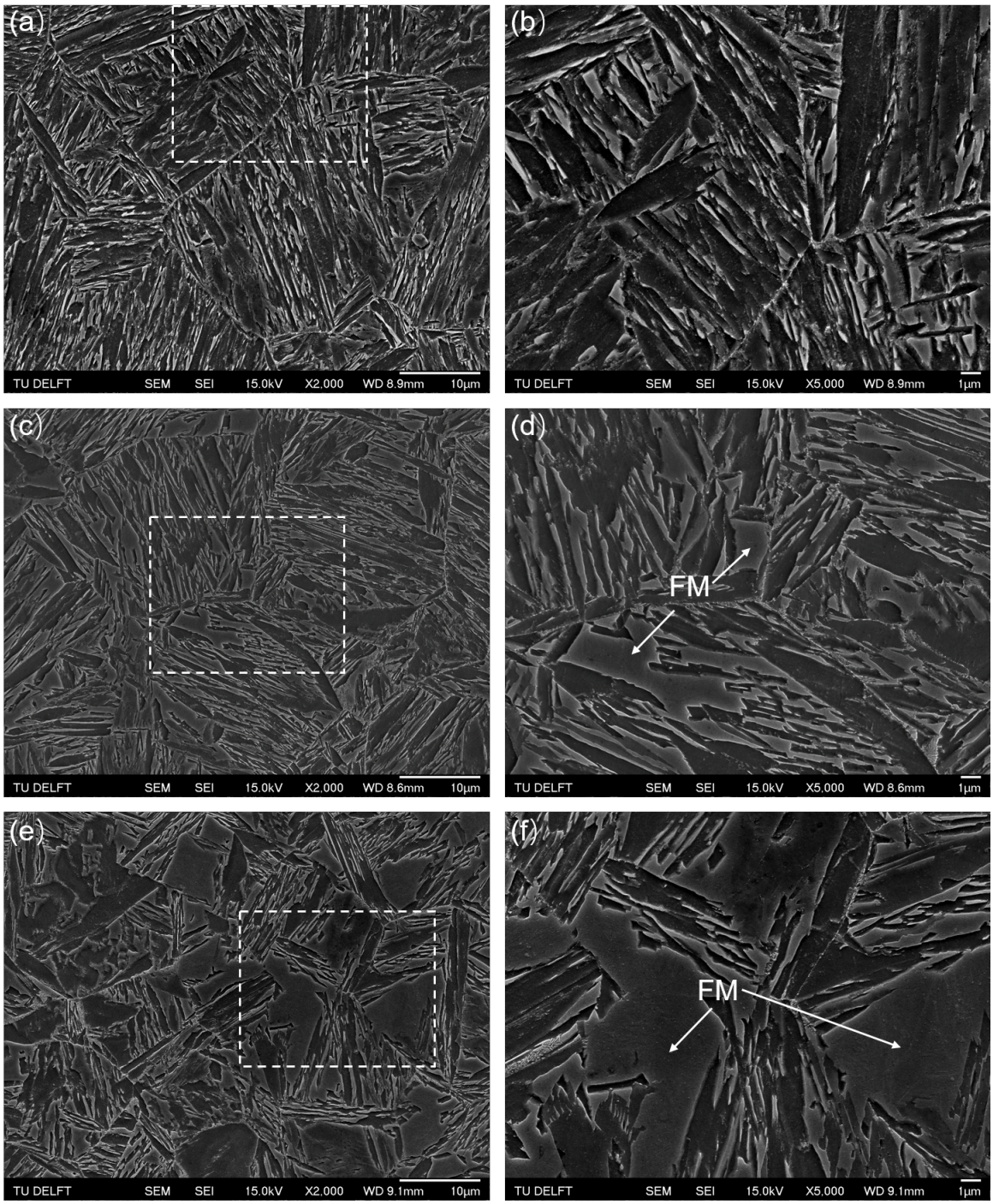

Figure A.3: (a),(c),(e): Microstructures of Q&P processed specimen quenched to 275 °C, 300 °C and 310 °C respectively. All specimens are partitioned at 500 °C. (b), (d), (f): The enlarged images of the squared area in (a), (c) and (e) respectively. Fresh martensite by FM.

B

XRD Diffractograms and Profile Fitting

B.1. XRD Diffractograms for the Preliminary Dilatometry Tests

Figure B.1 presents the diffractograms measured for the specimens in the preliminary dilatometry tests. The approximate peak positions are indicated by the blue lines (α peaks) or red lines (γ peaks).

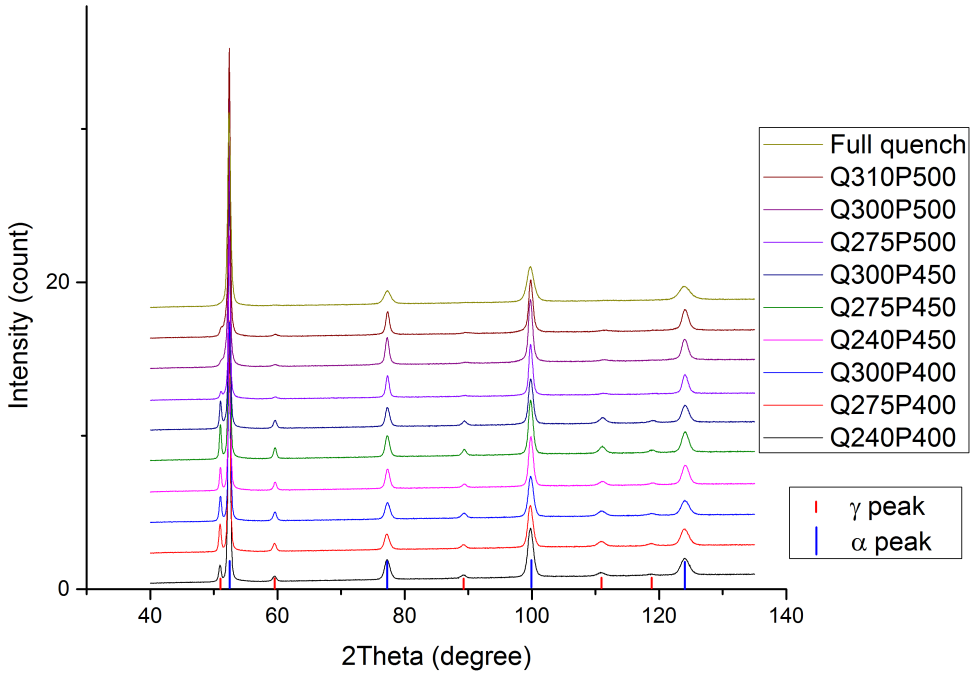

Figure B.1: XRD diffractograms of the first set of dilatometry specimens

B.2. In-situ XRD Experiments

The calibrated parameters are shown in Table B.1

Table B.1: Calibrated parameters for the in-situ XRD experiments.

Specimen	Refined beam centre (mm,mm)	Refined sample to detector distance (mm)	Refined tilt plane rotation angle (°)	Refined tilt angle (°)
Full quench	(50.653, 51.093)	301.709	17	0.058
Q230P400	(50.568, 51.113)	300.191	37.866	0.057
Q265P400	(50.684, 50.921)	300.447	38.807	-0.174
Q292P400	(50.652, 50.921)	300.883	22.213	0.091

The calibrated lattice parameters obtained for the calibrant CeO_2 (a_{CeO_2}) and the literature value [78] are shown in Table B.2. Compared to the literature value, a_{CeO_2} of Q265P400 deviates the most, and is smaller than the literature value. By checking the diffractogram of CeO_2 (Figure B.2, it is found that the apart from the CeO_2 peaks, there are other peaks that cannot be fitted, which implies that there is impurity in the CeO_2 powder. This deviation would result in a 0.26% error in the determination of lattice parameter of austenite (a_γ) since a_γ is calculated based on the calibration of CeO_2. This error in a_γ would lead to an error of 0.2wt.% in the determination of carbon content.

Table B.2: Calibrated a_{CeO_2} of the four specimens and a_{CeO_2} from literature.

Specimen	Full quench	Q230P400	Q265P400	Q292P400	literature
a_{CeO_2} (Å)	5.4135±0.0004	5.4146±0.0004	5.397±0.001	5.4147±0.0004	5.411
deviation (Å)	0.0025	0.0036	-0.014	0.0037	0

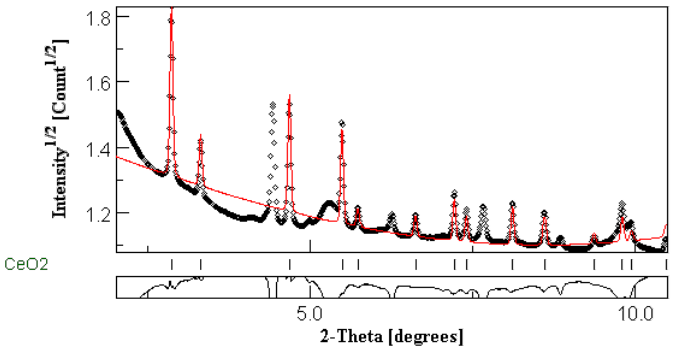

Figure B.2: Diffractogram of the calibrant CeO_2 for the specimen Q265P400.

The R_{wp} values for the fitting of each XRD diffractogram obtained for different specimens are shown in Figure B.3. The high R_{wp} values of the first few files are due to the spotty rings observed in the corresponding 2D XRD profiles.

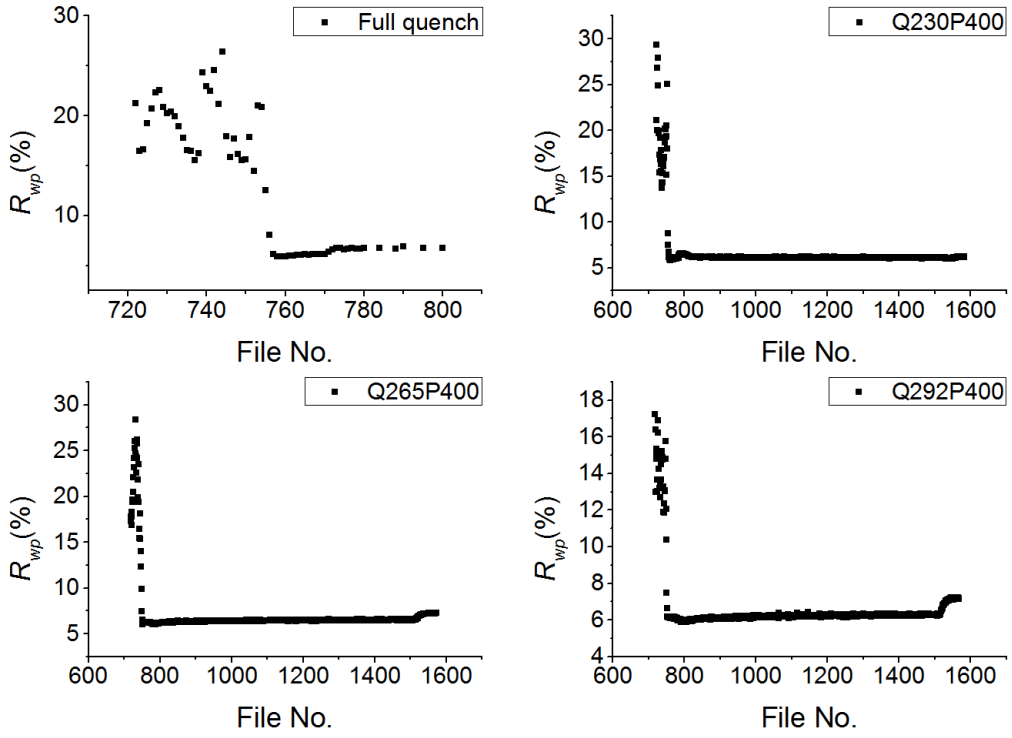

Figure B.3: XRD diffractograms of the first set of dilatometry specimens

B.3. XRD Experiments for the Second Dilatometry Tests

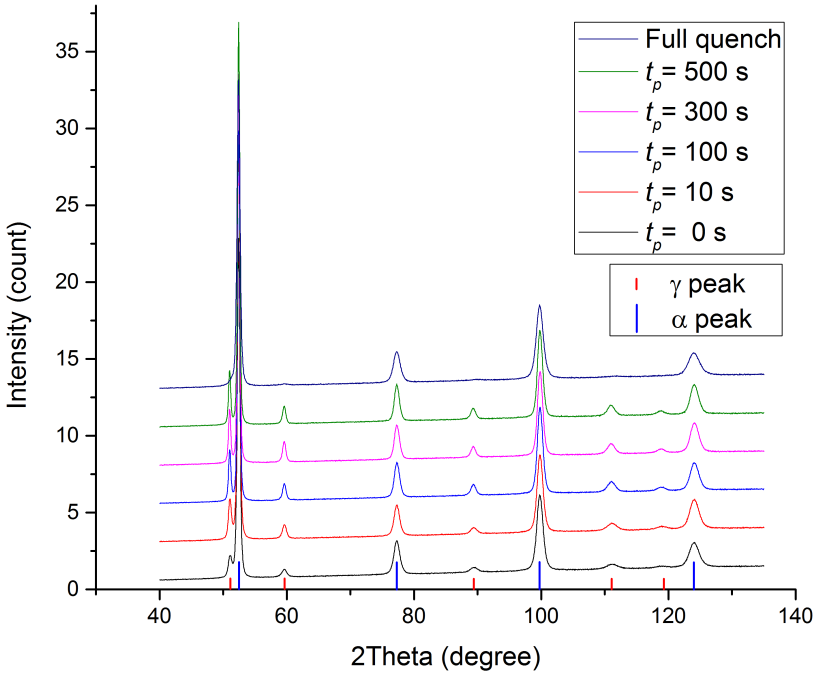

Figure B.4: XRD diffractograms of the second set of dilatometry specimens.

Figure B.4 presents the diffractograms measured for the specimens in the second dilatometry tests. The approximate peak positions are indicated by the blue lines (α peaks) or red lines (γ peaks).

C

Transformation Temperatures and Fittings

C.1. Identification of Transformation Temperatures

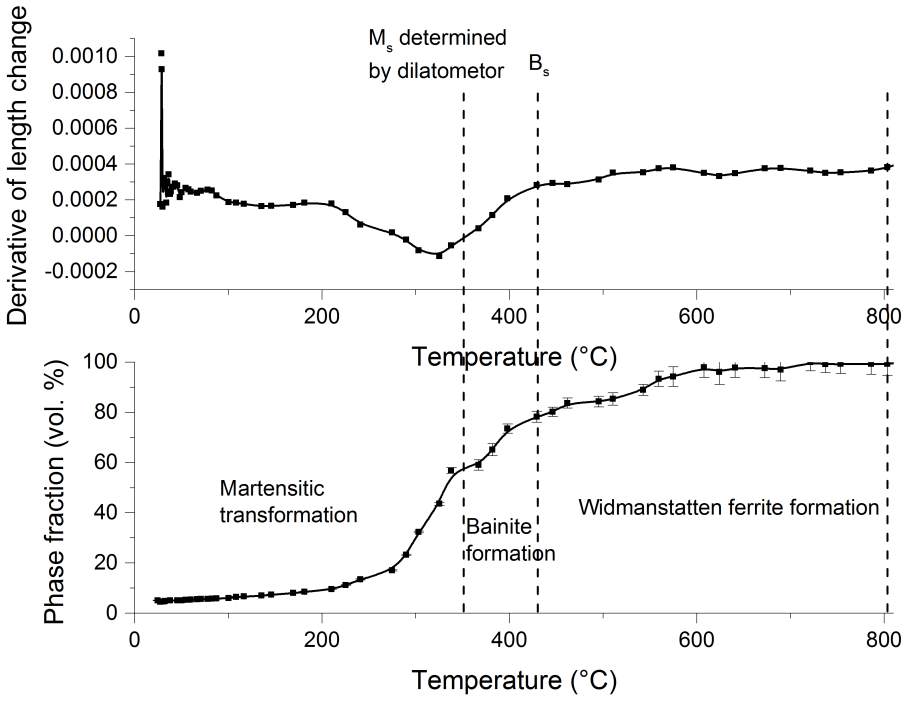

Figure C.1: Evolution of austenite fraction during initial quenching for Full quench.

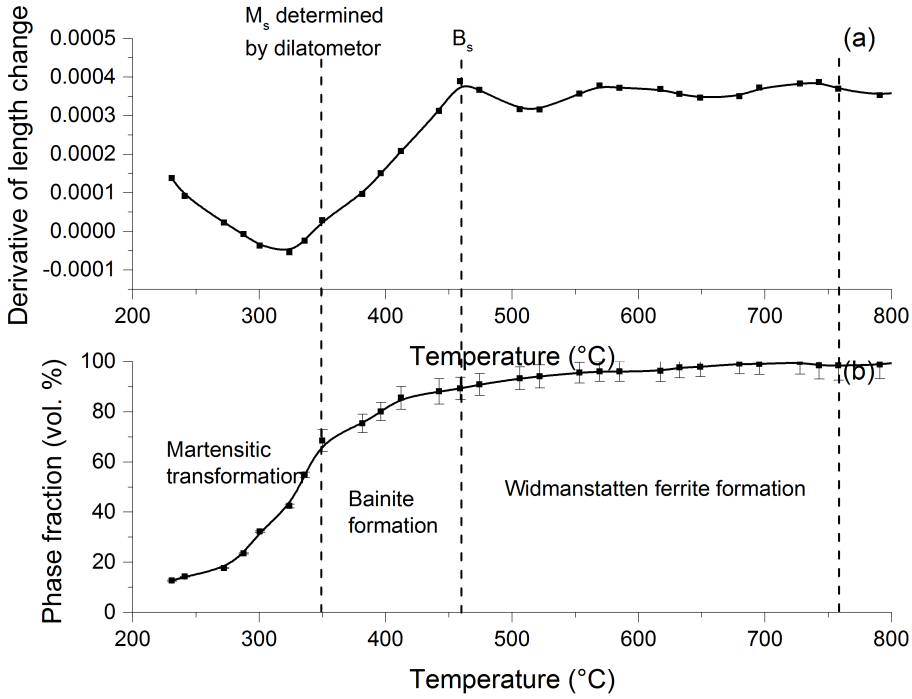

Figure C.2: Evolution of austenite fraction during initial quenching for Q230P400.

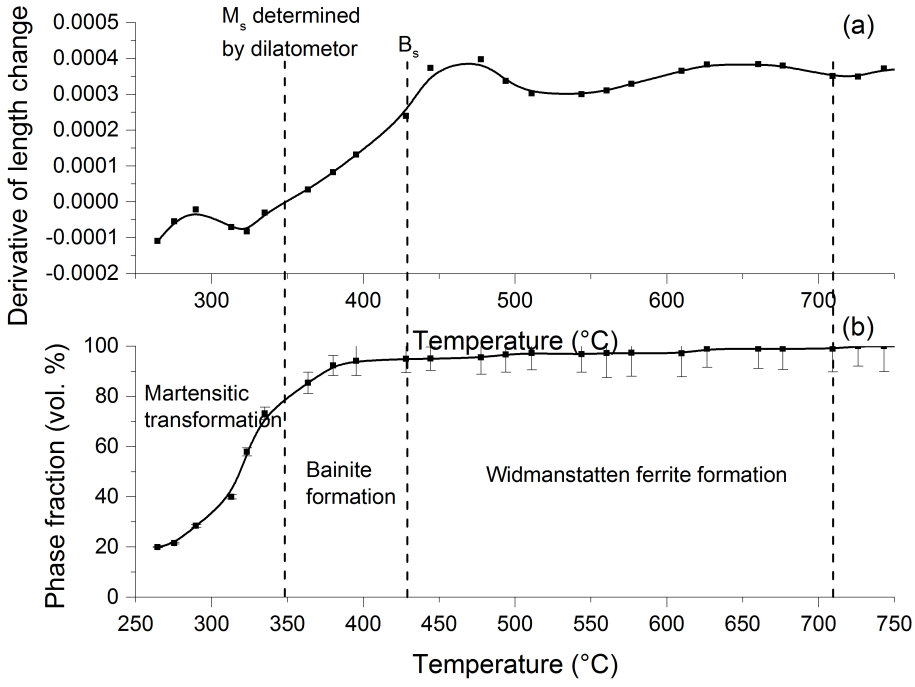

Figure C.3: Evolution of austenite fraction during initial quenching for Q265P400.

C.2. Linear Fitting of a_γ during Initial Quenching

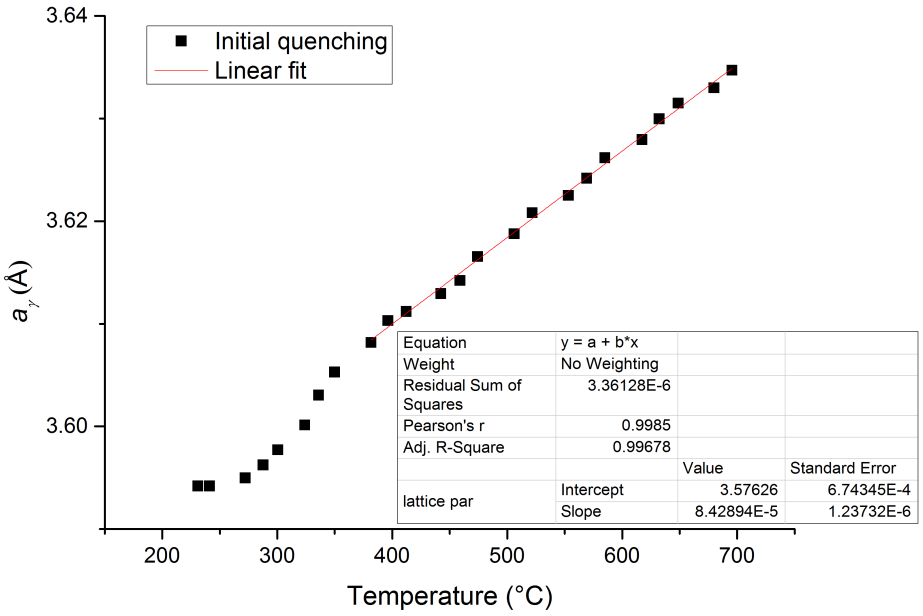

Figure C.4: Linear fitting of a_γ during initial quenching for Q230P400.

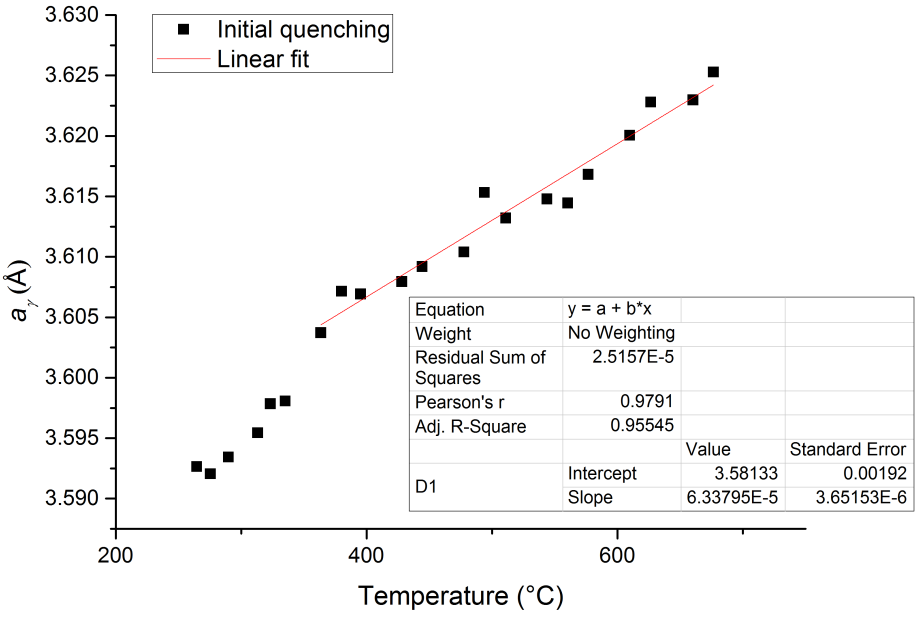

Figure C.5: Linear fitting of a_γ during initial quenching for Q265P400.

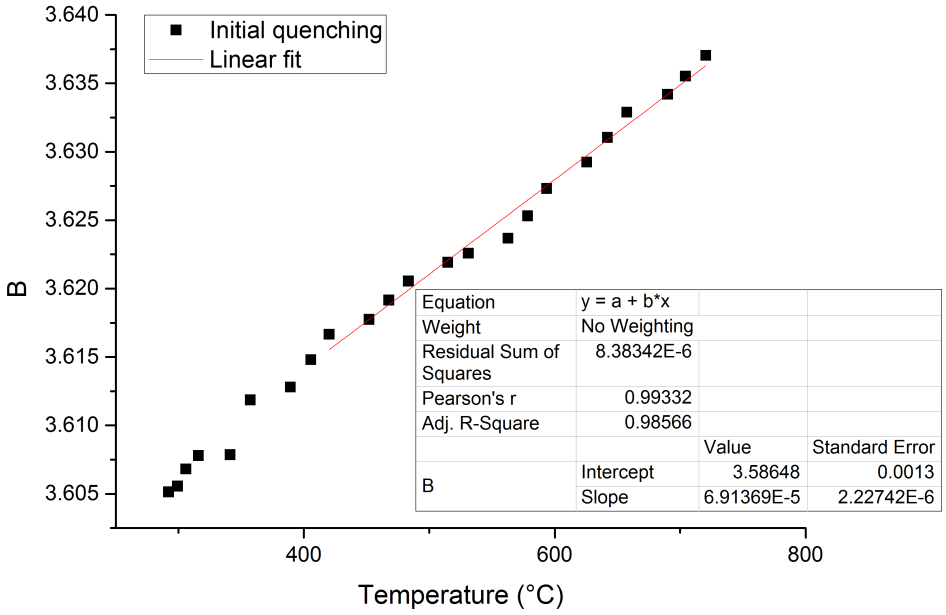

Figure C.6: Linear fitting of a_γ during initial quenching for Q292P400.

C.3. Linear Fitting of a_α during reheating

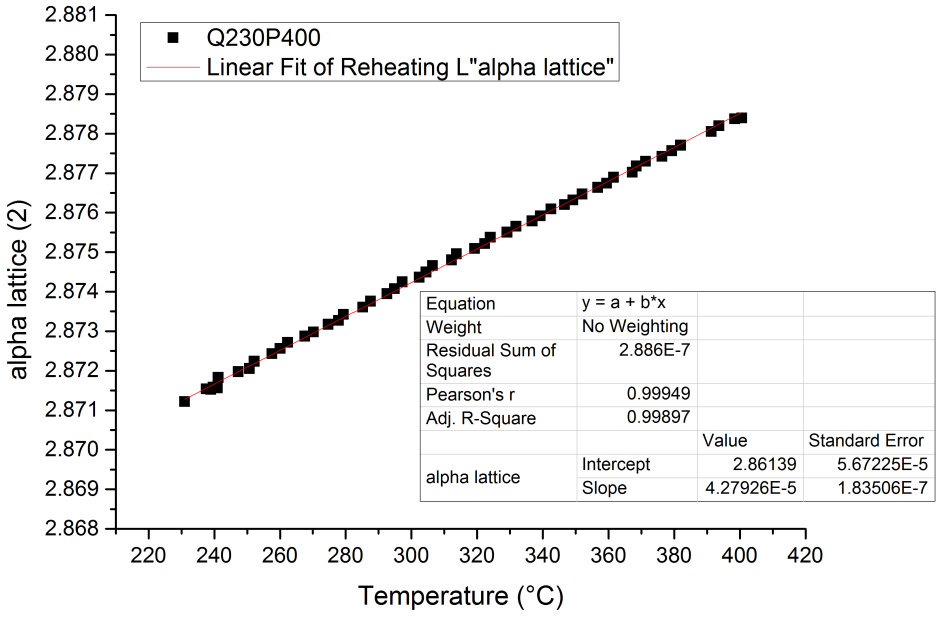

Figure C.7: Linear fitting of a_α for Q230P400.

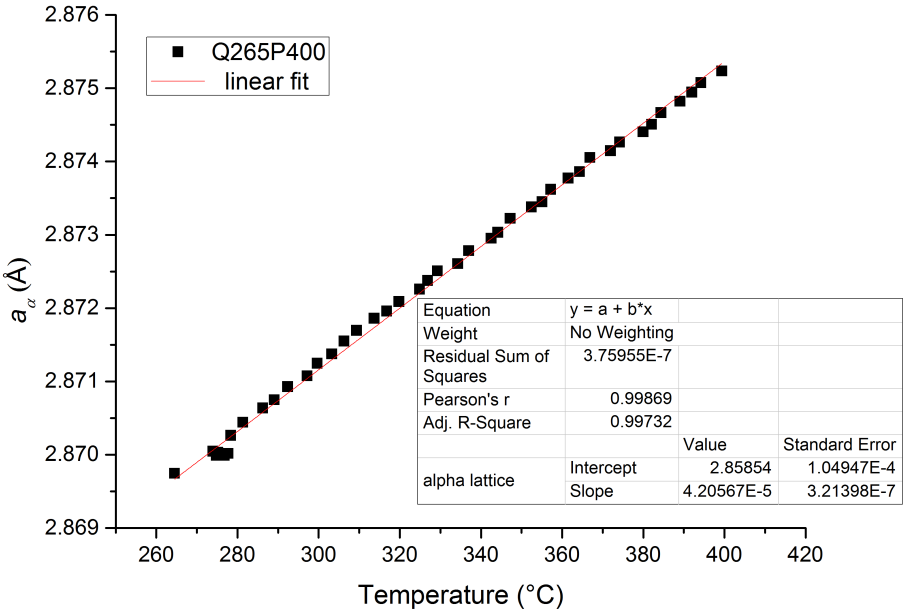

Figure C.8: Linear fitting of a_α for Q265P400.

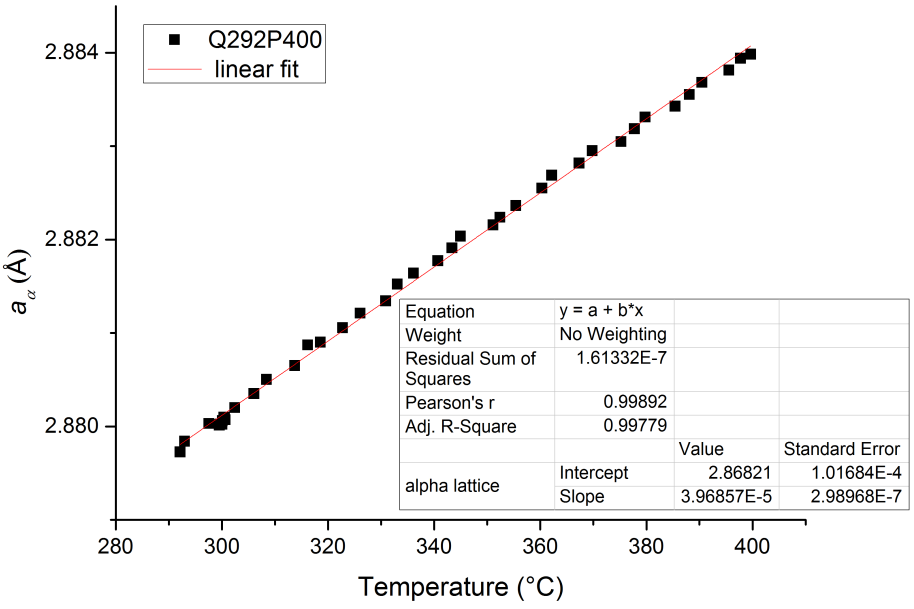

Figure C.9: Linear fitting of a_α for Q292P400.

C.4. Linear Fitting of a_α and a_γ during Final Quenching

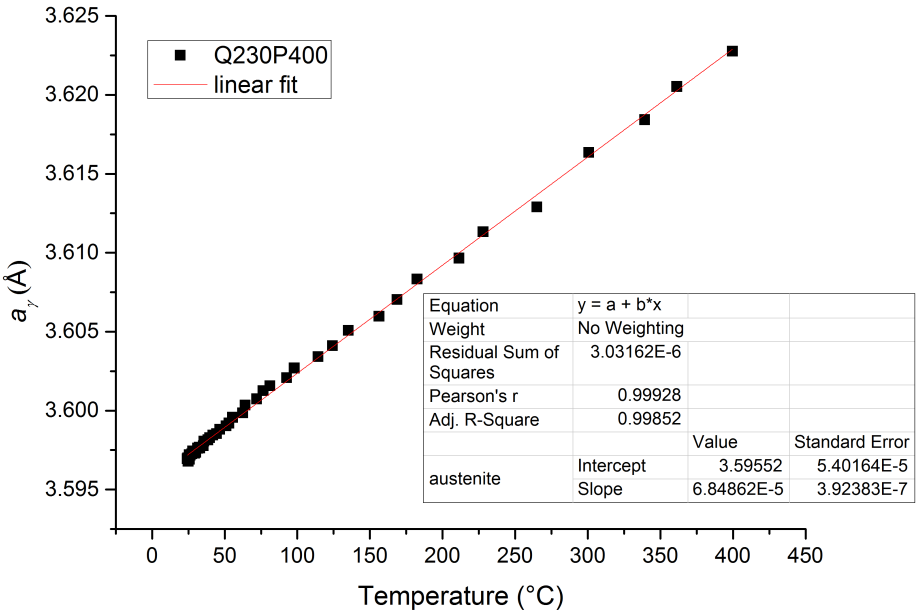

Equation	y = a + b*x		
Weight	No Weighting		
Residual Sum of Squares	3.03162E-6		
Pearson's r	0.99928		
Adj. R-Square	0.99852		
		Value	Standard Error
austenite	Intercept	3.59552	5.40164E-5
	Slope	6.84862E-5	3.92383E-7

Figure C.10: Linear fitting of a_γ for Q230P400.

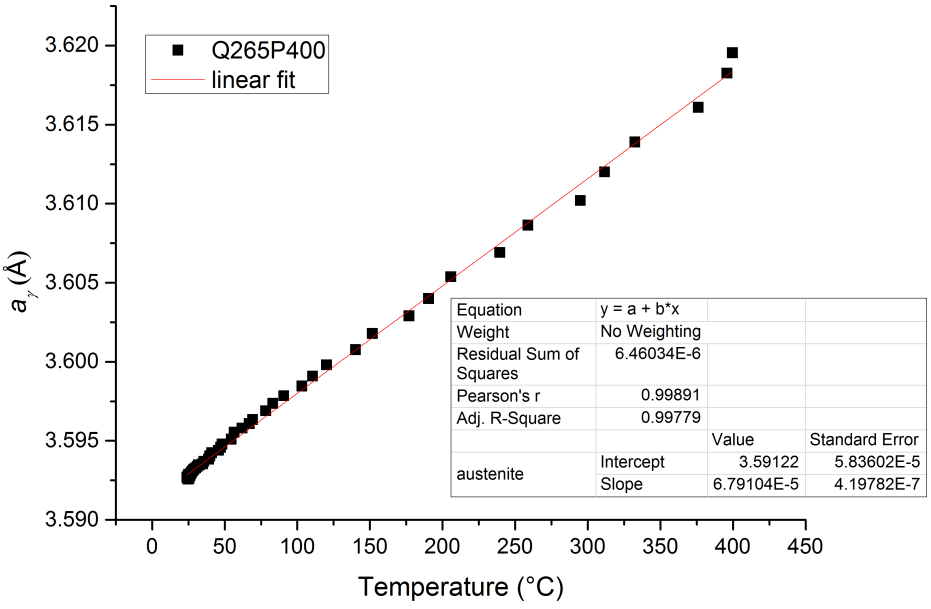

Equation	y = a + b*x		
Weight	No Weighting		
Residual Sum of Squares	6.46034E-6		
Pearson's r	0.99891		
Adj. R-Square	0.99779		
		Value	Standard Error
austenite	Intercept	3.59122	5.83602E-5
	Slope	6.79104E-5	4.19782E-7

Figure C.11: Linear fitting of a_γ for Q265P400.

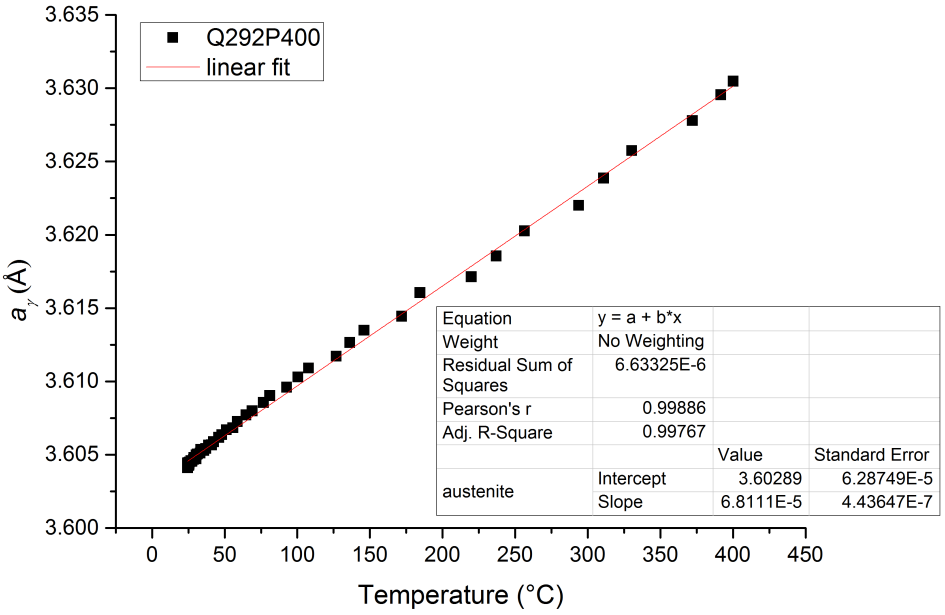

Figure C.12: Linear fitting of a_γ for Q292P400.

C.5. Summary of Fitting

Table C.1: Linear fitting of $a_\alpha - T$ during reheating

Specimen	Fitted slope	Fitted intercept	Fitted equation	R^2
Q230P400	$(4.28 \pm 0.02) \times 10^{-5}$	2.8614 ± 0.0001	$a_\alpha = 4.28 \times 10^{-5} T + 2.8614$	0.999
Q265P400	$(4.21 \pm 0.03) \times 10^{-5}$	2.8585 ± 0.0001	$a_\alpha = 4.21 \times 10^{-5} T + 2.8585$	0.997
Q292P400	$(3.97 \pm 0.03) \times 10^{-5}$	2.8682 ± 0.0001	$a_\alpha = 3.97 \times 10^{-5} T + 2.8682$	0.998

Table C.2: Linear fitting of $a_\gamma - T$ during initial quenching

Specimen	Fitted slope	Fitted intercept	Fitted equation	R^2
Q230P400	$(8.43 \pm 0.12) \times 10^{-5}$	3.5763 ± 0.0007	$a_\gamma = 8.43 \times 10^{-5} T + 3.5763$	0.997
Q265P400	$(6.34 \pm 0.37) \times 10^{-5}$	3.5813 ± 0.0019	$a_\gamma = 6.34 \times 10^{-5} T + 3.5813$	0.955
Q292P400	$(6.91 \pm 0.22) \times 10^{-5}$	3.5865 ± 0.0013	$a_\gamma = 6.91 \times 10^{-5} T + 3.5865$	0.986

Table C.3: Carbon content at the beginning and the end of the reheating for the three specimens.

Specimen	C_γ^{begin}	C_γ^{end}
Q230P400	0.43 ± 0.02	0.67 ± 0.02
Q265P400	0.49 ± 0.04	$0.66^{+0.04}$
Q292P400	0.65 ± 0.03	0.82 ± 0.03

Table C.4: Linear fitting of $a_\gamma - T$ during final quenching

Specimen	Fitted slope	Fitted intercept	Fitted equation	R^2
Q230P400	$(6.85 \pm 0.04) \times 10^{-5}$	3.5955 ± 0.0001	$a_\gamma = 6.85 \times 10^{-5} T + 3.5955$	0.998
Q265P400	$(6.79 \pm 0.04) \times 10^{-5}$	3.5912 ± 0.0001	$a_\gamma = 6.79 \times 10^{-5} T + 3.5912$	0.998
Q292P400	$(6.81 \pm 0.04) \times 10^{-5}$	3.6029 ± 0.0001	$a_\gamma = 6.81 \times 10^{-5} T + 3.6029$	0.998